

DETECTION OF F-REGION ELECTRON DENSITY IRREGULARITIES USING  
INCOHERENT-SCATTER RADAR

By

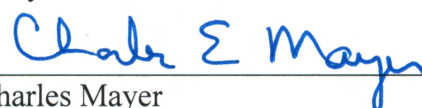
Krishna Prasad Gudivada

RECOMMENDED:

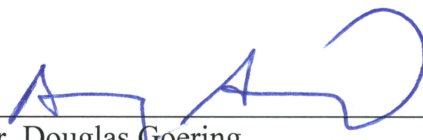
  
\_\_\_\_\_  
Dr. Vikas Sonwalkar

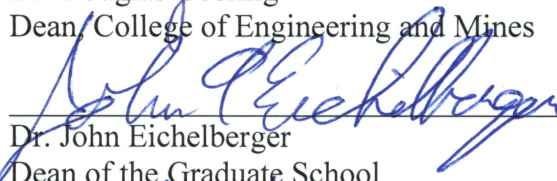
  
\_\_\_\_\_  
Dr. William Bristow

  
\_\_\_\_\_  
Dr. Brenton Watkins  
Advisory Committee Chair

  
\_\_\_\_\_  
Dr. Charles Mayer  
Chair, Department of Electrical and Computer Engineering

APPROVED:

  
\_\_\_\_\_  
Dr. Douglas Goering  
Dean, College of Engineering and Mines

  
\_\_\_\_\_  
Dr. John Eichelberger  
Dean of the Graduate School

  
\_\_\_\_\_  
Date



DETECTION OF F-REGION ELECTRON DENSITY IRREGULARITIES USING  
INCOHERENT-SCATTER RADAR

A  
THESIS

Presented to the Faculty  
of the University of Alaska Fairbanks

in Partial Fulfillment of the Requirements  
for the Degree of

MASTER OF SCIENCE

By

Krishna Prasad Gudivada, B.Tech.

Fairbanks, Alaska

August 2014

## Abstract

Incoherent-scatter radar data from Poker Flat, Alaska has been used to determine size distributions of electron density structures in the evening time sector of the auroral zone. At high latitudes ionospheric plasma typically moves east-west with speeds of several hundred meters per second. Density irregularities that rapidly move through the radar beam are therefore observed as time-varying power fluctuations. The new phased array radar used for this study has been operated with several antenna directions with successive pulses transmitted in each direction. It is therefore possible to observe plasma Doppler velocities in multiple directions and determine the vector direction of the plasma motion.

This near-simultaneous observation of the plasma velocity in conjunction with the electron density height profile data enable a new technique to determine the scale sizes of electron density fluctuations that move horizontally through the radar beam. The study focuses on the collision-less F-region ionosphere where the plasma drift is approximately constant with altitude. The experimental technique limits the range of scale sizes that may be studied to relatively large-scale sizes (i.e. greater than few tens of km).

Results show that during magnetically disturbed conditions ( $K_p \geq 4$ ) when westward plasma velocities are relatively high (500-1000 m/s) the scale sizes of irregularities (often called plasma blobs) are in the range of 100-300 km and predominantly originate from the polar cap and are transported over long distances (~1000 km) due to the long chemical recombination times (30-90 minutes). Some irregularities are caused by local auroral particle precipitation and have been identified with associated electron temperature enhancements. For cases of low magnetic activity ( $K_p \leq 1$ ), when the radar is located in a region of low plasma velocities (100-500 m/s) well south of the auroral oval (essentially a mid-latitude type ionosphere), the density distribution is always biased strongly toward small-scale sizes (less than 50 km).



## Table of Contents

	Page
Signature Page.....	i
Title Page.....	iii
Abstract.....	v
Table of Contents.....	vii
List of Figures.....	ix
List of Tables.....	xiii
Acknowledgements.....	xiv
Dedication.....	xv
<b>CHAPTER 1. INTRODUCTION.....</b>	<b>1</b>
1.1. Overview of the Ionosphere.....	1
1.2. Impact of Electron Density Irregularities on Navigation Systems and SAR Imaging ..	4
1.3. Historical Review and Objective of Thesis .....	7
<b>CHAPTER 2. INCOHERENT SCATTER RADAR .....</b>	<b>15</b>
2.1. Introduction.....	15
2.2. Determination of Electron Density .....	27
2.3. Basic Experiment Design and Estimation of Line-of-sight Velocity .....	30
2.4. Determination of Ion Vector Velocities.....	34
<b>CHAPTER 3. EXPERIMENTAL APPROACH.....</b>	<b>43</b>
3.1. Introduction.....	43
3.2. AMISR System Description .....	43
3.3. Description of Experiments .....	44
3.4. Determination of Ionization Blob Scale Sizes.....	53
<b>CHAPTER 4. OBSERVATIONS OF ELECTRON DENSITY IRREGULARITIES USING     THE POKER FLAT INCOHERENT SCATTER RADAR .....</b>	<b>63</b>
4.1. Introduction.....	63
4.2. Results.....	64

4.2.1. August 28th, 2011 .....	64
4.2.2. August 31 <sup>st</sup> , 2011 .....	68
4.2.3. March 9 <sup>th</sup> , 2012 .....	70
4.2.4. March 25 <sup>th</sup> , 2012 .....	73
4.2.5. October 9 <sup>th</sup> , 2012.....	76
4.2.6. October 12 <sup>th</sup> , 2012.....	79
4.2.7. October 19 <sup>th</sup> , 2012.....	82
4.2.8. November 4 <sup>th</sup> , 2012.....	84
4.3. Discussion .....	89
<b>CHAPTER 5. CONCLUSIONS AND FUTURE WORK .....</b>	<b>93</b>
5.1. Conclusions.....	93
5.2. Future Work.....	94

## List of Figures

	Page
<b>Figure 1.1:</b> (a) Structure of ionosphere during day time as a function of altitude and electron density. (b) Structure of ionosphere during night time as a function of altitude and electron density. ....	3
<b>Figure 1.2:</b> (a) Propagation of high-frequency radio waves by reflection of ionosphere during day time. (b) Propagation of high-frequency radio waves by reflection of ionosphere during night time. ....	4
<b>Figure 1.3:</b> Ionospheric effects on radio wave propagation.....	7
<b>Figure 1.4:</b> Synthetic Aperture Radar Imaging concept with the presence of F region electron density blobs. ....	8
<b>Figure 1.5:</b> Plasma Convection at high-latitude (a) Basic two-cell convection pattern under southward IMF conditions. (b) An example of four-cell convection pattern under northward IMF conditions. ....	11
<b>Figure 1.6:</b> Irregular structures in the polar cap ionosphere (a) Patches drifting anti-sunward during Southward IMF state (b) Sun-aligned arcs or theta auroras with Dawn-Dusk drift observed during Northward IMF state. [After Carlson 1994] .....	12
<b>Figure 1.7:</b> Altitude/latitude variation of electron density in the midnight sector auroral zone measured by the Chatanika incoherent scatter radar [From Kelley et al., 1982].....	13
<b>Figure 2.1:</b> Typical power spectrum of the signal received as a function of frequency showing both upshifted and downshifted ion-lines and plasma-lines.....	21
<b>Figure 2.2:</b> Dependence of the shape of the ISR ion-line spectrum and autocorrelation function on ion temperatures $T_i$ . [Courtesy of C.J. Heinselman] .....	22
<b>Figure 2.3:</b> Dependence of the shape of the ISR ion-line spectrum and autocorrelation function on ion mass $m_i$ . [Courtesy of C.J. Heinselman].....	23
<b>Figure 2.4:</b> Dependence of the shape of the ISR ion-line spectrum and autocorrelation function on electron to ion temperature ratio $T_r$ . [Courtesy of C.J. Heinselman].....	24
<b>Figure 2.5:</b> Dependence of the shape of the ISR ion-line spectrum and autocorrelation function on Doppler shift. [Courtesy of C.J. Heinselman].....	25
<b>Figure 2.6:</b> Dependence of the shape of the ISR ion-line spectrum and autocorrelation function on ion-neutral collision frequency. [Courtesy of C.J. Heinselman] .....	26



<b>Figure 2.7:</b> Overall picture of the power spectrum dependence on various plasma parameters.	27
<b>Figure 2.8:</b> The left panel shows received power as a function of altitude using an integration of 5000 samples and the right panel shows the electron density (without temperature corrections) plot as a function of altitude calculated after range corrections. ....	30
<b>Figure 2.9:</b> Two dimensional ambiguity function of a long-pulse with a pulse width of 480 $\mu$ s sampled at rate of 30 $\mu$ s including filter effects.....	32
<b>Figure 2.10:</b> Measured autocorrelation function and power spectrum as a function of altitude along with fitted data for the beam direction along the field line using long-pulse data [Courtesy of M.J. Nicolls].....	33
<b>Figure 2.11:</b> Experimental configuration for THEMIS 13 beam position mode. The top panel shows the azimuth and elevation for all the beam directions and the bottom panel shows the geomagnetic latitude and longitude coverage of the beams. ....	39
<b>Figure 2.12:</b> Line-of-sight ion velocities as a function of time and altitude for 13 beam positions from the long-pulse measurements on 02 December 2012.....	40
<b>Figure 2.13:</b> Electron density (with temperature corrections) as a function of time and altitude for 13 beam positions from the long-pulse measurements on 02 December 2012..	41
<b>Figure 2.14:</b> Perpendicular east, perpendicular north and anti-parallel velocities along with error estimates as function of magnetic latitude and time from the long-pulse measurements on 02 December 2012. ....	42
<b>Figure 3.1:</b> Building blocks of an AMISR system.....	44
<b>Figure 3.2:</b> Northward looking UHF phased array radar at Poker Flat, near Fairbanks, Alaska.	45
<b>Figure 3.3:</b> (a) Possible PFISR beam directions with black star shaped grating lobe limits of the system. (b) Contours represent the PFISR's field of view at 100, 200, 300 and 400 km altitude. ....	46
<b>Figure 3.4:</b> Geometry plot of the azimuthal and elevation angle of the beams. ....	48
<b>Figure 3.5:</b> Electron density plot (Integration time of 2 seconds) from an altitude of 200-450 km with no Te/Ti correction as a function of altitude and time from the vertical beam [AZ: 14.04°, El: 90°] of PFISR. ....	49
<b>Figure 3.6:</b> Filtered Electron density plot (integration time of 2 seconds) from an altitude of 200-450 km with no Te/Ti correction as a function of altitude and time from the vertical beam [Az: 14.04°, El: 90°] of PFISR. ....	53

<b>Figure 3.7:</b> Height Integrated Electron density Ne (Integrated over F region i.e., from 200-250 km) with no Te/Ti correction as a function of time from the vertical beam [Az: 140.040, El: 90o] of PFISR.....	54
<b>Figure 3.8:</b> Single sided amplitude spectrum of integrated and detrended electron density data for about 12 minutes estimated using Blackman-Tukey spectral estimate (using Kaiser Window) a function of frequency.....	56
<b>Figure 3.9:</b> (a) Eastward ion velocities and (b) Northward ion velocities from 9-12 UT on 30 August 2011 as a function of time and magnetic latitude.....	57
<b>Figure 3.10:</b> Bar graph of blob occurrence as a function of scale sizes on 30 August 2011.....	59
<b>Figure 3.11:</b> Auroral activity during quiet conditions ( $K_p \leq 1$ ) over Alaska. ....	60
<b>Figure 3.12:</b> Auroral activity during moderate conditions ( $2 \leq K_p \leq 3$ ) over Alaska. ....	60
<b>Figure 3.13:</b> Auroral activity during disturbed conditions ( $K_p \geq 3$ ) over Alaska.....	61
<b>Figure 3.14:</b> Distribution of ionization blob scale sizes for different density threshold values during slightly active conditions ( $K_p = 2$ ).....	61
<b>Figure 3.15:</b> Distribution of ionization blob scale sizes for different density threshold values during disturbed conditions ( $K_p = 5$ ). ....	62
<b>Figure 4.1:</b> Magnetometer data from Poker Flat and Ft Yukon on 28 August 2011. [Onset of westward current is noted from onset of the negative excursion of the magnetic H component and Z component indicates the location of the substorm current]. ....	65
<b>Figure 4.2:</b> Magnetometer data and PFISR results for the night of 28 August 2011 from 09-12 UT. ....	66
<b>Figure 4.3:</b> Bar graph of blob occurrence as a function of scale sizes on 28 August 2011.....	68
<b>Figure 4.4:</b> Magnetometer data and PFISR results for the night of 31 August 2011 from 09-12 UT. ....	69
<b>Figure 4.5:</b> graph of blob occurrence as a function of scale sizes on 31 August 2011.....	70
<b>Figure 4.6:</b> Magnetometer data from Poker Flat and Ft Yukon on 09 March 2012. ....	71
<b>Figure 4.7:</b> Magnetometer data and PFISR results for the night of 09 March 2012 from 09-13 UT .....	72
<b>Figure 4.8:</b> Bar graph of blob occurrence as a function of scale sizes on 09 March 2012.....	73
<b>Figure 4.9:</b> Magnetometer data from Poker Flat and Ft Yukon on 25 March 2012. ....	74

<b>Figure 4.10:</b> Magnetometer data and PFISR results for the night of 25 March 2012 from 09-13 UT. ....	75
<b>Figure 4.11:</b> Bar graph of blob occurrence as a function of scale sizes on 25 March 2012. ....	76
<b>Figure 4.12:</b> Magnetometer data from Poker Flat and Ft Yukon on 09 October 2012. ....	77
<b>Figure 4.13:</b> Magnetometer data and PFISR results for the night of 09 October 2012 from 07-10 UT. ....	78
<b>Figure 4.14:</b> graph of blob occurrence as a function of scale sizes on 09 October 2012. ....	79
<b>Figure 4.15:</b> Magnetometer data from Poker Flat and Ft Yukon on 12 October 2012. ....	80
<b>Figure 4.16:</b> Magnetometer data and PFISR results for the night of 12 October 2012 from 07-10 UT. ....	81
<b>Figure 4.17:</b> Bar graph of blob occurrence as a function of scale sizes on 12 October 2012. ....	82
<b>Figure 4.18:</b> Magnetometer data and PFISR results for the night of 19 October 2012 from 07-10 UT. ....	83
<b>Figure 4.19:</b> Bar graph of blob occurrence as a function of scale sizes on 19 October 2012. ....	84
<b>Figure 4.20:</b> Magnetometer and PFISR data for the night of 04 November 2012 from 07-10 UT. ....	85
<b>Figure 4.21:</b> Bar graph of blob occurrence as a function of scale sizes on 04 November 2012. ....	86
<b>Figure 4.22:</b> Bar graph of blob occurrence as a function of scale sizes on (a) 27 August 2011 (b) 29 August 2011 (c) 30 August 2011 (d) 26 March 2012 (e) 15 January 2013. ....	88
<b>Figure 4.23:</b> Irregular structures in the polar cap ionosphere (a) Patches drifting anti-sunward during Southward IMF state (b) Sun-aligned arcs or theta auroras with Dawn-Dusk drift observed during Northward IMF state [After Carlson 1994]. ....	90
<b>Figure 4.24:</b> Consistent trend of plasma flow observed from numerous case studies using Poker Flat incoherent scatter radar. ....	91
<b>Figure 5.1:</b> (a) Geometry plot of the azimuthal and elevation angles of the beams. (b) Range coverage of the beams as a function of magnetic longitude and magnetic latitude. ....	95
<b>Figure 5.2:</b> Northward looking UHF phased array radar at Resolute Bay, on Cornwallis Island, Canada. ....	96

## List of Tables

	Page
<b>Table 4.1:</b> Operations carried out using Poker Flat Incoherent-scatter radar from Aug, 2011-Jan, 2013... .....	63

## **Acknowledgements**

It would not have been possible to write this thesis without the help and support of the kind people around me, to only some of whom it is possible to give particular mention here.

First and foremost I offer my sincerest gratitude to my principal advisor, Dr. Brenton Watkins, who has supported me throughout my thesis with his patience and knowledge while allowing me the room to work in my own way. I attribute the level of my Master's degree to his encouragement and effort and without him this thesis, too, would not have been completed or written. One simply could not wish for a better or friendlier advisor. Besides my advisor, I would like to thank the rest of my thesis committee: Dr. Vikas Sonwalkar and Dr. William Bristow, for their encouragement and insightful comments.

I would like to thank Dr. Joseph Hawkins, Dr. Jason McNeely, and Dr. Seta Bogosyan whose advice and encouragement were invaluable to me. I would also like to thank my colleague Dr. Chris Fallen for his stimulating discussions on space physics and for all the fun we had in the last three years.

The financial support from the Department of Electrical and Computer Engineering, NSF grants #1243476 and #0608577, are gratefully acknowledged.

Craig Heinselman and Michael Nicolls deserve special thanks for their work in providing me the data with a special mode for the whole thesis.

Last, but by no means least, I would like to thank my family and relatives especially my mother and my uncles for believing in me, for their continuous love and their support in my decisions. Without them I could not have made it here.

For any errors or inadequacies that may remain in this work, of course, the responsibility is entirely my own.

I would like to dedicate my thesis  
to my beloved grandparents



## CHAPTER 1. INTRODUCTION

In the auroral zone naturally occurring plasma irregularities with a broad range of horizontal spatial scale sizes exist in the ionosphere, particularly at evening due to the effects of particle precipitation, magnetospheric convection electric fields and auroral currents. Of particular interest in the present study are the large-scale electron density enhancements in auroral zone F-region ionosphere known as blobs. Ionospheric blobs are associated with small-scale density irregularities that may affect satellite to ground communication links such as GPS navigation systems. These structures also are potentially significant to applications such as SAR (Synthetic Aperture Radar) satellite imaging of earth. The newly available PFISR (Poker Flat Incoherent Scatter Radar) is a powerful ground-based remote sensing tool capable of studying earth atmosphere and ionosphere that we have used to investigate these large-scale density structures. Phased-array (pulse-to-pulse steering) technology integrated with this UHF (ultra high frequency) radar allows near-simultaneous measurements of numerous plasma parameters, such as electron density, ion drift velocity, electron/ion temperatures and line-of-sight (los) velocity in multiple look directions. The objective of this thesis is to use high-time resolution measurements from the radar at Poker Flat, Alaska to estimate the scale sizes of irregularity structures.

This thesis is divided into five chapters. Chapter 1 introduces the background and motivation of the thesis, including the overview of the ionosphere, the effects of electron density irregularity structures on navigation systems and SAR imaging, the review of previous studies and the objective of the thesis. Chapter 2 discusses the incoherent-scatter radar technique, advantages of the phased-array radar over traditional incoherent scatter radar, and determination of electron density and estimation of ion velocity. Chapter 3 discusses the experimental approach, signal processing techniques and assumptions used to calculate the distribution of scale sizes of electron density blobs. The results and findings of electron density irregularity observations carried out on fourteen different nights using the incoherent-scatter radar at the Poker Flat Research Range are discussed in chapter 4. Finally the conclusion and future work are discussed in chapter 5.

### 1.1. Overview of the Ionosphere

The study of the ionized region of the earth's atmosphere, i.e. the ionosphere, has gained its importance with the evolution of long-distance radio communication. In 1902, Arthur Kennelly and Oliver Heaviside independently suggested that ionized layers of the upper



atmosphere are responsible for the refraction/reflection of radio waves over the curvature of the earth from trans-Atlantic communication experiments demonstrated by Guglielmo Marconi in 1901 [Hunsucker and Hargreaves, 2003]. Later, a set of experiments conducted by Appleton provided direct evidence of ionized layers above 50 km from the earth's surface [Appleton and Barnett, 1925a, 1925b]. Breit and Tuve [1926] confirmed the existence of conducting layers through their oscillographic study of radio echoes from the ionized layers. Both studies were based on findings of radio signals of frequency  $f$  reflected from ionized layers present at an altitude at which the signal frequency is equal to plasma frequency (i.e.,  $f = f_{pe}$  where  $f_{pe}$  is the plasma frequency). High frequency signals with a frequency  $f$  greater than the plasma frequency (i.e.,  $f > f_{pe}$ ) propagate through the ionosphere into the space without any reflection. The plasma frequency and electron density are related as shown in equation 1.1,

$$f_{pe} = 8970 * \sqrt{Ne} \quad (1.1)$$

where  $f_{pe}$  = Plasma frequency in Hertz

$Ne$  = Electron density/cm<sup>3</sup>.

As shown in figure 1.1a, during day time the ionosphere is heavily ionized due to solar radiation and it has four regions (i.e. D, E, F1 and F2 regions). The D region of the ionosphere ranges from an altitude of ~ 60-95 km during the day. The electron recombination and attachment rates in this region are relatively high and the free electron density is very small ( $< 10^3 \text{ cm}^{-3}$ ). The region above the D region is the E region, also known as Kennelly-Heaviside layer. The E region of the ionosphere ranges from an altitude of ~ 90-140 km with an electron density ranging from  $10^4$ - $10^5 \text{ cm}^{-3}$ . Thin, enhanced layers of ionization known as sporadic-E are often observed at these altitudes. The F region has the maximum ionization which ranges from an altitude of 140-500 km above the earth's surface with an electron density maximum typically from  $10^5$ - $10^6 \text{ cm}^{-3}$  at about 250-300 km altitude. During the day time, the F region often has two distinct peaks, i.e. F1 (from 140-210 km) and F2 regions (over 200 km). During night time, with no EUV (Extreme Ultra Violet) radiation to produce electrons, the E and F regions rapidly decay as shown in figure 1.1b.

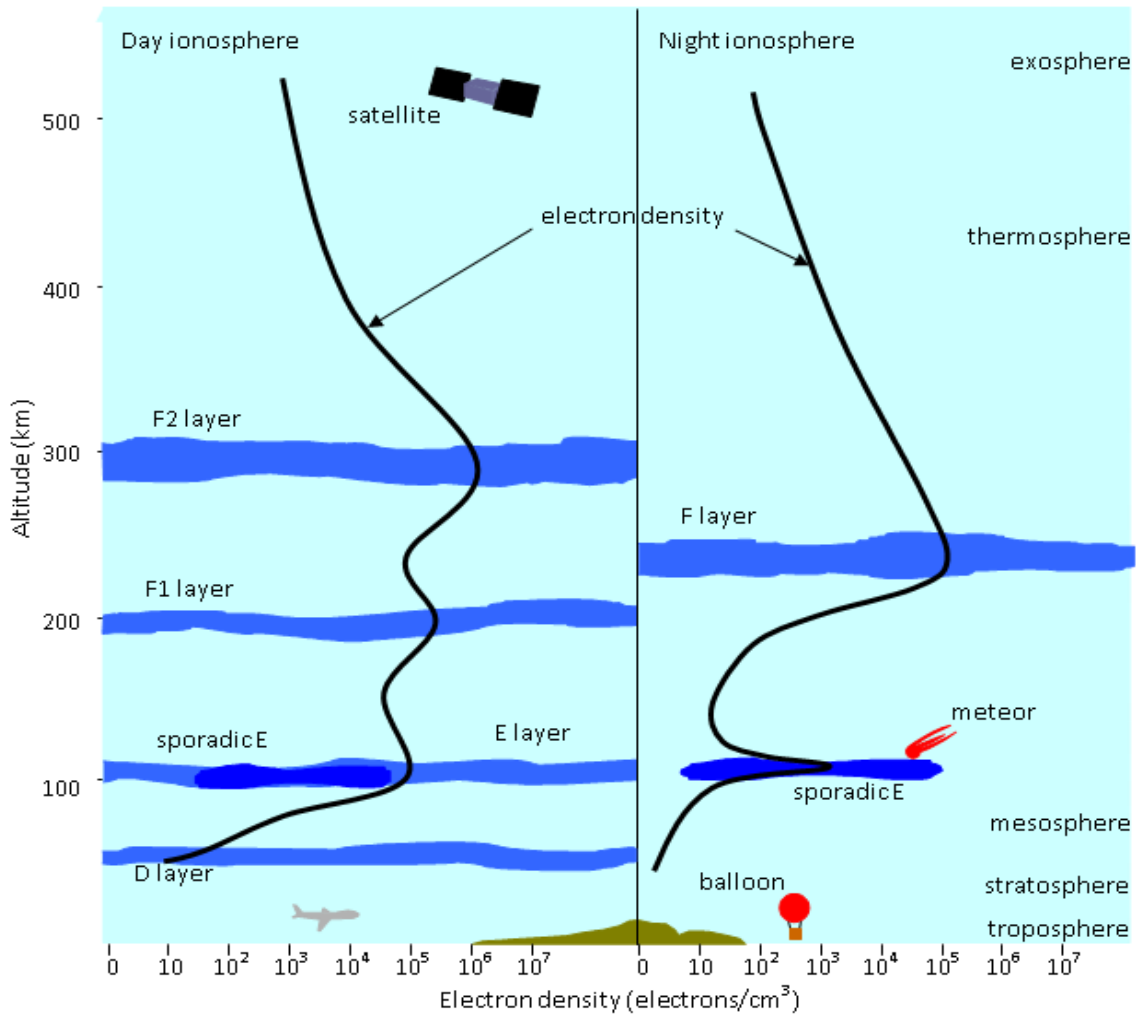


**Figure 1.1:** (a) Structure of ionosphere during day time as a function of altitude and electron density. (b) Structure of ionosphere during night time as a function of altitude and electron density.

Radio waves propagating through the ionosphere are sensitive to various phenomena such as absorption, reflection, refraction, scattering, polarization, dispersion and diffraction; these effects are dependent on wave frequency, altitude, etc. For example, due to the high collision frequency and recombination rate of electrons, the D region strongly absorbs the high frequency signals propagating through it. Under normal conditions sky wave propagation of High Frequency (3-30 MHz) radio waves over long distances is possible either by refraction or by multiple reflections between the ground and the E or F-region of the ionosphere as shown in Figure 1.2a. At night the intensity of the E region decreases, making it unsuitable for radio transmission and the radio communication is done via the F layer. The F layer is the most useful layer for long distance radio communications even though its degree of ionization varies from

time to time, day to day, season to season and geomagnetic latitude to latitude. Knowledge of unpredictable irregular variations of the F region is required in order to plan an efficient communication system.

The ionosphere can be probed by using a variety of tools such as ionosondes, radars, rockets, satellites, interferometers, and optical imagers. This thesis uses a ground-based radar technique for studying the earth's ionosphere (incoherent-scatter radar) which is discussed in-depth in chapter 2.

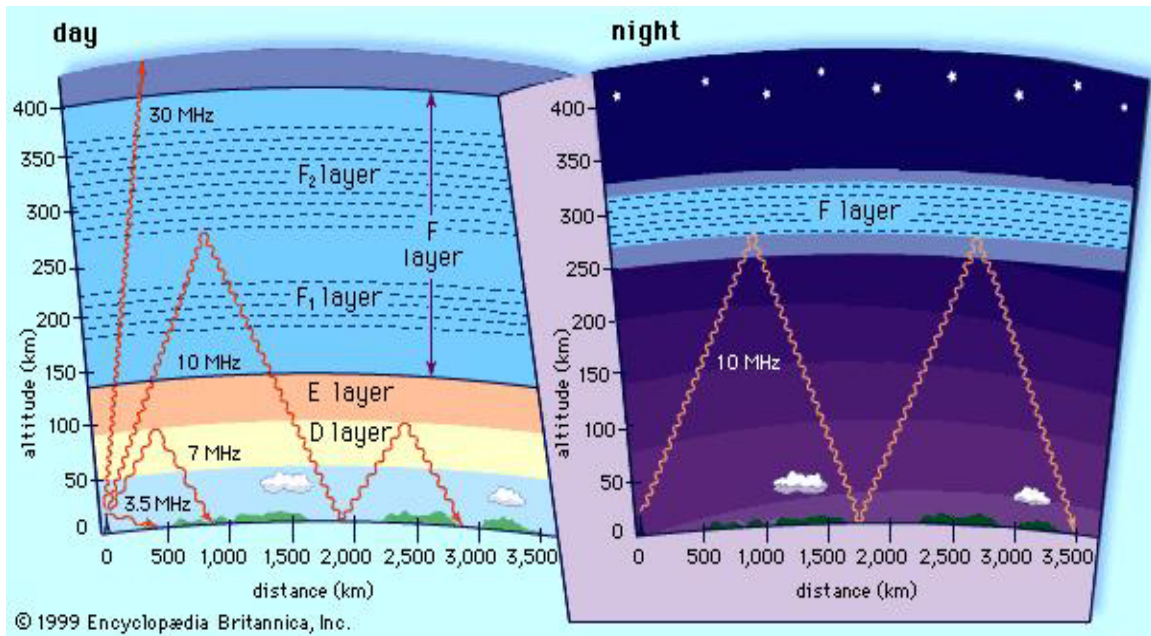


**Figure 1.2:** (a) Propagation of high-frequency radio waves by reflection of ionosphere during day time. (b) Propagation of high-frequency radio waves by reflection of ionosphere during night time.

## 1.2. Impact of Electron Density Irregularities on Navigation Systems and SAR Imaging

Communication and navigation systems located above the ionosphere transmit signals with frequencies higher than the maximum usable frequency of the ionosphere so that the signals can travel through the ionosphere and reach the receivers on the ground without getting reflected. Though these signals pass through the ionosphere without any reflection, there are considerable effects on their amplitude, phase and angle of arrival, known as ionospheric scintillation. The radio waves are diffracted as they propagate through regions of electron density irregularities and reach receivers on the ground through multiple paths, resulting in amplitude and phase fluctuations from constructive and destructive interference. Large-scale variations of electron density also vary the phase of the signal very rapidly. The phase and amplitude fluctuations of

the signal depend on the electron density along the path of the signal. The variation in the phase of the signal is given by

$$\text{Phase}(\phi) = \frac{8.448 \times 10^{-13} \times \text{TEC}}{f} \text{ rad} \quad (1.2)$$

where  $f$  = Radio frequency in MHz.

TEC = Total Electron Content (1 TEC unit =  $10^{16}$  electrons/m<sup>2</sup>) is the measure of total number of electrons along the path of the signal and is given by

$$\text{TEC} = \int_{r_1}^{r_2} N_e dr$$

where  $N_e$  = Electron density in electrons/m<sup>3</sup>

$r_1$  and  $r_2$  are the initial and final ranges of the path of the signal.

The phase of the modulation of the signal is varied by

$$\phi_m = -8.448 \times 10^{-7} \times \frac{f_m}{f_c^2} \times \text{TEC} \text{ rad} \quad (1.3)$$

where  $f_m$  = Modulated Frequency (Hz)

$f_c$  = Carrier Frequency (Hz).

Total electron content fluctuations also results in a time delay of the signal and is given by equation 1.4,

$$\Delta \text{time} = 8.448 \times 10^{-7} * \frac{\text{TEC}}{2 * \pi * f_c^2} \text{ sec.} \quad (1.4)$$

The wave propagating perpendicular to the slope of electron content fluctuations gets refracted through an angle  $\alpha$ , known as wedge refraction and is given by

$$\alpha = \left( \frac{c}{2 * \pi} \right) * \left( \frac{8.448 \times 10^{-19}}{f^2} \right) * \frac{\delta \text{TEC}}{\delta y} \quad (1.5)$$

where  $y$  = direction of the wave.

All the phase calculations are done by neglecting the geomagnetic field and collision frequencies. Under the influence of a magnetic field, when a linearly polarized wave is incident on a medium, the plane of polarization of the wave may rotate through an angle [Faraday, 1846]. Later, the theory of this Faraday Effect was extended to different media including the ionosphere [Verdet, 1856; Bacquerel, 1897; Cotton and Mouton, 1907; Pedersen, 1927; Browne et al., 1956; Davies, 1989; Yariv and Yel, 1984; Yeh et al., 1999]. The wave polarization angle changes as it propagates through the ionized medium and the amount of rotation depends on electron density along the path of the wave and the magnetic field strength. The angle of rotation, or the polarization angle ( $\Omega$ ), may be computed from

$$\Omega = \frac{2.365 \cdot 10^4}{f^2} \int_{r_1}^{r_2} Ne * B_L dr \quad (1.6)$$

where  $B_L$  = Magnetic field (webers/m<sup>2</sup>) component in the direction of wave propagation.

Electro-magnetic waves often suffer amplitude variations (called scintillations) as they propagate through the ionosphere. Amplitude scintillation affects the signal to noise ratio of GPS receiver signals and increases the noise levels in the code and phase measurements. The received GPS signal intensity from a satellite might drop below the receivers tracking threshold, causing the loss of lock on that satellite, resulting in reduced accuracy navigation, cycle slips and data loss. Phase scintillations may also occur and have significant effects on phase-lock loops in GPS receivers, resulting in a loss of phase lock. Plasma irregularities with a scale size smaller than 1 km cause amplitude and phase scintillations of GPS signals. Large-scale electron density structures cause only phase scintillations and are known for their effects such as refraction, signal delay and polarization rotation. This effect increases with the increase in variations of total electron content (TEC). The presence of elongated structures in the F-region ionosphere is the main reason for large-scale variations of TEC. An overview of ionospheric effects on radio wave propagation is shown in Figure 1.3.

L-band space-borne synthetic aperture radar (SAR) provides valuable earth science measurements. A detailed description of SAR is complex and beyond the scope of this thesis. In a typical SAR application, a single radar antenna with a large aperture attached to the space craft flies over the ionosphere radiating a signal that illuminates the terrain underneath the satellite out

towards the horizon. As shown in Figure 1.4, the radar gathers the reflected signals at different times and positions during the flight which are coherently processed to achieve fine spatial resolution images. The presence of large-scale electron density structures in a field view may result in phase scintillations and Faraday rotation of the radio waves, which can cause image defocusing [van de Kamp et al., 2009], geolocation errors, interferometric phase errors and distortions of the signal’s polarimetric signature. Large-scale density structures in the auroral zone have been shown to adversely affect SAR images [Meyer et al., 2006]. In order to develop techniques to correct these images, knowledge of spatial and temporal properties of the irregularities is required.

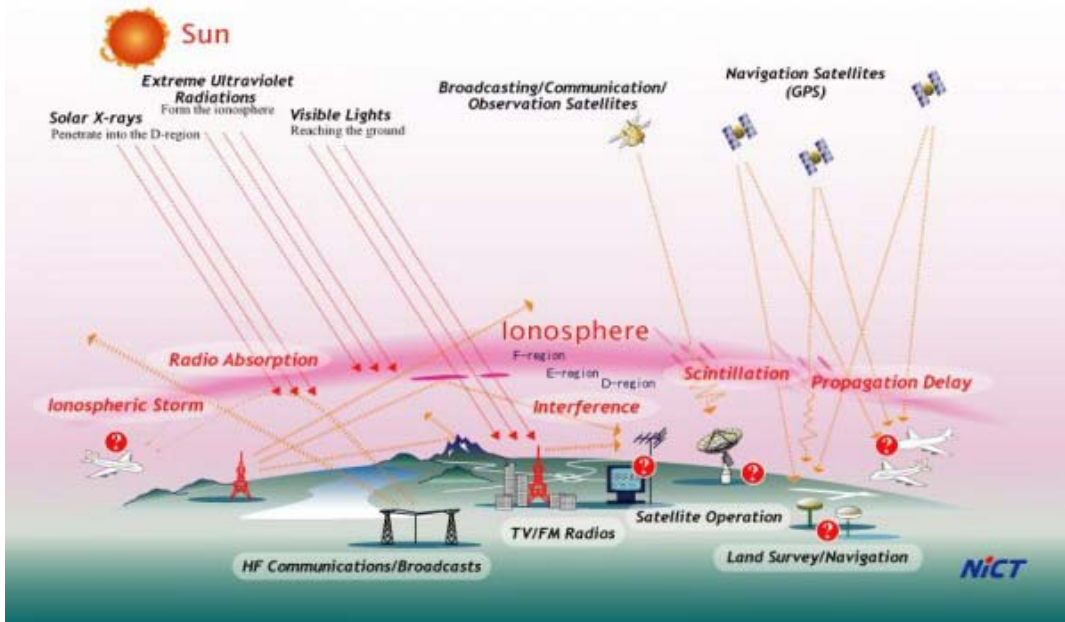


**Figure 1.3:** Ionospheric effects on radio wave propagation.

### 1.3. Historical Review and Objective of Thesis

In 1946, Hey, Parsons and Phillips reported small-scale fluctuations in the intensity of cosmic noise from the direction of the Cygnus constellation which was believed to be the source of fluctuations at that time [Hey et al., 1946]. The Interstellar medium, or terrestrial ionosphere, were also considered as two possible regions responsible for fluctuations of galactic sources [Ryle and Hewish, 1950]. Even though observations made with receivers separated by a short distance showed some correlation, readings taken from widely-spaced receivers revealed no coherency in the fluctuations of radio stars [Bolton and Stanley, 1947; Smith, 1950; Little and Lovell, 1950; Bolton et al., 1953]. These observations led to the assumption that irregular

refraction from the ionosphere is responsible for the radio star scintillations. In 1950, Ryle and Hewish observed radio waves on wave lengths of 3.7 m and 6.7m and concluded that the earth's atmosphere is responsible for irregular refraction of radio waves and also stated that electron density irregularities of the ionosphere might be the reason [Ryle and Hewish, 1950]. In 1951, Hewish used the diffraction mechanism of radio waves received from a radio star to study irregularities in the ionosphere. Based on observations, he deduced that ionospheric irregularities have a sidewise extent of 2-10 km at an altitude of 400 km with irregularities peaking near midnight with an annual variation [Hewish, 1952]. Insufficient observations hampered his method of determining the height based on amplitude and phase fluctuations of radio waves received from the radio stars [Booker, 1958]. The theory of radio diffraction pattern and their application to study the F region ionosphere was discussed in detail by Ratcliffe [Ratcliffe, 1951; Ratcliffe, 1954] and Booker [Booker et al., 1950; Booker, 1958]. Many earlier radio-astronomical studies identified the dependence of variations in the scintillation of radio waves with the time of the day, season, solar cycle, latitude and magnetic activity [Bolton et al.,1953; Booker, 1958; Wild and Roberts,1956; Briggs, 1958; Shimazaki, 1959; Aarons et al., 1966; Smerd and Slee, 1966 and references therein].

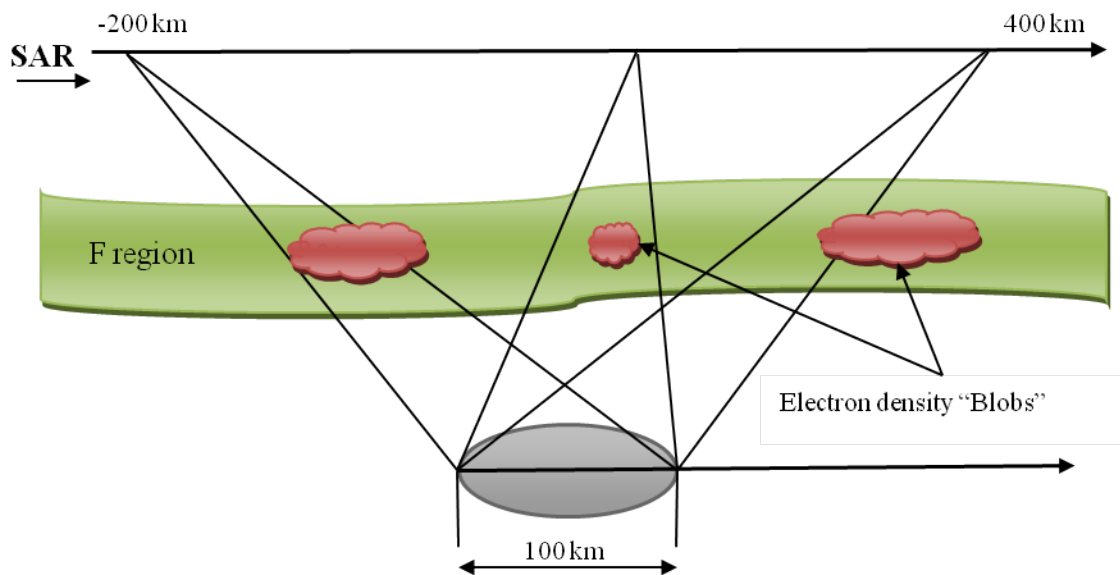


**Figure 1.4:** Synthetic Aperture Radar Imaging concept with the presence of F region electron density blobs.

The success of the first low-altitude satellite, ‘Sputnik 1’, in 1957 triggered the study of E-region and F-region irregularities. Kent (1959) reported that a 40 MHz wave transmitted from ‘Sputnik 1’ as it propagated through the ionosphere experienced fading due to the rotation of the satellite, Faraday rotation of the wave and irregular fading associated with 1 km electron density irregularities and that this fading was observed at latitudes greater than  $50^{\circ}$  N. Kent (1961) later reported similar fading of 108 MHz waves associated with 100 km scale size F-region density irregularities along the magnetic field lines during night time in the equatorial region. Signals recorded from satellites “Sputnik I” and “Sputnik III” exhibited diurnal variations and seasonal variations of scintillation occurrence [Yeh and Swenson, 1959]. Many observations and theoretical studies of radio satellite scintillations associated with spread F, sporadic E and auroral E at low, middle and high latitudes during the years of high and low solar activity at different times, seasons and magnetic activity by using different satellites are reported by many researchers [Yeh and Swenson, 1959; Liszka, 1962a; 1962b, 1963; Singleton and Lynch, 1962; McClure, 1964; Basu et al., 1964; Frihagen and Liszka, 1965; Aarons et al., 1966; Ireland and Preddey, 1967; Aarons et al., 1969; Bandyopadhyay and Aarons, 1970; Hargreaves, 1970; Hargreaves and Holman, 1972; McClure and Hanson, 1973; Davies et al., 1975; Basu et al., 1980 and references there in]. The global morphology of ionospheric scintillations and a complete review of geographical and geophysical effects on the scintillation variations are reviewed by Aarons et al., 1971, Aarons 1982, Yeh and Liu, 1982.

For convenience, it is common to divide the earth into three regions based on geomagnetic latitude. They are

- (1) Low-latitude or Equatorial Region ( $15^{\circ}$ - $25^{\circ}$  either side of the equator)
- (2) High-latitude Region (Pole ward of about  $60^{\circ}$  latitude )
- (3) Mid-latitude Region (The region between high and low latitude regions).

This thesis is mainly addressing the high-latitude ionospheric region that is more dynamic compared to lower latitudes and is the location of the plasma structures that have been measured. As the geomagnetic field runs nearly vertical in the high-latitude region, it is influenced by the magnetosphere and solar wind.

The convection pattern of plasma at higher latitudes is influenced by the orientation and intensity of the interplanetary magnetic field (IMF) [Dungey, 1961]. IMF is a vector quantity with three directional components,  $B_x$ ,  $B_y$  and  $B_z$ . Components  $B_x$  and  $B_y$  are oriented parallel



to the ecliptic plane whereas component  $B_z$  is oriented perpendicular to the ecliptic plane. The  $B_x$  component, which is along the sun-earth line, has subtle effects on the circulation pattern of plasma. Both east-west  $B_y$  and north-south  $B_z$  IMF components have significant effects on the circulation patterns. Coupling between the solar wind and magnetosphere varies widely for different IMF conditions. Southward IMF, or negative  $B_z$ , causes strong coupling between the solar wind and the magnetosphere, which results in transfer of energy, mass and momentum from the solar wind to the magnetosphere. When the IMF is southward, the magnetospheric plasma flow at ionospheric heights resembles a two-cell convection pattern which was first defined by Axford and Hines [1961] and was mapped in detail from satellite observations and various ground-based observations [Heppner, 1972, 1973, 1977; Heelis et al., 1982; Maynard et al., 1982; Heelis, 1984; Heppner and Maynard, 1987]. It has also been studied with ionospheric modeling [Knudsen et al., 1977; Spiro et al., 1978; Watkins, 1978; Quegan et al., 1982; Sojka and Schunk, 1985, 1987; Schunk et al., 1986]. The plasma flows in the ionosphere with speeds of several hundred m/s are commonly observed. Plasma circulation patterns are shown in figure 1.5a. Coupling between the solar wind and the magnetosphere is less during northward IMF conditions and the speed of plasma flow is much lower under these conditions. Several researchers proposed two-cell, three-cell and four-cell convection patterns in order to explain the circulation pattern of plasma flow under certain IMF conditions. An example of a four-cell convection pattern when IMF  $B_z$  is positive is shown in Figure 1.5b.

Enhanced elongated F region plasma structures, known as patches, were first observed over the central polar cap at Thule, Greenland using all-sky imagers and ionosonde data [Weber and Buchau, 1981]. Many other observations using a variety of optical techniques and ionospheric soundings [Buchau et al., 1983; Weber et al., 1984; Weber et al., 1986], Incoherent scatter radar [Kelley and Vickrey, 1984; Foster, 1984, 1989; Foster and Doupnik, 1984; Foster et al., 1985; Moen et al., 2006 and references there in], meridian scanning photometer [McEwen and Harris, 1996], coherent radar [Milan et al., 2002], and modeling studies [Sojka et al., 1994] were reported to explain the formation, evolution and characteristics of patches.

Polar cap patches of ionization with horizontal scale sizes of more than 100 km are thought to be formed on the dayside by solar extreme-ultraviolet (EUV) radiation [Foster 1984, 1989, 2005; Buchau et al., 1983; Anderson et al., 1988; Sojka et al., 1993; Sojka et al., 1994; and references therein] or by energetic particle precipitation [Weber et al., 1984; Rodger et al., 1994;

and references therein] in the cusp region or in subauroral latitudes. For southward IMF conditions, Patches thus formed convect over the polar cap with  $E \times B$  drift velocity from the noon to midnight sector and exit the polar cap during midnight [Carlson, 1994, 2012]. Under northward IMF conditions, sun-aligned arcs, or theta auroras, or transpolar arcs, are often observed over the polar cap ionosphere [Buchau et al., 1983]. Figure 1.6 shows the dynamics of the polar cap under different IMF conditions. The black lines represent the corrected geomagnetic latitude and local time with the red auroral oval superimposed on it for reference. Blue lines indicate the circulation pattern of plasma flow. Figure 1.6(a) shows patches with a horizontal spatial scale size of around 1000 km surrounded by lower density plasma produced in the cusp region moving in the anti-sunward direction with a speed of around 1000 m/s across the polar cap to join the return sunward flow patterns under southward IMF  $B_z$  and positive  $B_y$  conditions. Changes in  $B_y$  introduces a dawn-dusk symmetry.

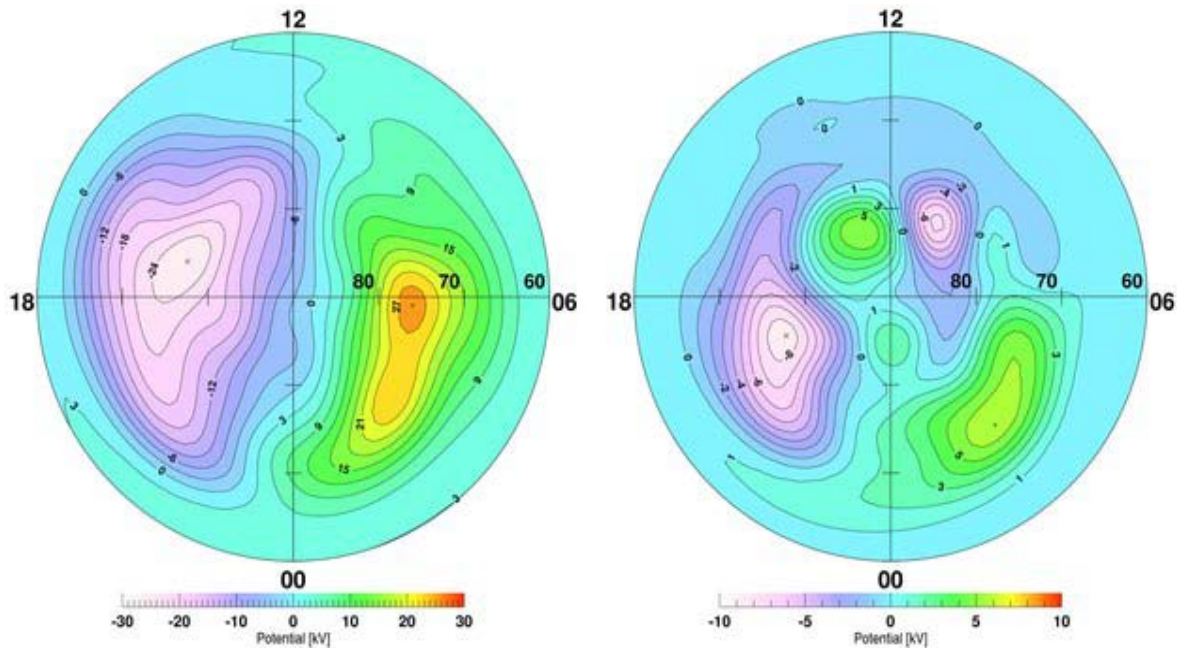


**Figure 1.5:** Plasma Convection at high-latitude (a) Basic two-cell convection pattern under southward IMF conditions. (b) An example of four-cell convection pattern under northward IMF conditions.

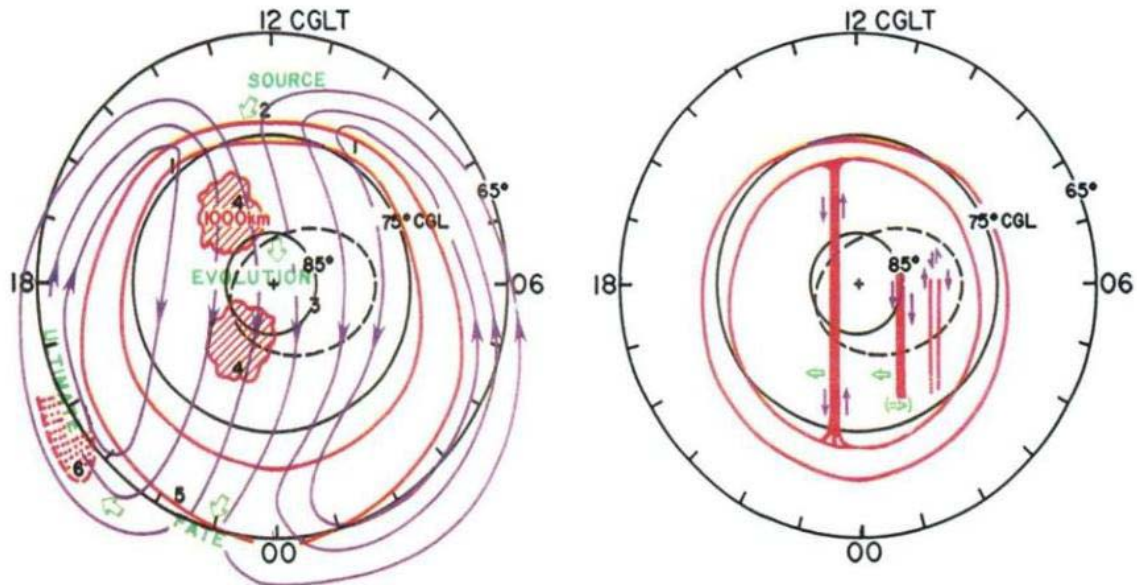


**Figure 1.6:** Irregular structures in the polar cap ionosphere (a) Patches drifting anti-sunward during Southward IMF state (b) Sun-aligned arcs or theta auroras with Dawn-Dusk drift observed during Northward IMF state. [After Carlson 1994]

This thesis principal interest lies in the larger structures with approximate sizes ranging from 10-300 km that are present in the auroral zone F-region ionosphere during the evening. The first incoherent-scatter radar observations of plasma enhancements in the auroral zone were made at Chatanika by Banks et al., [1974]. Coordinated observations using radar and TRIAD satellite data of VHF scintillations resulting from F-region ionization enhancements were reported by Vickrey et al., [1980] and Vickrey [1981]. Later, many studies addressed the production mechanisms and properties (spatial extent, motion, temperatures) of auroral zone blobs using a variety of experimental techniques coordinating with the Chatanika incoherent scatter radar [Kelley et al., 1982; Muldrew and Vickrey, 1982; Rino et al., 1983; Robinson et al., 1985; de la Beaujardière et al., 1985; Weber et al., 1985; and references there in] and EISCAT radar [de la Beaujardière et al., 1985; Hargreaves et al., 1985; Tsunoda et al., 1985; Hargreaves and Burns, 1988; Wang et al ., 1990 ; Burns and Hargreaves, 1996; Pryse et al., 1996; and references therein] were reported. A number of theories proposed to explain the production mechanism of irregularity structures were reviewed by Tsunoda [1988]. The most accepted source mechanisms are:

- (a) Polar cap patches that are formed on the day-side of the earth by solar radiation or energetic particle precipitation in the cusp region move antisunward across the polar cap with the ExB drift velocity from noon to midnight. As F-region plasma has long chemical

recombination times, polar cap patches then convect into the night side auroral zone forming east-west elongated structures known as blobs [Robinson et al., 1985; Weber et al., 1985; and references therein].

- (b) Particle precipitation in the polar cap or auroral zone produce blobs in the evening auroral zone [Kelley et al., 1982].

Figure 1.7 shows the electron density contour map as a function of altitude and latitude measured by Chatanika radar while the antenna was swept in the magnetic meridian plane. This plot shows a series of electron density enhancements, or blobs, with a horizontal scale-size ranging around 50-100 km located nearly overhead of the radar site. Figure 1.7 suggests the presence of a range of density scale sizes. However to derive these data, the radar, which used a large mechanically movable dish, was slowly scanned in the north-south direction in a time span of several minutes. Since the ionization in the auroral zone is usually moving east-west with speeds of several hundred m/s, it was not possible to derive scale size values. There is a new radar facility at Poker Flat where the phased-array permits measurements in several directions nearly simultaneously. This new capability provides both the east-west velocity and electron density range profile data. The combination of both density and velocity data with very good time resolution can then be used to derive scale-size values of density structures. The next chapters will explain the method in more detail.

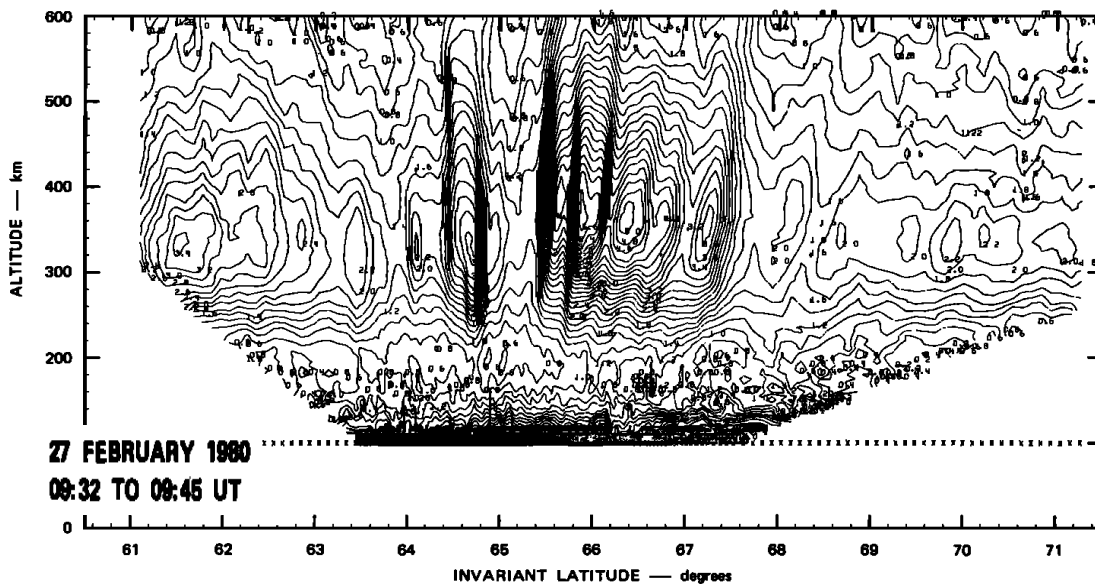


**Figure 1.7:** Altitude/latitude variation of electron density in the midnight sector auroral zone measured by the Chatanika incoherent scatter radar [From Kelley et al., 1982].



## CHAPTER 2. INCOHERENT SCATTER RADAR

### 2.1. Introduction

Incoherent-scatter radar (ISR) is one of the most powerful ground-based remote sensing techniques capable of measuring a wide variety of ionospheric plasma parameters. Electromagnetic waves transmitted by high-power radio transmitters are weakly scattered by thermal fluctuations of the electrons, i.e. incoherent scatter, in the ionosphere and are collected by using large aperture radar receivers. Incoherent-scatter radar measures the basic parameters of the backscattered signal such as (a) Power as function of range [Farley, 1969a], (b) Faraday rotation angle as a function of altitude [Farley, 1969b] and (c) Power spectrum, or Frequency spectrum or the autocorrelation of the received signal as a function of range [Farley, 1969c]. Several plasma parameters, such as electron density, ion and electron temperatures, line-of-sight (LOS) velocities (can be transformed to ion drift velocity), ion mass and ion-neutral collision frequencies can be determined by fitting or comparing the theoretical spectrum to the measured spectrum of the scattered radiation.

Over the years, with advances in technology, traditional incoherent-scatter radars have been replaced by phased-array technologies that can provide high-time and spatial resolution measurements and less space-time ambiguity overcoming the disadvantages of traditional incoherent-scatter radars. The basic concepts and measurement techniques for determining the plasma parameters are still the same. This chapter briefly discusses the incoherent-scatter radar theory, basic modulation technique, advantages of the phased-array radar over traditional incoherent-scatter radar, determination of electron density and evaluation of ion velocity with an example.

Over 50 years ago, the incoherent-scatter radar technique came into existence when in 1958 W. E. Gordon pointed out that scattering of radio waves from free electrons can be detected by using powerful radar. He also predicted that the backscattered signal is Doppler broadened in frequency, corresponding to thermal motion of electrons in the plasma [Gordon, 1958]. Enormous sensitivity is required for estimating the Doppler broadening associated with the electrons. For this very purpose Gordon proposed the construction of the Arecibo observatory with 305 meter diameter antenna. Before the completion of Arecibo observatory, Bowles [1958], using 20 MW acre system with a 41-MHz pulse transmitter and Pineo, Kraft and Briscoe [1960], using 84-foot-diameter antenna with a 440 MHz pulse transmitter observed incoherent scatter

from electrons with expected amount of power density but with a much narrower spectral width (around 5-10 %) than predicted by Gordon. As Coulomb's force of attraction exists between the ions and electrons in the plasma, narrower spectral width or Doppler broadening of the scattered signal corresponds to the speed of much heavier and slower ions rather than that of electrons [Bowles, 1959; Dougherty and Farley, 1960; Fejer 1960a,1960b]. Gordon also expected the spectrum of the scattered electromagnetic signal to be Gaussian, which was later modified and demonstrated to have a double-humped spectrum distributed on both sides of the transmitted frequency. Due to electrostatic coupling between electrons and ions, the random thermal motion of electrons produces ion-acoustic waves and plasma waves. The double-humped shape of the spectrum is due to ion acoustic waves travelling towards and away from the radar and is shifted slightly up or down in frequency, which gives a measure of line-of-sight bulk-plasma velocity. Theories for incoherent scatter from the ionosphere were developed in parallel by several researchers [Fejer, 1960a, 1960b; Dougherty and Farley, 1960, 1963; Salpeter, 1960a, 1960b, 1961; Hagfors, 1961; Rosenbluth and Rostoker, 1960, 1962; Farley et al., 1961; Farley, 1966; Bekefi, 1966; Farley,1971; Swartz and Farley, 1979; and references therein].

Radar (Radio Detection and Ranging) is an electrical system which transmits short pulses of electromagnetic (EM) signals towards a point of interest and receives the reflected EM waves to determine the basic properties (like range, direction, and doppler shift i.e. speed/velocity) of a target. The amplitude of the received signal measured by the radar depends on the nature of the targets (shape, size and composition). The amplitude of the received signal will be high if the target is a hard target (e.g. aircraft, ship, spacecraft, and guided missile) and will be low if the target is a soft target (e.g. rain, fog, electrons). Doppler radars are also capable of measuring the Doppler shift in frequency of the received power, which determines the velocity of the target. If the target is moving away from the radar, the frequency of the received echo will be less than the frequency of the transmitter and vice versa. In the case of incoherent-scatter radar the target is a collection of a vast number of ionospheric electrons filling the radar beam. The electric field component of the incident-wave puts the free electrons into oscillatory motion. The oscillating electrons act like Hertzian dipoles re-radiating the electromagnetic waves very weakly [J.J Thomson, 1906]. The scattering cross-section of a single electron is given by

$$\sigma_e = 4\pi r_e^2 \sin^2 \theta \approx 10^{-28} m^2 \quad (2.1)$$

where  $\sigma_e$  = Radar cross section of a single free electron

$r_e$  = Classical electron radius of the earth =  $2.8 * 10^{-15}m$

$\emptyset$  = Angle between the incident electric field and observer =  $\frac{\pi}{2}$  (for backscatter).

This scattering cross-section is appropriate for cases where the radar wavelength is significantly less than the plasma Debye length (which is not normally applicable in the ionosphere for radars used in our research). The scattering process is usually termed “Thomson Scatter”. For cases where the radar wavelength is greater than the plasma Debye length the scattering is termed “Collective Thomson Scatter” or “Incoherent Scatter” and the scattering cross-section is one half the Thomson cross-section.

All the electrons present in the finite volume of the radar beam illuminated by the incident wave have statistically independent, random thermal motions and scatter signals with phases that are unrelated to each other. Thus, the received signal will simply be equal to the sum of the reflected power (rather than voltages) of each electron in the radar field of view, and the average radar cross-section will be equal to the product of electron density ( $N_e$ ) and the cross-section of the electron. The average cross-section of the unit volume is given by

$$\sigma_{avg} = N_e * \sigma_e \quad (2.2)$$

where  $N_e$  = Electron density (varies with range)

$\sigma_{avg}$  = Average scattering cross-section per unit volume

$\sigma_e$  = Scattering cross-section/ Thomson cross-section of a single electron.

However, the ionospheric plasma contains both electrons and ions that are accelerated by the incident electric field. Since the mass of electrons is less than the ions, electrons are accelerated more than ions and thus the scattering is effectively from the electrons. Since ions and electrons are electrostatically coupled to each other, electron-ion collective effects must be included in determining the incoherent radar cross-section. Two main approaches for calculating the scattering characteristics of plasma are

- a) The dielectrically screened (“Dressed”) test particle approach [Fejer, 1960a, 1960b; Hagfors, 1961; Rosenbluth and Rostoker, 1960, 1962 ; Bekefi, 1966, etc]



- b) The plasma wave approach [Dougherty and Farley, 1960, 1963; Farley et al., 1961; Farley, 1966; Swartz and Farley, 1979; and references therein]

The dressed-test particle approach is a microscopic approach based on the application of plasma kinetic theory. The scattering characteristics of plasma are calculated by placing a charged particle in plasma and by considering the collective efforts of all the plasma particles. Comparing the radar wavelength to Debye length, the scattering is considered to be either from individual electrons (Thompson Scatter) or due to the collective efforts of plasma (Incoherent Scatter) where electron clouds around the ion screen the electric fields. Debye length or shielding distance  $\lambda_D$  is a measure of plasma's ability to shield out electric potentials that are applied to it. The Debye length  $\lambda_D$ , or thickness of sheath (thickness of the electron cloud around the positively charged ions), is given by

$$\lambda_D = \left( \frac{\epsilon_0 K_B T_e}{N_e q_e^2} \right)^{1/2} = 69 \left( \frac{T_e}{N_e} \right)^{1/2} m \quad (2.3)$$

where  $\lambda_D$  = Debye length or shielding distance in meters

$N_e$  = Electron density in  $m^{-3}$

$\epsilon_0$  = Permittivity of the free space  $\approx 8.85 * 10^{-12} F \cdot m^{-1}$

$T_e$  = Electron Temperature in K

$K_B$  = Boltzmann constant  $\approx 1.38 * 10^{-23} JK^{-1}$

$q_e$  = Charge of an electron  $\approx 1.6 * 10^{-19}$  Coulombs.

At 100 km of altitude, substituting typical values of electron density ( $N_e \sim 10^9 m^{-3}$ ) and electron temperature ( $T_e \sim 300$  k) in the above equation gives a Debye length of 4 cm. Similarly, the Debye length has approximate values of 0.22 cm at 300 km of altitude (the approximate height of F-region peak) and 10cm at 1000 km of altitude.

When the radar wavelength is smaller than the Debye length, no shielding is offered by the ions and Thompson scattering from individual electrons is applicable. When the radar wavelength is longer than the Debye length, ion shielding and collective behavior of plasma has to be taken into account. For this latter case the wavelength of the radar probing the ionosphere will be much larger than that of the Debye length, so scattering from the individual electrons can

no longer be considered. The scattering coefficient per unit volume [Fejer, 1960a, 1960b] based on the dressed-test particle approach is given by

$$\sigma_{avg} = Ne \cdot \sigma_e \cdot \left( \frac{[4\pi\lambda_D \sin \phi/2]^2 + \lambda_R^2}{[4\pi\lambda_D \sin \phi/2]^2 + 2\lambda_R^2} \right) \quad (2.4)$$

where  $\sigma_{avg}$  = Average scattering cross-section per unit volume

$\lambda_R$  = Wavelength of the radar

$\phi$  = Scattering angle.

When  $\lambda_R$  is smaller than the Debye length, the above equation reduces to the value as predicted by Gordon

$$\sigma_{avg} = Ne \cdot \sigma_e. \quad (2.5)$$

When  $\lambda_R$  is larger than the Debye length, the reflected power will be half of the value as predicted by Gordon and the scattering coefficient per unit volume is given by

$$\sigma_{avg} = \frac{1}{2} \cdot Ne \cdot \sigma_e. \quad (2.6)$$

The factor of  $\frac{1}{2}$  arises because the cross-section per electron for incoherent-scatter is one half the cross-sections for the Thomson scatter  $\sigma_e$ . The plasma-wave approach is a macroscopic approach based on the Nyquist noise or fluctuation-dissipation theorem [Dougherty and Farley, 1960, 1963]. In this approach, the scattering due to fluctuations in the refractive index is considered in contrast to the dressed-test particle approach where the scattering from individual particles is considered. The fluctuations in the refractive index are proportional to the residual thermal fluctuations of the electron density. Using the analytical method of integration employed by Daugherty and Farley (1960), Buneman (1962) provided a good approximation to the scattering cross-section which is given by

$$\sigma = \sigma_e \left[ \frac{K^2 \lambda_D^2}{1 + K^2 \lambda_D^2} + \frac{1}{(1 + K^2 \lambda_D^2)(1 + K^2 \lambda_D^2 + Tr)} \right] \quad (2.7)$$

where  $\sigma$  = effective radar scattering cross-section

$\sigma_e$  = Scattering cross-section of an electron (Thompson Scatter)

$K$  = Radar wave number =  $4\pi/\lambda_R$

$Tr = Te/Ti$  = Ratio of electron temperature to ion temperature.

The two terms in the above equation refer to the “plasma-line” and “ion-line” portions of the incoherent-scatter spectra, respectively. Plasma-line returns correspond to the “high-doppler shifted frequency” terms of the ISR spectrum and arise due to the signal scattered from the high frequency electron waves or Langmuir waves. The upshifted and downshifted plasma lines are due to Langmuir waves travelling towards and away from the radar. Ion-line returns correspond to the “low-doppler shifted frequency” terms of the ISR spectrum and arise due to the signal scattered from ion acoustic waves. The upshifted and downshifted ion lines are due to the ion acoustic waves travelling towards and away from the radar.

Thermally generated ion lines are attenuated by a process called Landau damping, which results in the broadening of the spectral lines. The broadening of the spectral lines of ion-acoustic waves is sufficient to make them merge into a single, double-humped spectrum. The degree of damping is strongly affected by the ratio of electron to ion temperatures. Ion lines are spectrally compact and typically spread over a few kilohertz to a few tens of kilohertz around the transmitter frequency. Figure 2.1 shows the incoherent scatter spectra with Landau-damped ion-acoustic lines and plasma-lines. It can be clearly seen that the two spectral ranges are well separated because of the variation in the mass of ions and electrons.

Both the theories, i.e. the dressed-test particle approach and the plasma wave approach, have been shown to attain approximately the same results [Evans, 1969]. Most of the theoretical results along with experimental techniques and results involving ionospheric studies were reviewed by Evans (1969), Farley (1971), Brekke (1977) and Nygren (1996). Power corresponding to the plasma-line is very weak and difficult to detect, therefore it is often neglected while making routine ISR measurements. The plasma-line of the power spectrum, i.e. electronic component, is not discussed here.

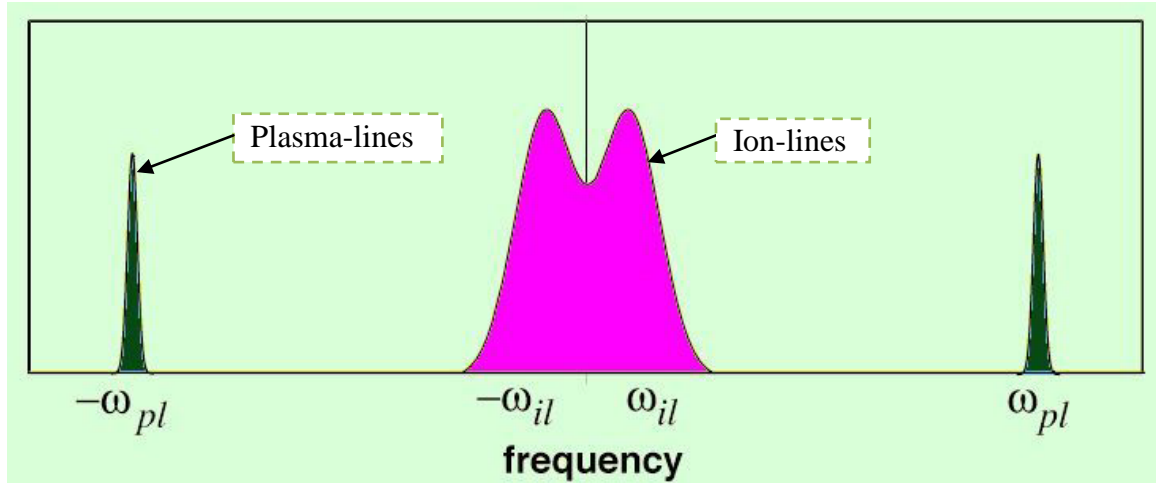


**Figure 2.1:** Typical power spectrum of the signal received as a function of frequency showing both upshifted and downshifted ion-lines and plasma-lines.

The shape of the ion-line in the ISR spectrum depends on various plasma parameters, such as ion and electron temperature, ion composition, ion-neutral collision frequency and ion-drift velocity. The spectral shape can, for example, be calculated by using expressions from the theoretical developments of Dougherty and Farley (1960, 1963). The theoretical approach is not discussed here; however a qualitative approach of how these plasma parameters affect the spectrum shape is discussed next. The width of the ion-line spectrum is proportional to the ratio of ion temperature ( $T_i$ ) to ion mass ( $m_i$ ). Figure 2.2 shows the broadening of ion-line spectrum with increasing ion temperature. Figure 2.3 indicates that the width of the spectrum gets narrower as the ion mass increases. The electron to ion temperature ratio ( $T_r = T_e/T_i$ ) affects the “peak-to-valley” ratio. Figure 2.4 shows the deepening of the central minimum with an increase in electron temperature. As the electron temperature increases above the ion temperature, the Landau-damping decreases and the two ion lines separate. The overall shift of the incoherent-scatter spectrum from the zero-center frequency gives the measure of bulk plasma velocity. Figure 2.5 shows the variation of the incoherent-scatter spectrum for different Doppler shifts. Ion-neutral collision frequency also affects the shape of incoherent-scatter spectrum; high ion-neutral collision frequency results in a narrower spectrum and as the ion-neutral collision frequency reduces, the spectral width increases as shown in the figure 2.6. The electron density is proportional to the area under the spectrum. All the plasma parameters can be calculated using either the power spectrum or autocorrelation function as they form a Fourier transform pair.

Figure 2.7 provides an overall picture of the effect of various plasma parameters on the spectrum shape.

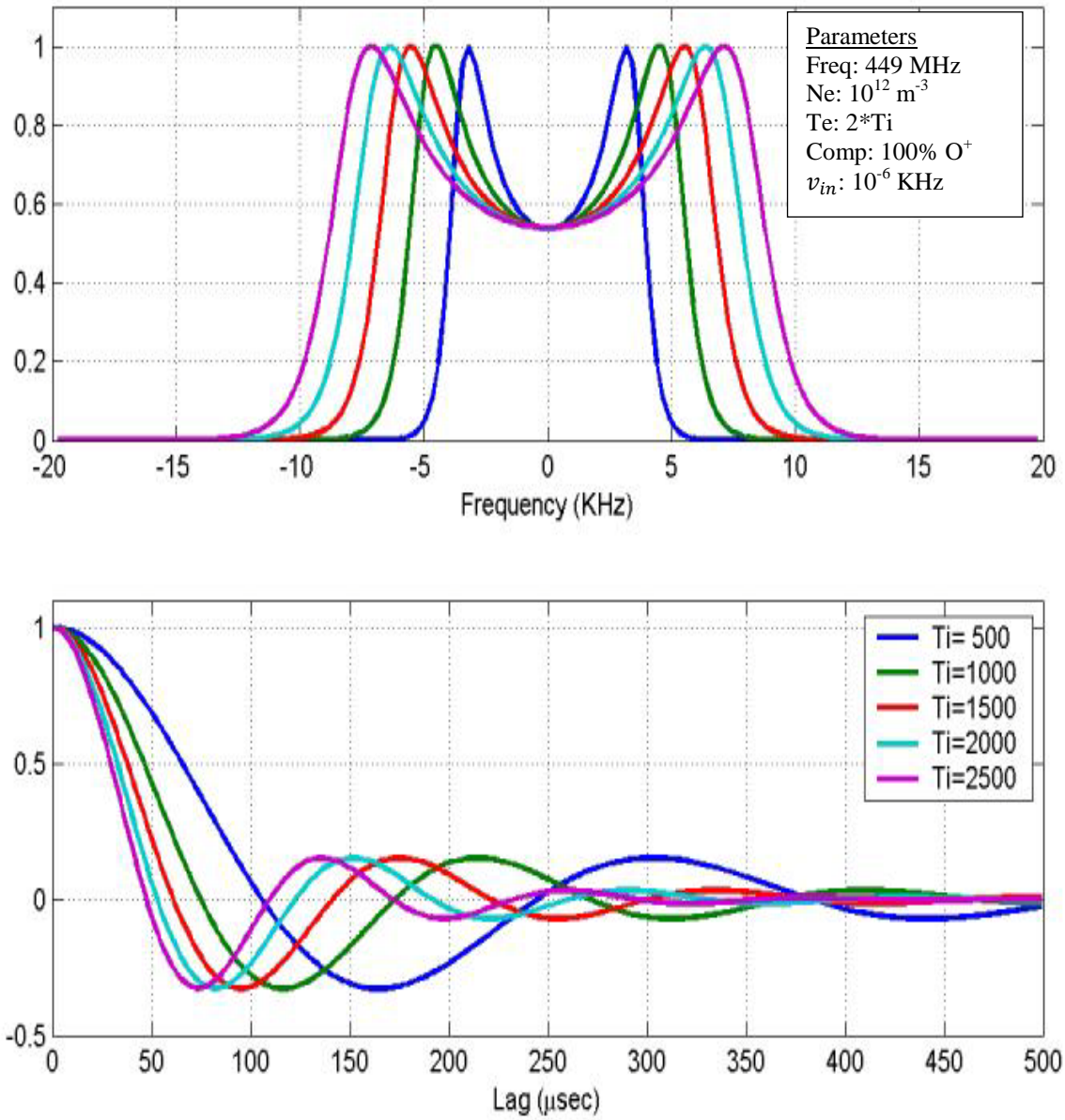


**Figure 2.2:** Dependence of the shape of the ISR ion-line spectrum and autocorrelation function on ion temperatures ( $T_i$ ). [Courtesy of C.J. Heinselman]

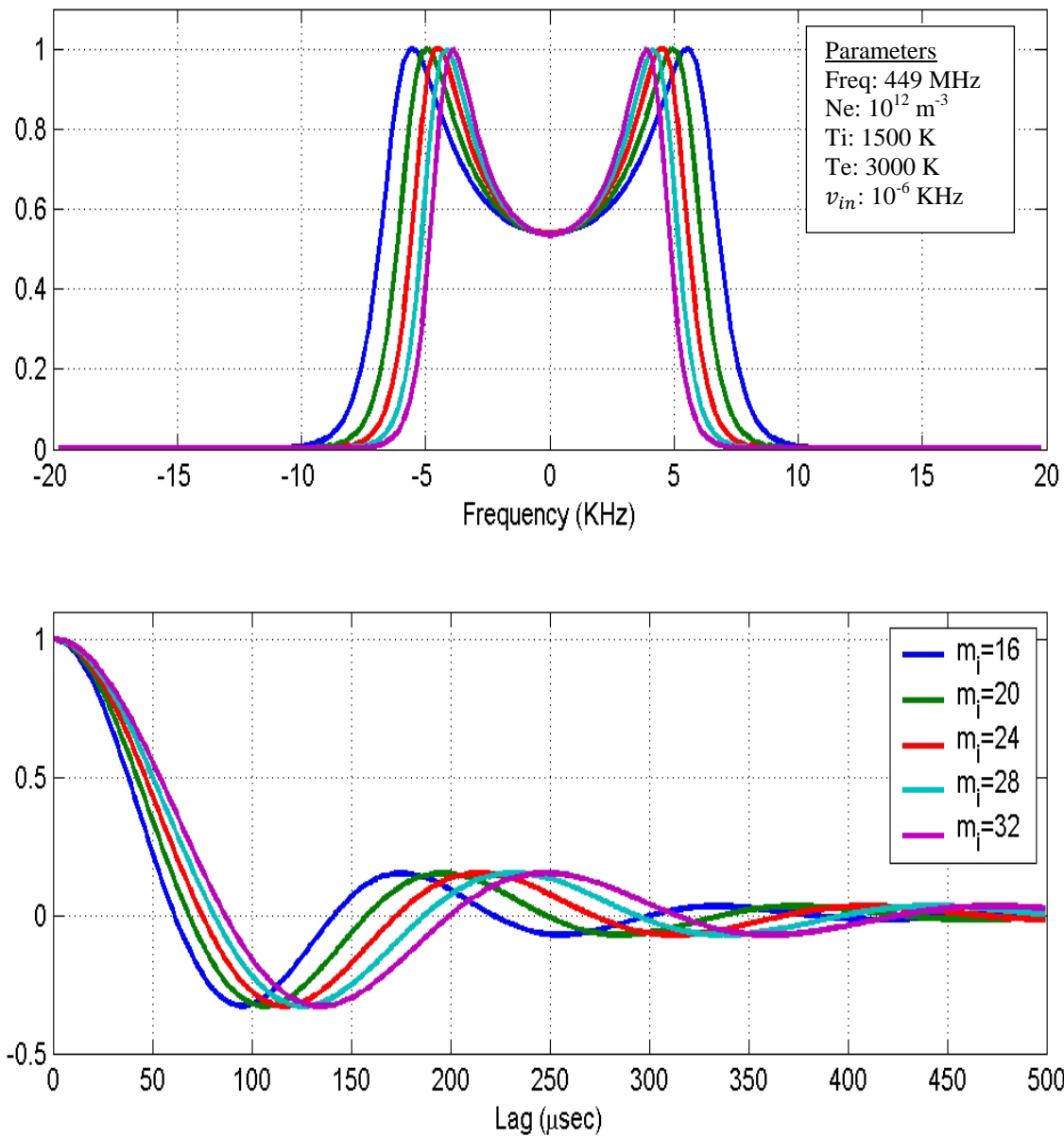


**Figure 2.3:** Dependence of the shape of the ISR ion-line spectrum and autocorrelation function on ion mass ( $m_i$ ). [Courtesy of C.J. Heinselman]

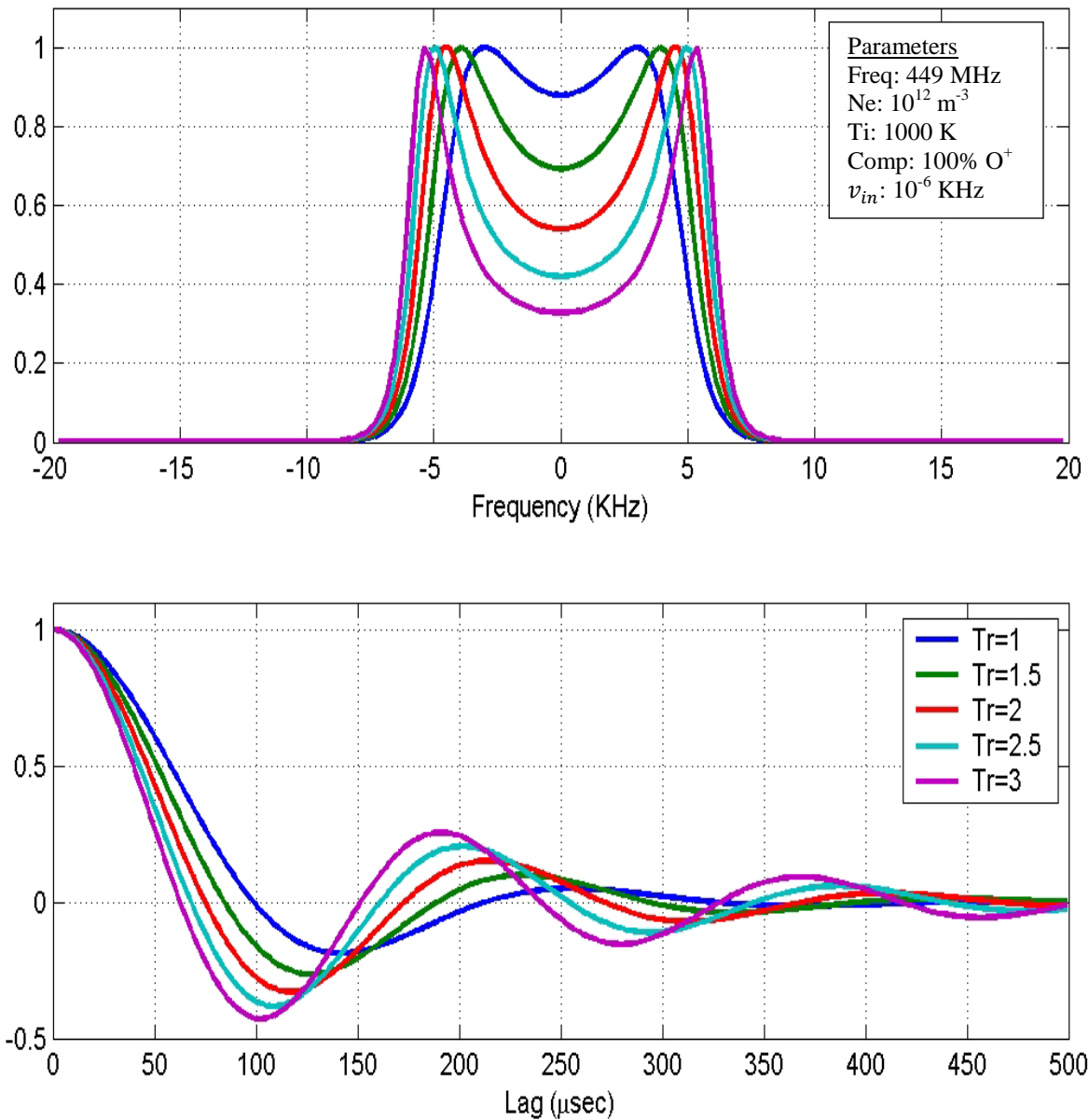


**Figure 2.4:** Dependence of the shape of the ISR ion-line spectrum and autocorrelation function on electron to ion temperature ratio ( $Tr$ ). [Courtesy of C.J. Heinselman]

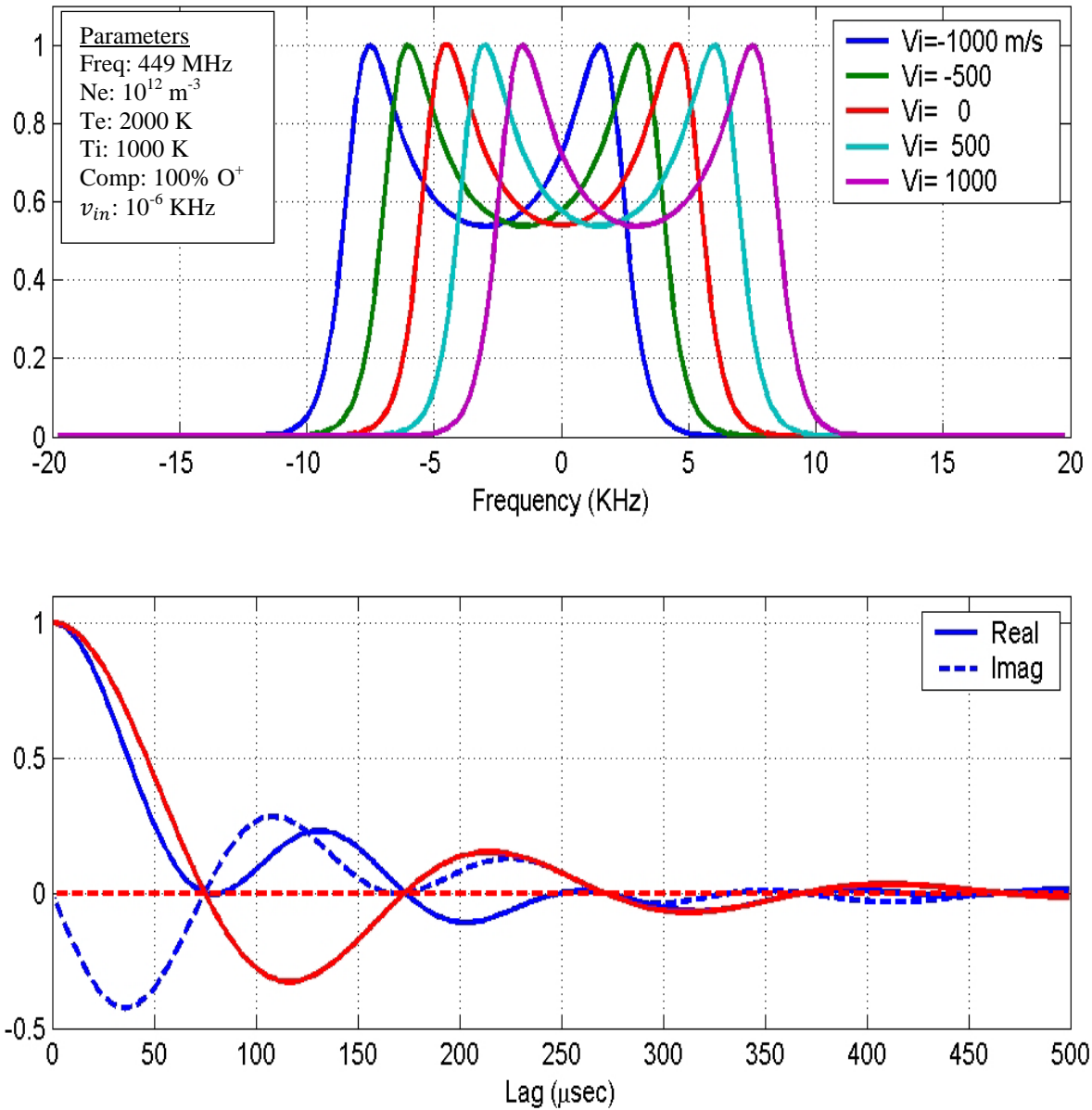


**Figure 2.5:** Dependence of the shape of the ISR ion-line spectrum and autocorrelation function on Doppler shift. [Courtesy of C.J. Heinselman]



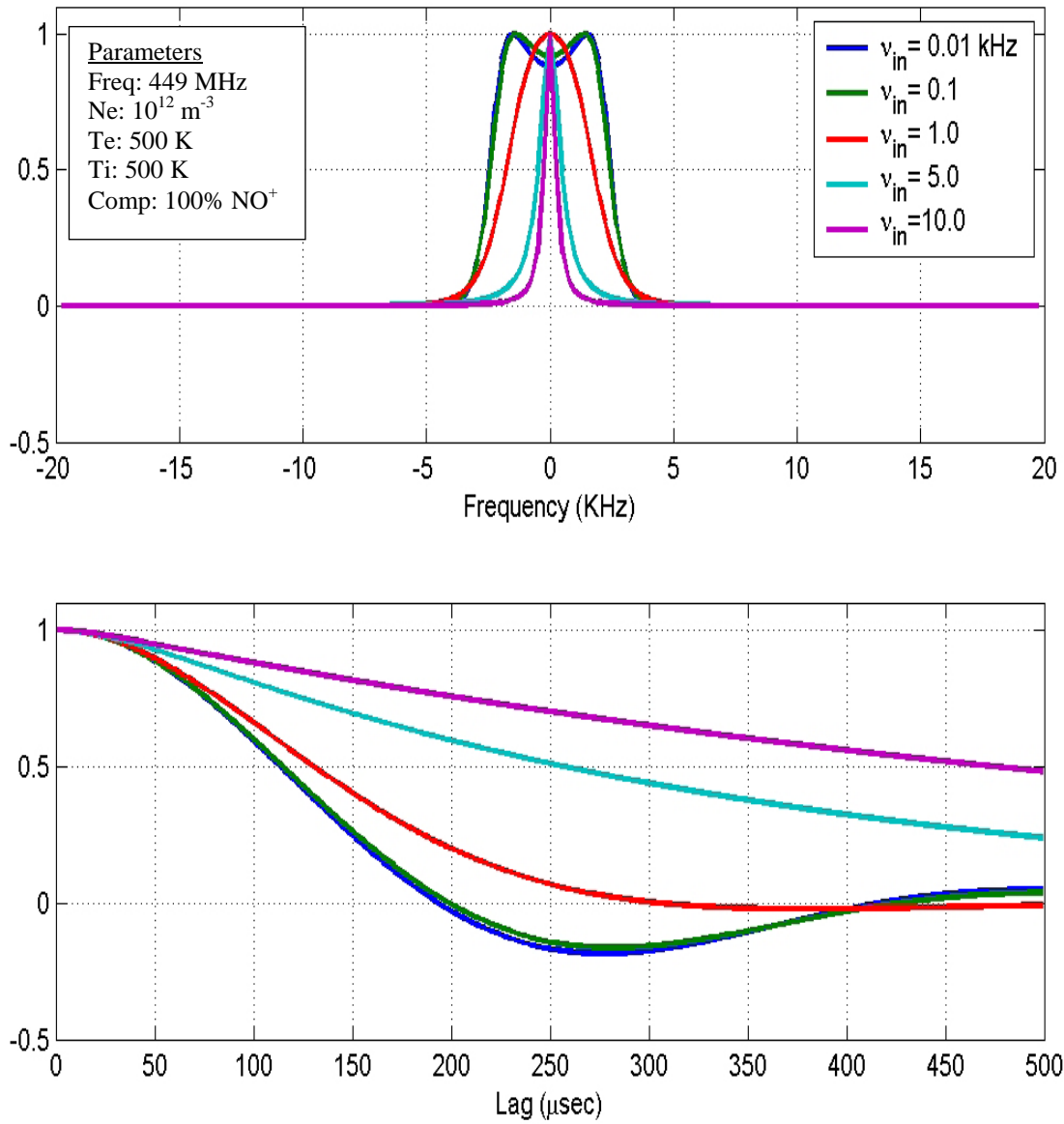


**Figure 2.6:** Dependence of the shape of the ISR ion-line spectrum and autocorrelation function on ion-neutral collision frequency. [Courtesy of C.J. Heinselman]

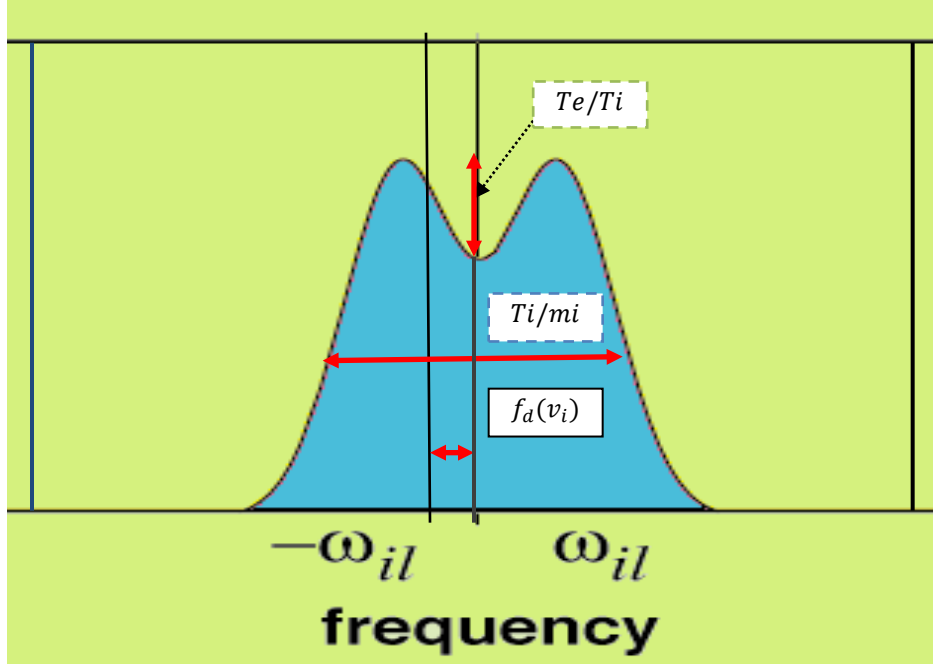


**Figure 2.7:** Overall picture of the power spectrum dependence on various plasma parameters.

## 2.2. Determination of Electron Density

In monostatic radar, pulses are transmitted (possibly with a certain modulation) for a brief period of time and the scattered pulses reflected from the scattering volume are received during a subsequent reception period. Power captured by the receiving antenna when a pulse of duration  $\tau_p$  is transmitted with peak power  $P_t$  is given by the incoherent scatter radar equation [Evans, 1969] and can be written as

$$P_r(r) = \frac{0.76LC A_e P_T \tau_p \sigma_{avg}}{8\pi r^2} = \frac{0.38LC A_e P_T \tau_p \sigma N_e(r)}{4\pi r^2} \quad (2.8)$$

where  $P_T$  = Peak transmitter power in MW

$P_r$  = Power received from a scattering volume at a range  $r$

$A_e$  = Antenna's effective aperture in  $m^2$

$c$  = Speed of light  $\approx 3 \cdot 10^8$  m/s

$L$  = Transmission system loss

$\tau_p$  = Pulse width

$N_e$  = Electron density at a given range  $r$

$\sigma$  = per-ion scattering cross-section calculated from plasma theory.

Neglecting the plasma-line signals, a simple approximation for per-ion scattering cross-section from plasma theory can be written as

$$\sigma = \sigma_e \left[ \frac{1}{(1+\alpha^2)(1+\alpha^2+Tr)} \right] \quad (2.9)$$

where  $\alpha = K\lambda_D = 4\pi\lambda_D/\lambda_R$ .

Power received from the ion-line is given as

$$\begin{aligned} P_r(r) &= \frac{0.38LcA_e\sigma_e P_T\tau_p}{4\pi} \frac{Ne(r)}{r^2 (1+\alpha^2)(1+\alpha^2+Tr)} \\ &= \frac{1}{C_s} \frac{P_T\tau_p}{r^2} \frac{Ne(r)}{(1+\alpha^2)(1+\alpha^2+Tr)} \end{aligned} \quad (2.10)$$

where  $C_s = \frac{4\pi}{0.38LcA_e\sigma_e}$  is a system constant and can be calculated by substituting the radar system parameters, in practice it is often more easily calculated by comparing the ion-line power measurements with peak density estimated using plasma-line measurements [Heinselman, 1999]. The electron density can be estimated from the received power and can be written as

$$Ne(r) = (C_s) \left( \frac{1}{P_T\tau_p} \right) (r^2 P_r(r)) [(1 + \alpha^2)(1 + \alpha^2 + Tr)]. \quad (2.11)$$

The received signal is usually no more than a few times larger than the noise level. Therefore, a careful measurement of received power is required. A calibrated pulse with known amplitude is injected during a time when no ionospheric signal is present, and receiver noise is also estimated in order to account for gain and noise power changes. All the measurements are time-averaged in order to get good estimations. The received power at a range R can be determined by the following equation

$$\overline{P}_r(r) = \frac{K_B T_{cat} B}{\overline{S}_c - \overline{S}_n} (\overline{S}_r(r) - \overline{S}_n)$$

where  $\overline{S}_r$  = Time averaged measured power at a range  $r$

$K_B$  = Boltzmann constant

$T_{cal}$  = Noise pulse temperature injected by the calibrated pulse

$B$  = Receiver bandwidth

$\overline{S_c}$  = Time averaged calibrated power

$\overline{S_n}$  = Time averaged Noise Power.

An initial estimate of electron density, known as raw electron density, without accounting for the effects of  $Tr$  and  $\alpha$  is often calculated with an assumption that the radar wavelength is much greater than the Debye length, i.e.  $\alpha \rightarrow 0$ , electron-to-ion temperature ratio  $Tr \approx 1$  using a relation

$$Ne'(r) = \frac{2C_s}{P_T \tau_p} r^2 P_r(r).$$

Here  $Ne'$  is the raw electron density at a particular range that is determined without temperature corrections. Figure 2.8 shows the plot of received power and raw electron density measured using PFISR with a transmitter peak power of 1.72 MW, a long pulse with pulse width of 480  $\mu$ s and an integration of 2 mins (around 5000 pulses).

After calculating the raw electron density, the value is corrected using the electron-to-ion temperature ratio  $Tr$ , which is calculated by fitting the measured spectrum to the theoretical spectrum. When the electron temperature is considerably larger compared to the ion temperature, the raw  $Ne$  underestimates the true density. Electron temperature rarely becomes larger than ion temperature in the high-latitude and the polar region. For densities of order  $\sim 3 \times 10^{11} \text{ m}^{-3}$ , the difference between the raw  $Ne$  and fitted  $Ne$  is approximately equal to uncertainty of the fitted  $Ne$  [Pedersen et al., 1998]. This thesis therefore uses raw  $Ne$  measurements to study electron density irregularities in high-latitude region. The method of calculating electron temperature  $Te$  and ion temperature  $Ti$  is beyond the scope of this thesis and will not be discussed here.

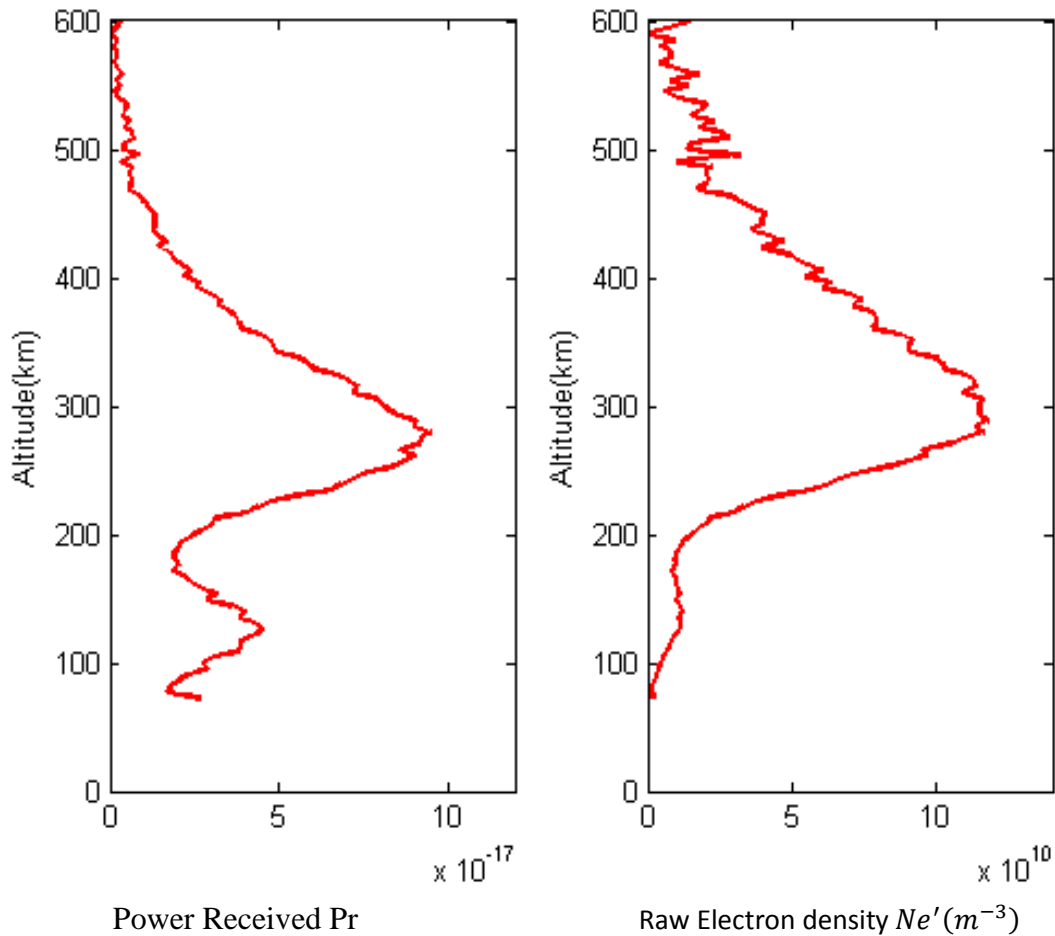


**Figure 2.8:** The left panel shows received power as a function of altitude using an integration of 5000 samples and the right panel shows the electron density (without temperature corrections) plot as a function of altitude calculated after range corrections.

### 2.3. Basic Experiment Design and Estimation of Line-of-sight Velocity

The signal received from a certain altitude is temporally correlated over a short period of time and is totally independent of the signal received after that time and from other non-overlapping regions. Therefore, plasma parameters are to be estimated accurately with good range resolution and time resolution. Over the past few decades, various modulation patterns were proposed by several researchers to increase the performance of the radar and to meet resolution requirements for different purposes. Various modulation schemes like Long Pulse, Multipulse [Farley, 1972; Hagen and Farley, 1973; Rino et al., 1974], Pulse compression codes like Barker codes [Ioannidis and Farley, 1972; Gray and Farley, 1973; Zamlutti, 1980; Huuskonen et al., 1988; Huuskonen and Turunen, 1990], Coded long pulse techniques using

random codes [Sulzer, 1986] and Alternating codes [Lehtinen, 1986; Lehtinen and Häggström, 1987; Sulzer, 1989, 1993; Lehtinen and Huuskonen, 1996; Nygren and Markkanen, 1997] have been used to attain improved range resolution that can be used for specific purposes. Vast literature about these modulation schemes is available in the above mentioned references and various other standard textbooks and is not discussed here.

This thesis uses a basic radar pulse scheme often employed in incoherent-scatter measurements i.e. the simple, unmodulated long-pulse. The long-pulse technique is a method widely used to study the F region, and for our data, has a pulse width on the order of 400-500 micro-seconds, which provides a spatial resolution of 60-75 kilometers. Since the scattering volume is very high, this technique provides a very good signal-to-noise ratio. The drawback of the long-pulse technique is that it heavily filters out the spatial details of the target due to its poor range resolution.

The signal received has a band-limited spectrum centered on transmitter frequency which is shifted to lie around zero frequency by complex mixing. After passing through various stages of amplifiers and filters, the signal is digitized by using an analog-to-digital converter and is either sent to the correlator for calculating the autocorrelation function or the spectrum is computed directly from complex samples. The signal arriving at the antenna from a certain altitude does not represent the point values of plasma parameters at that altitude; rather, it is a sum of signals from different ranges and times. The signal is also deformed by the receiver-impulse response which is equivalent to calculating a weighted average over time as determined by the impulse response of the receiver. Therefore, the signal is a weighted sum of the signals from different ranges and lags. The functions describing the weights in the sum are known as ambiguity functions. The theory of two dimensional ambiguity functions is discussed in detail by Lehtinen (1986) and Nygren (1996).

For the PFISR long-pulse mode, a pulse width of 480  $\mu\text{s}$  is used and is sampled every 30  $\mu\text{s}$  at the receiver. Figure 2.9 shows the two-dimensional ambiguity function, including the filter effects. It can be clearly observed that the zero-lag contains data from a broad altitude range that is equivalent to the pulse-width, whereas longer lags contain data from a narrower altitude range. Shorter lags are more heavily weighted in the autocorrelation function than the longer lags. Therefore, different lags have different range ambiguity functions, which have to be taken into account while calculating the autocorrelation. The correlator collects the data from the A/D

converter and calculates the lagged products and integrates them for a specified number of transmissions. Averaged lagged products are organized into a matrix called a lag profile matrix. In order to increase the accuracy of the autocorrelation function, two or more neighboring elements from a lag profile are added to make a single-lag estimate by a method called gating. Gating of lagged products reduces the statistical error of the measurement along with the range resolution. Various summation rules like the triangular-summation rule, the alternate-triangle-summation rule and the trapezoidal-summation rule are used to estimate ACFs from lag-profile matrices. Summation rules and various other alternate ways to estimate ACFs are discussed in detail by Holt et al., (1992).

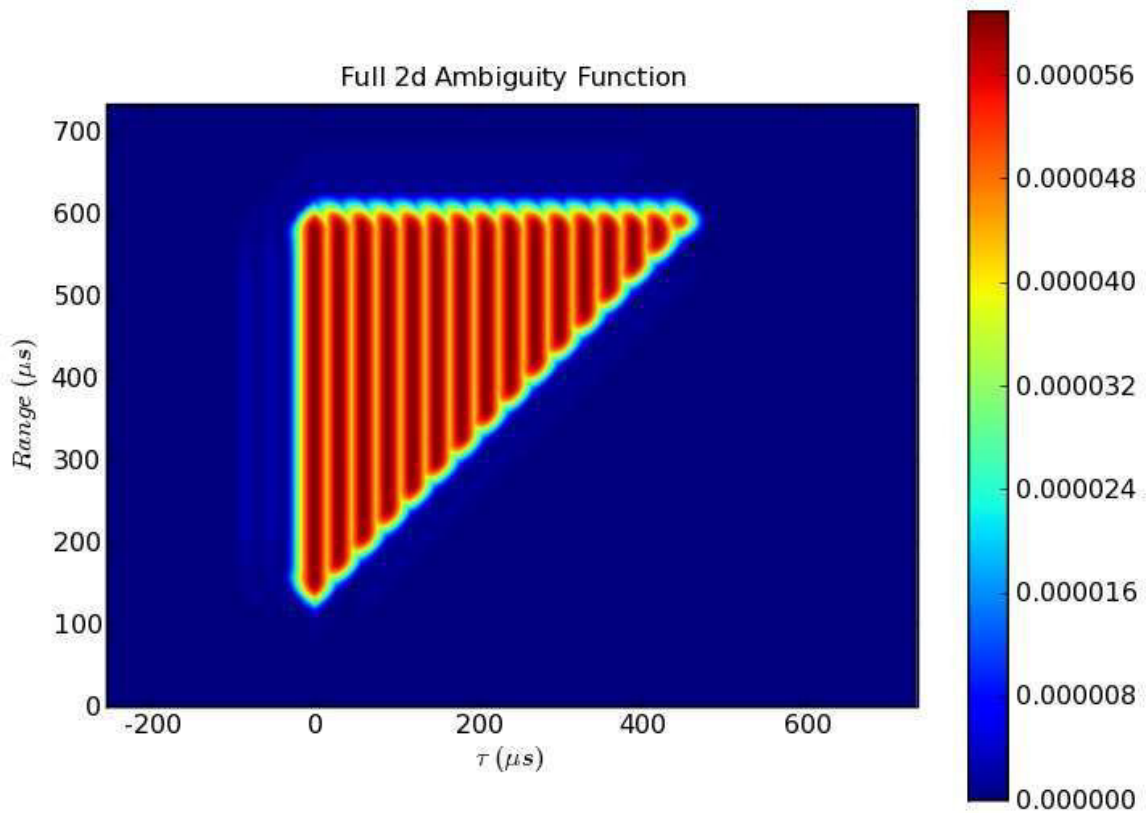


**Figure 2.9:** Two dimensional ambiguity function of a long-pulse with a pulse width of  $480 \mu\text{s}$  sampled at rate of  $30 \mu\text{s}$  including filter effects.

Once the ACFs are estimated for various range separations and lags, various plasma parameters can be estimated by using either power spectrum or the autocorrelation function. Incoherent scatter data analysis is an inverse problem where the parameters are predicted from the model and the data. The measured spectrum is noisy and the data is fitted to the model by using different fitting algorithms. Figure 2.10 shows the measured autocorrelation function and

power spectrum along with the fitted data at various ranges along the direction of the magnetic field line for PFISR.

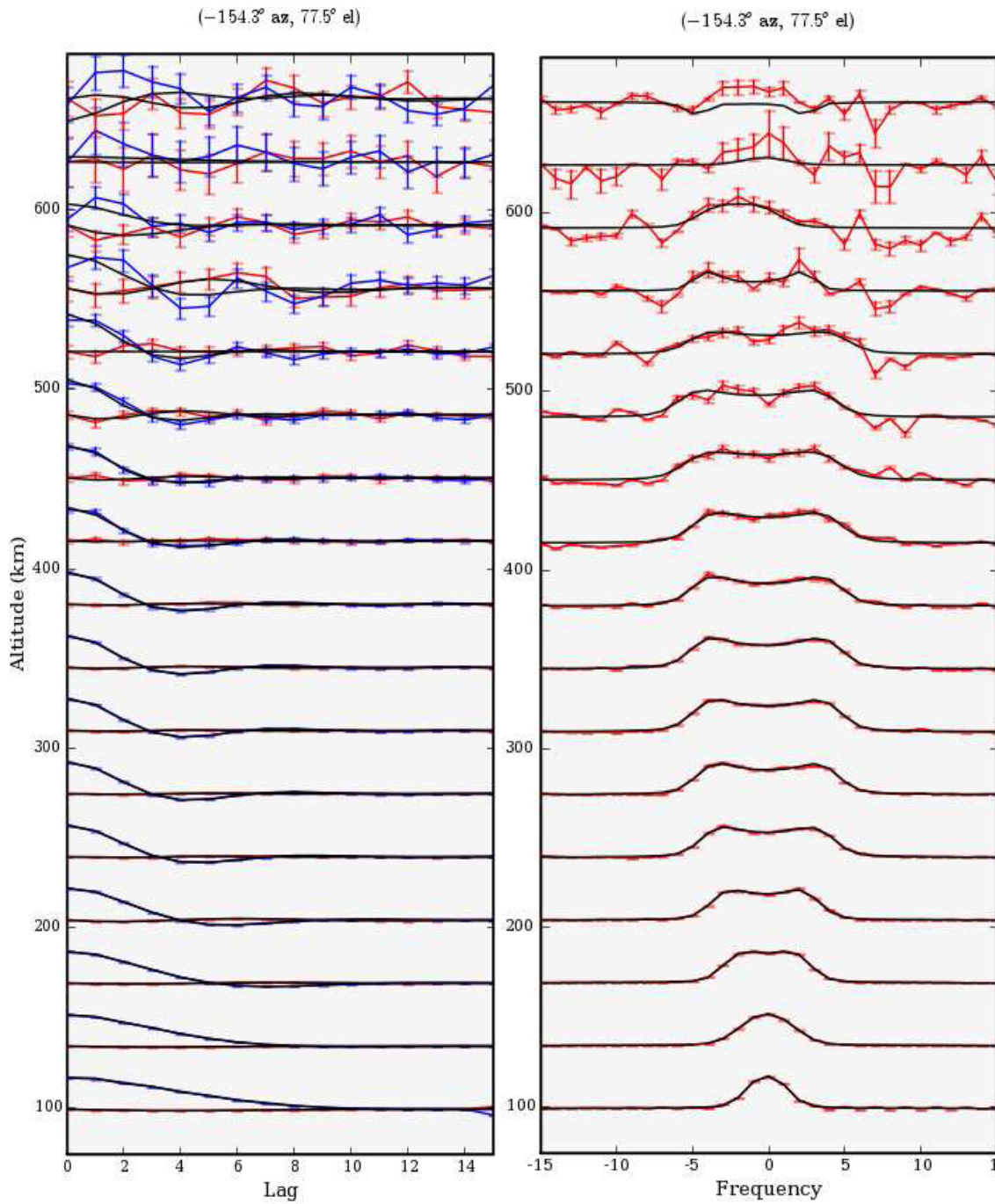


**Figure 2.10:** Measured autocorrelation function and power spectrum as a function of altitude along with fitted data for the beam direction along the field line using long-pulse data [Courtesy of M.J. Nicolls].



## 2.4. Determination of Ion Vector Velocities

The full velocity field (i.e. the three orthogonal components of plasma velocity vector) required to give a complete description of ion motion is derived using the line-of-sight ion velocities. Earlier, measurements of the drift velocity component approximately along the direction of the magnetic field line from Saint Santin, France were first reported by Carru et al., (1967a, 1967b) and Vasseur (1969). Measurements of vertical drift velocity were also found by using Jicamarca radar [Woodman and Hagfors, 1969] and Millstone Hill radar [Evans et al., 1970]. In order to estimate three independent components (North-South, East-West and Parallel components) of plasma velocity, the radar has to measure the line-of-sight velocity from three different beams pointing simultaneously at the same volume. A new radar system with three stations (one station capable of acting as both transmitter and receiver and the other two stations acting as receivers) arranged approximately at the corners of an isosceles triangle directed at the same volume for measuring plasma vector velocities was proposed by Evans (1972). Multistatic radar with a transmitter at Malvern and three receiving stations at Aberystwyth, Wardle and Chilbolton was used to measure three-dimensional plasma velocities [Taylor, 1974].

The EISCAT (European Incoherent Scatter Scientific Association) UHF system with three incoherent scatter radar stations at Tromsø (Norway), Sodankylä (Finland) and Kiruna (Sweden) can be operated either in monostatic mode or multistatic mode to estimate plasma velocities [Williams et al., 1984; Schlegel and Moorcroft, 1989]. A monostatic instrument with fully steerable antenna can also be used to determine plasma velocities. In the case of monostatic radar, line-of-sight velocities are measured from three or more different directions by steering the radar mechanically in different azimuths and elevations. This method is employed at Arecibo [Behnke, 1971; Harper, 1971; Hagfors and Behnke, 1974; Sulzer et al., 2005], Millstone Hill [Evans, 1972; Wand and Evans, 1981] and Chatanika incoherent scatter radars [Doupnik et al., 1972; de la Beaujardiére et al., 1977].

With the 23-cm wavelength incoherent scatter facility at Chatanika (Alaska), Doupnik et al. (1972) were able to measure vector velocities with a time resolution of 30 minutes and with a spatial resolution of 57 km by steering the antenna in three different azimuths spaced at  $120^\circ$  apart. Assuming plane-earth geometry, Hagfors and Behnke (1974) were able to provide the velocity information with a time resolution of 20 min and with a spatial resolution of 120 km. Plasma velocity was measured with a resolution of 10-30 min's assuming that the velocity was

constant over periods of tens of minutes and over a distance of hundreds of kilometers. This method of resolving three components of ionospheric vector velocities with a time resolution of 10-30 min and a range resolution of 50-150 km from the line-of-sight velocities measured at different scattering volumes and at different times with an inherent assumption of time and spatial stationarity over the scan is apt for low and middle latitude regions where ionospheric conditions are quiet. This method is not always adequate at high-latitude regions because of rapid changes in plasma velocity at the Harang discontinuity and at times of auroral substorms. Another drawback of the scanning systems is that they produce inconsistent velocity estimates when the velocity changes rapidly during the period of scan [Heinselman and Nicolls, 2008]. Mechanically-scanning systems are very slow and beam-positioning patterns are limited by antenna inertia and the inflexibility of the radar which reduces the time and spatial resolution of radar.

The Advanced Modular Incoherent Scatter Radar (AMISR) is a new ISR that employs phased-array technology capable of measuring plasma parameters near simultaneously in multiple beam directions. Phased-array radar systems utilize an array of radiating elements which are fed with a radio frequency source through a phase-shifting network. Beams can be formed in any desired angle by controlling the phase of the signal fed to antenna element units. The phase of the radiating elements is controlled electronically and thus the beams can be steered without moving the radar mechanically. Phased-array technology provides the ability to change the beam direction with high directivity almost instantaneously and overcomes all the disadvantages of mechanical systems.

An approach for estimating the vector velocities in the F region was reported by Heinselman and Nicolls (2008). By steering the beam on a pulse-to-pulse basis in multiple (at least three) beam directions and on integrating the received pulses over a period of time, various plasma parameters along with line-of-sight velocities are effectively measured simultaneously. Line of sight (LOS) velocities are resolved into vector drifts with an assumption of constant velocity over an integration period rather than the duration of the scan which is a major advantage over traditional ISRs. Heinselman and Nicolls (2008) estimated the LOS velocities from a fit to full incoherent- scatter autocorrelation function (using both real and imaginary parts). However, LOS velocities can also be measured by fitting a measured spectrum to the

theoretical spectrum or a fit to the phase angle. In the local geomagnetic coordinate system, any LOS velocity measurement  $i$  from any beam direction can be represented as

$$v_{los}^i = k_{pe}^i v_{pe} + k_{pn}^i v_{pn} + k_{ap}^i v_{ap} = \mathbf{k} \mathbf{V}$$

where  $\mathbf{V} = [v_{pe} \ v_{pn} \ v_{ap}]^T$  is an unknown ion velocity vector with three components defined in a local geomagnetic coordinate system, the subscripts  $pe, pn$  refer to field-perpendicular east and north components respectively and  $ap$  refer to field-parallel component.

Projection matrix  $\mathbf{k} = [k_{pe} \ k_{pn} \ k_{ap}]$  is given by

$$\mathbf{k} = \begin{bmatrix} k_{pe} \\ k_{pn} \\ k_{pz} \end{bmatrix}^T = \begin{bmatrix} k_e \cos \delta - k_n \sin \delta \\ k_z \cos I + \sin I (k_n \cos \delta + k_e \sin \delta) \\ k_z \sin I - \cos I (k_n \cos \delta + k_e \sin \delta) \end{bmatrix}^T = [\mathbf{k}' * R_{geo \rightarrow gmag}]^T.$$

The radar centered vector  $\mathbf{k}'$  in the geographic coordinate system is defined as

$$\mathbf{k}' = \begin{bmatrix} k_e \\ k_n \\ k_z \end{bmatrix} = \begin{bmatrix} \cos \theta \sin \emptyset \\ \cos \theta \cos \emptyset \\ \sin \theta \end{bmatrix}$$

where the subscripts  $e, n, z$  refer to East, North and Up respectively and  $\emptyset, \theta$  refer to the azimuth and elevation angle of the radar beam direction, respectively. Rotation matrix  $R_{geo \rightarrow gmag}$  used for transforming of the velocity vector from the geographic coordinate system to the local geomagnetic coordinate system can be written as

$$R_{geo \rightarrow gmag} = \begin{bmatrix} \cos \delta & -\sin \delta & 0 \\ \sin I \sin \delta & \cos \delta \sin I & \cos I \\ -\cos I \sin \delta & -\cos I \cos \delta & \sin I \end{bmatrix}$$

where  $\delta (\sim 22^\circ)$  and  $I (\sim 77.5^\circ)$  corresponds to the declination angle and dip (or inclination) angle respectively.

Heinselman and Nicolls (2008) used a Bayesian linear model to combine all samples within a particular magnetic-latitude bin to produce a single estimate with a full error covariance estimate. The Bayesian linear model for a particular measurement is the dot product of the projection matrix  $\mathbf{K}^i$  with a velocity vector  $\mathbf{v}_i$  plus an error associated with LOS velocity estimate and can be written as

$$v_{los}^i = \mathbf{K}^i \cdot \mathbf{v}_i + e_{los}^i.$$

Multiple measurements can be written as

$$\begin{bmatrix} v_{los}^1 \\ v_{los}^2 \\ \cdot \\ \cdot \\ v_{los}^k \\ \cdot \\ \cdot \\ v_{los}^n \end{bmatrix} = \begin{bmatrix} k_{pe}^1 & k_{pn}^1 & k_{ap}^1 \\ k_{pe}^2 & k_{pn}^2 & k_{ap}^2 \\ k_{pe}^3 & k_{pn}^3 & k_{ap}^3 \\ \cdot & \cdot & \cdot \\ \cdot & \cdot & \cdot \\ k_{pe}^k & k_{pn}^k & k_{ap}^k \\ \cdot & \cdot & \cdot \\ \cdot & \cdot & \cdot \\ k_{pe}^n & k_{pn}^n & k_{ap}^n \end{bmatrix} \begin{bmatrix} v_{pe} \\ v_{pn} \\ v_{ap} \end{bmatrix} + \begin{bmatrix} e_{los}^1 \\ e_{los}^2 \\ e_{los}^3 \\ \cdot \\ \cdot \\ e_{los}^k \\ \cdot \\ \cdot \\ e_{los}^n \end{bmatrix}$$

(Or)

$$\mathbf{V}_{los} = \mathbf{A}\mathbf{v}_i + \mathbf{e}_{los}.$$

In order to estimate the velocity vector  $\mathbf{v}_i$  as a function of latitude, the above equation can be solved using a Bayesian estimator [Heinselman and Nicolls, 2008], which can be written as

$$\hat{\mathbf{v}}_i = \Sigma_v \mathbf{A}^T (\mathbf{A} \Sigma_v \mathbf{A}^T + \Sigma_e)^{-1} \mathbf{v}_{los}$$

where  $\mathbf{v}_i$  is a Gaussian-random variable with zero mean and with a covariance of  $\Sigma_v$ ,  $\Sigma_v$  is a prescribed prior covariance model for  $\mathbf{v}$ ,  $\Sigma_e$  is an error covariance matrix.

A 13-antenna beam-position mode is a common experimental configuration employed for electric field measurements using PFISR. Figure 2.11 shows the geometry plot of the elevation

and azimuth angle of the beams and the line plot of the range coverage (typically 0-800 km, which varies depending upon the elevation angle of the beam) of beam directions as a function of magnetic-latitude and magnetic-longitude [Nicolls and Heinselman, 2007]. Among the 13 beams, one beam (# 12) is pointed along the magnetic field aligned direction of PFISR ( $Az = -154.3^{\circ}$  and  $El = 77.5^{\circ}$ ), four beams (#9-11,13) are pointed along the poleward (i.e., directly towards north), four beams (#1-4) are pointed along the westward (i.e., towards northwest) and the remaining four beams (#5-8) are pointed along the eastward (i.e., towards northeast). The transmission scheme consists of a long pulse (a pulse width of  $480 \mu s$  corresponding to a range resolution of 72 km is sampled at receiver at a rate of  $30 \mu s$ ) and an alternating code (with a range resolution of 4.5 km). This beam configuration provides the data with the largest magnetic latitude coverage and good temporal resolution. This beam configuration is best-suited for determining the F-region plasma drift velocity components and also for E- region measurements. The measured LOS velocities are integrated over a period of time, typically 1-3 min, and have a range resolution of 36 km (range resolution corresponding to half of a pulse width of a long-pulse). Figure 2.12 and 2.13 shows LOS velocities and densities for a typical experiment from 13 beam directions as a function of altitude with a time resolution of 1 min and a spatial resolution of 36 km measured using a long-pulse. Each panel on these figures corresponds to separate antenna pointing directions. Figure 2.14 shows the resolved velocities as a function of time and magnetic latitude with a time resolution of 1 min and a spatial resolution of  $0.25^{\circ}$  latitude.

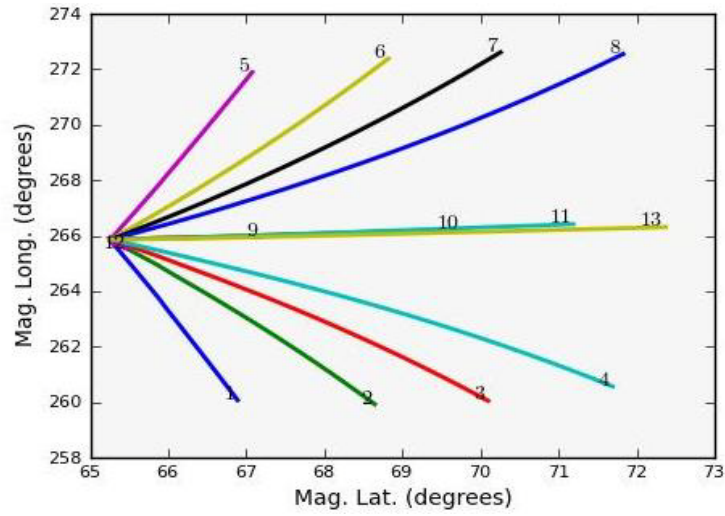
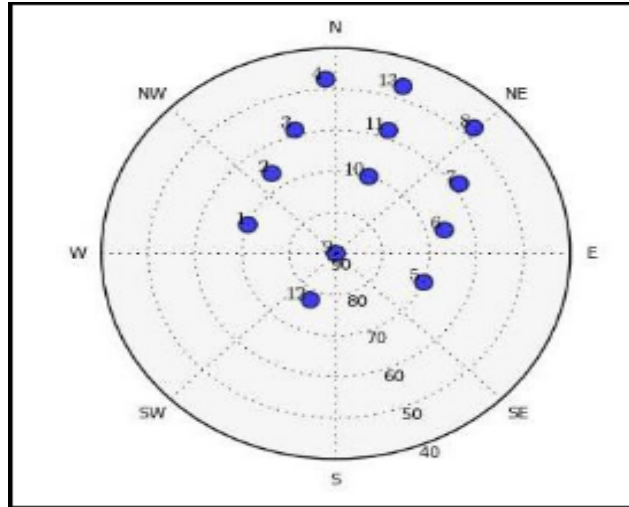


**Figure 2.11:** Experimental configuration for THEMIS 13 beam position mode. The top panel shows the azimuth and elevation for all the beam directions and the bottom panel shows the geomagnetic latitude and longitude coverage of the beams.

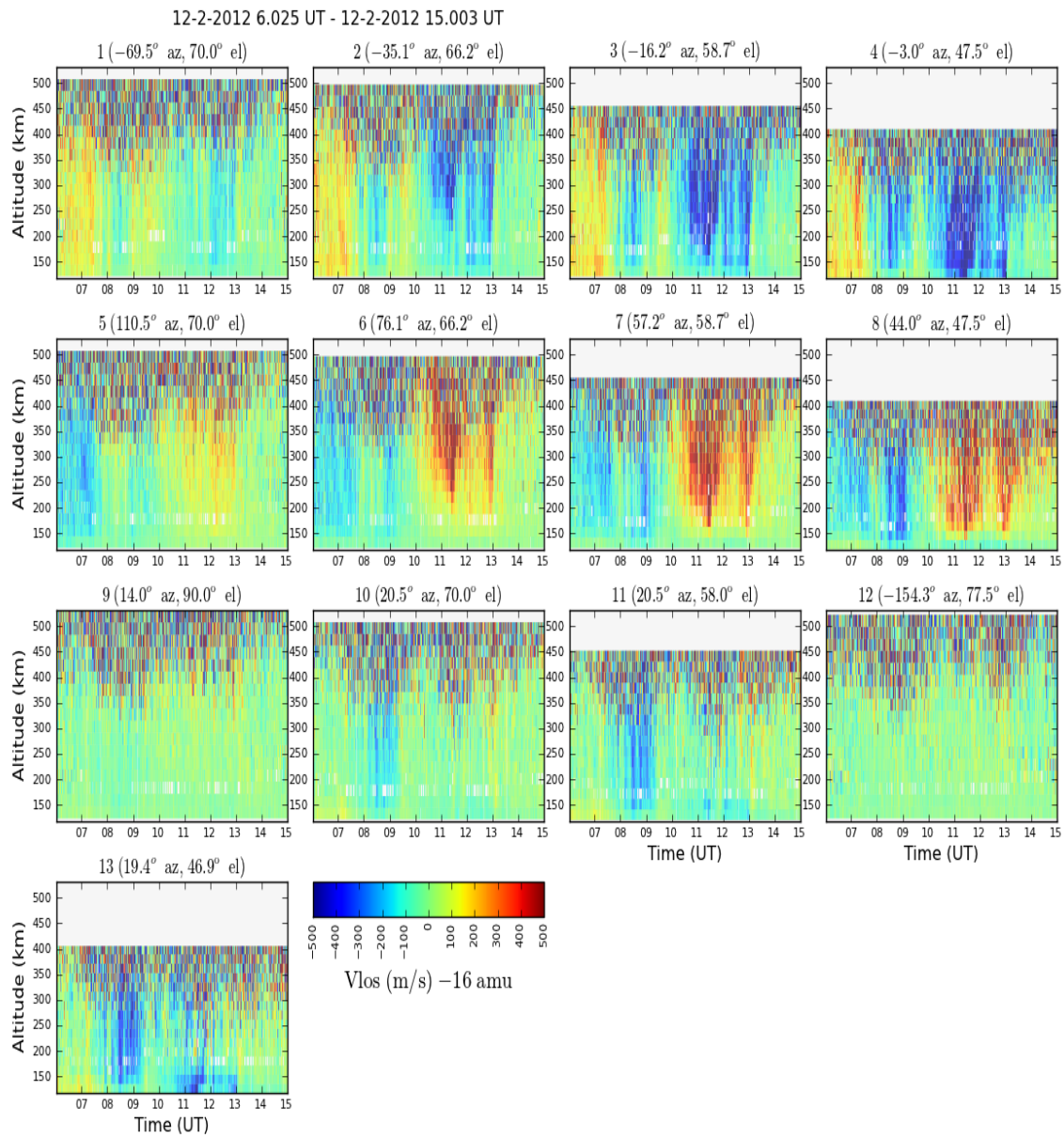


**Figure 2.12:** Line-of-sight ion velocities as a function of time and altitude for 13 beam positions from the long-pulse measurements on 02 December 2012.

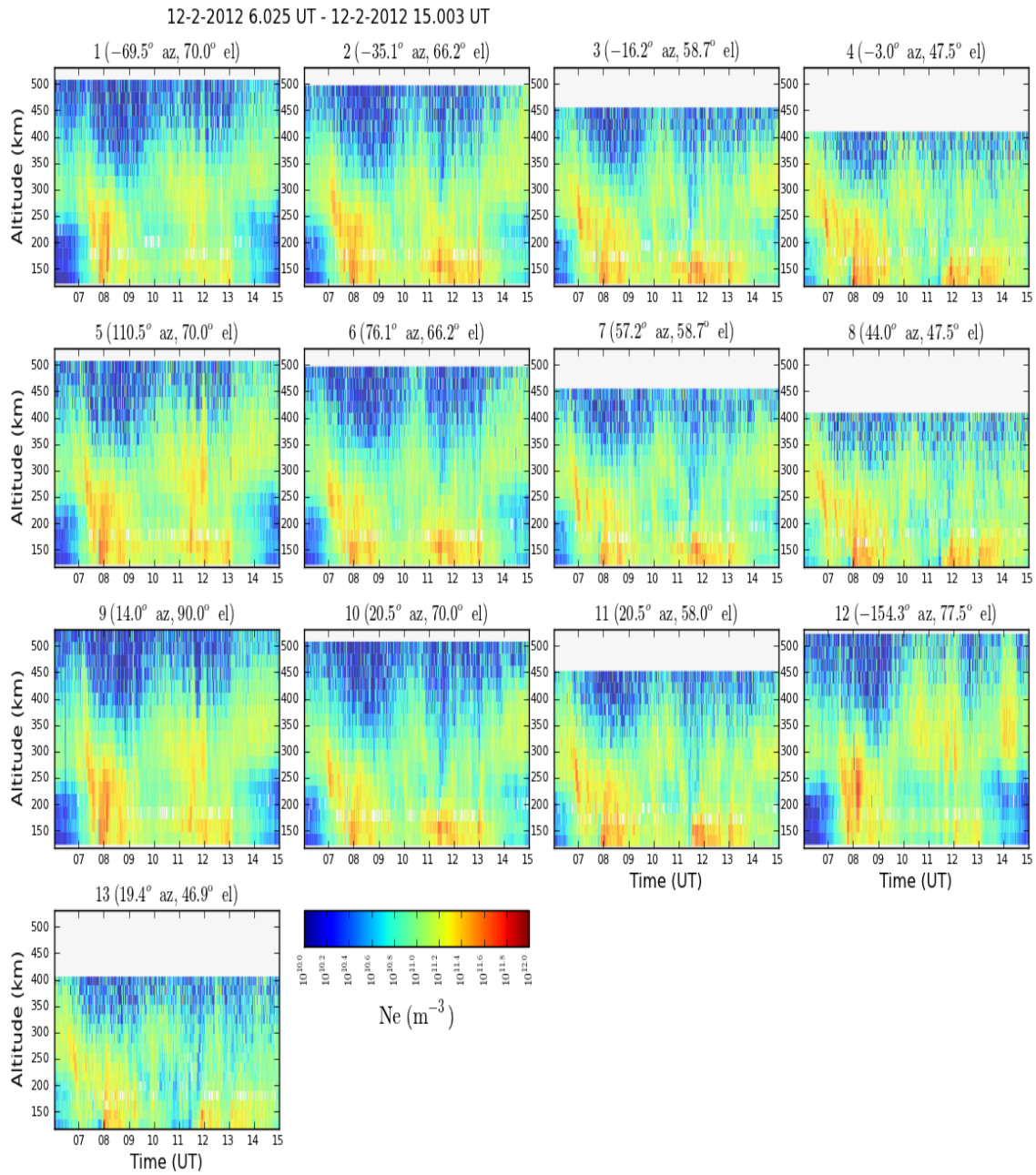


**Figure 2.13:** Electron density (with temperature corrections) as a function of time and altitude for 13 beam positions from the long-pulse measurements on 02 December 2012.



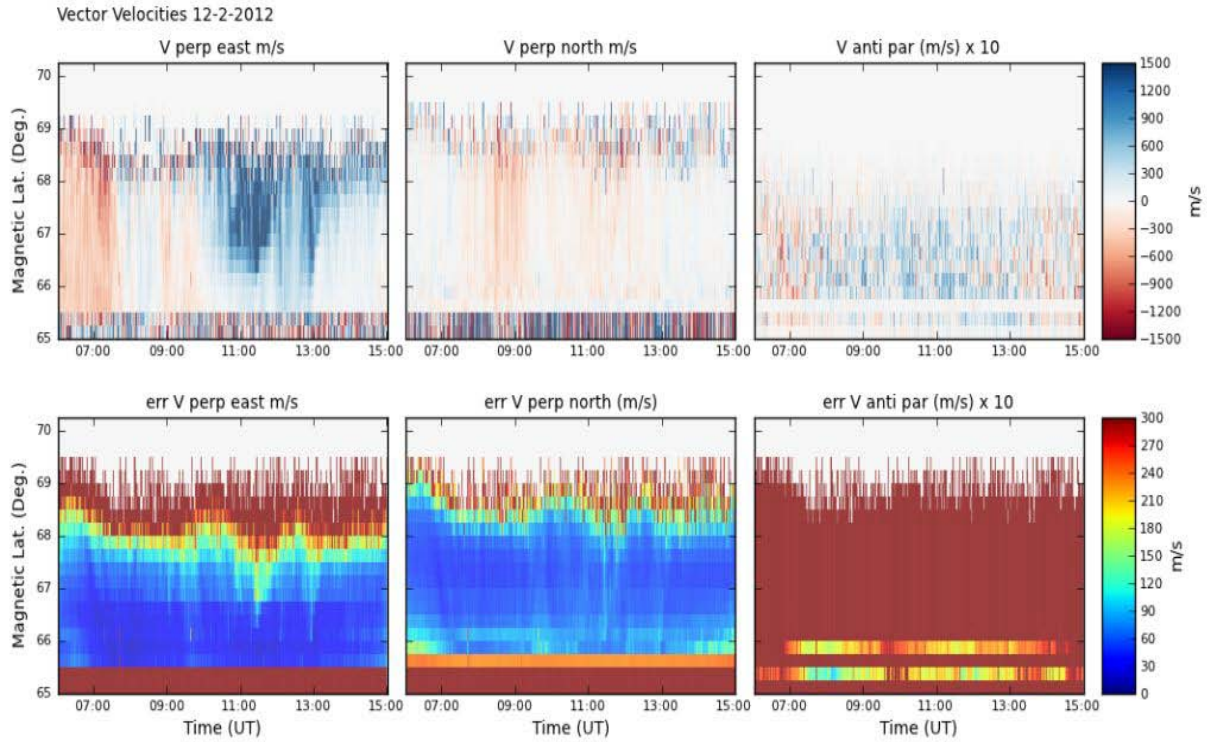


**Figure 2.14:** Perpendicular east, perpendicular north and anti-parallel velocities along with error estimates as function of magnetic latitude and time from the long-pulse measurements on 02 December 2012.

## **CHAPTER 3. EXPERIMENTAL APPROACH**

### **3.1. Introduction**

In the previous chapter the incoherent-scatter radar theory as well as the determination of electron density, and determination of ion velocity using the Advanced Modular Incoherent Scatter Radar at Poker Flat, Alaska was discussed. In this chapter the experimental approach and the technique used to measure the scale sizes of large-scale electron density irregularity structures is presented. This will be done by using Doppler measurements of the horizontal plasma velocity in conjunction with high time resolution measurements of the scattered power.

SRI International, under a grant from the National Science foundation, developed AMISR with electronic beam steering and remote operation capabilities to study the upper atmosphere. AMISR consists of two separate radars [Poker Flat, Alaska (PFISR) and Resolute Bay, Canada (RISR-N and RISR-C)], with each face comprised of 128 panels over a 30 x 30 meter roughly square surface.

### **3.2. AMISR System Description**

A standard AMISR system consists of 128 AMISR panels with 4096 Transmit/Receive modules known as Antenna Element Units (AEUs). Each AEU consists of a 500 W solid state power amplifier (SSPA) to generate the transmitted RF signal, a crossed dipole antenna to convert the electric signals to circularly polarized radio waves, low level RF circuitry for phase control on transmit and receive, a low noise amplifier to amplify the signals captured by the antenna, a power supply, and digital control and communications electronics. Each AMISR panel consists of 32 AEUs controlled and monitored by a Panel Control Unit (PCU) which includes a programmable Linux based computer. The radar runs on a 400 Hz power which is generated by eight JetPower units in two Utility Distribution Unit (UDU) vans. The complete radar system is controlled from Operation and Control Center (OCC) which houses the data acquisition channels, general purpose computers and the source for the transmitted signal. The AMISR system can be operated over the internet without an onsite operator. Figure 3.1 shows the building blocks of an AMISR system.

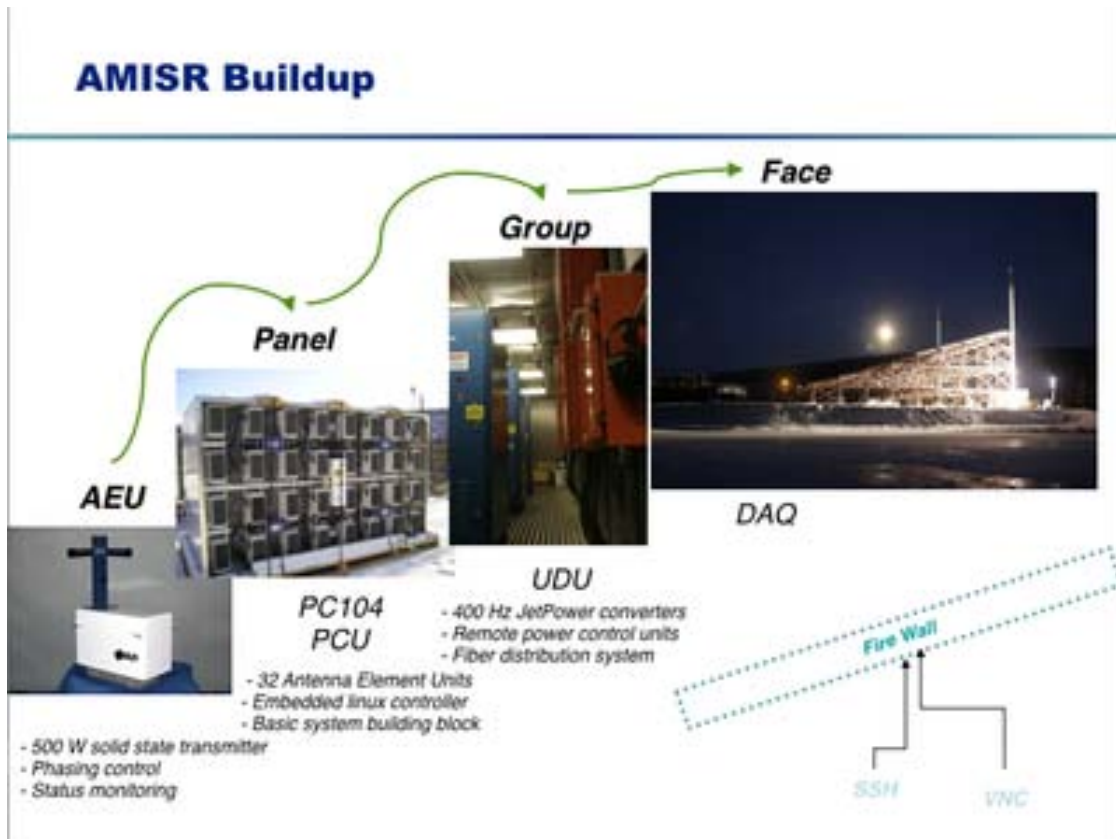


**Figure 3.1:** Building blocks of an AMISR system.

### 3.3. Description of Experiments

The experiments were carried out using the Poker Flat Incoherent Scatter Radar (PFISR), located at Poker Flat Research Range near Fairbanks, Alaska, which has a geographic latitude  $65.199^{\circ}\text{N}$  and longitude  $147.47^{\circ}\text{W}$ . Figure 3.2 shows the northward- looking Ultra High Frequency (UHF) phased array radar at Poker Flat. The face of the radar is tilted along the direction of magnetic meridian in such a way that its bore sight direction corresponds to an azimuth angle (east of north) of  $15^{\circ}$  and an elevation angle of  $74^{\circ}$ . This organization allows the radar to look up along the local magnetic field line as well as maximum possible downrange coverage to support rocket observations at Poker Flat Research Range. The radar operating frequency is approximately 450 MHz and operates at an output power of 2 MW with 10% maximum duty cycle. A recent upgrade of the number of panels from 96 to 128 increased the antenna aperture to approximately  $715\text{ m}^2$  as well as the transmitted power which increased the SNR of the radar by approximately 80%. The beam width of the radar is about  $1^{\circ} \times 1.15^{\circ}$  and the magnetic dip angle varies from  $75^{\circ}$  to  $85^{\circ}$  in the F region, depending on the beam position.

PFISR can be pointed in any of the 473 preprogrammed look directions within the grating lobe limits. These beam configuration positions along with the grating lobe limits are shown in figure 3.3a. The system gain is 43 dBi at the bore sight and it decreases proportionally to the cosine of the angle off bore sight. PFISR's field of view at various altitudes is shown in figure 3.3b. High-time resolution measurements can be taken in multiple beam directions by electronically steering the beam on a pulse-to-pulse basis by using the phased array technique. As the look directions increases time resolution decreases and vice versa.



**Figure 3.2:** Northward looking UHF phased array radar at Poker Flat, near Fairbanks, Alaska.

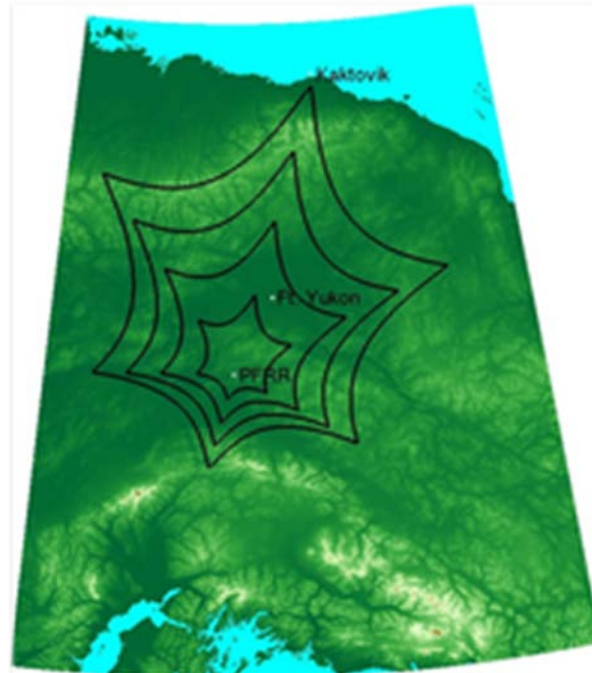
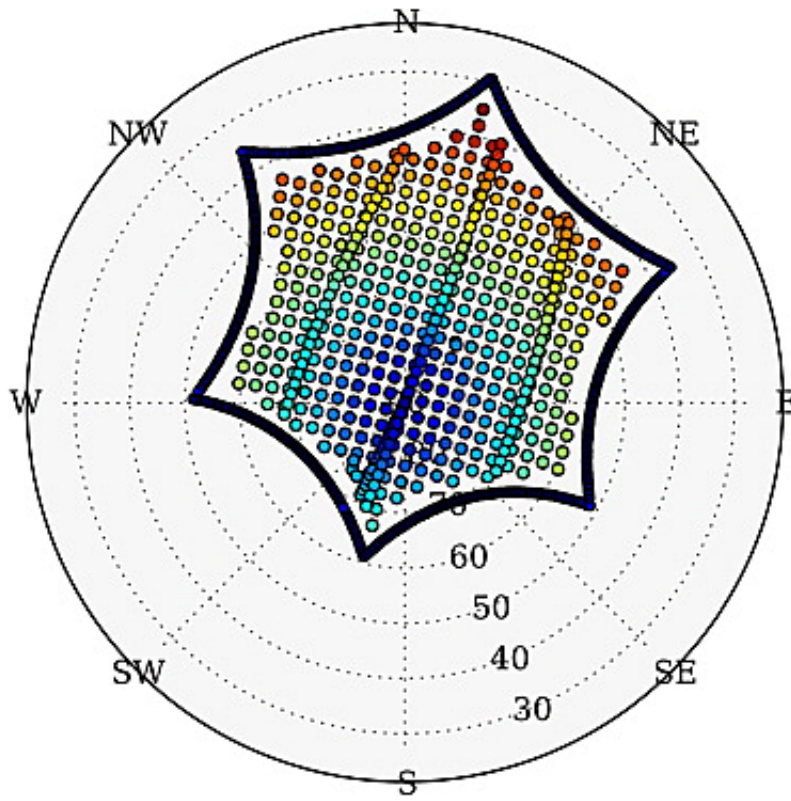


**Figure 3.3:** (a) Possible PFISR beam directions with black star shaped grating lobe limits of the system. (b) Contours represent the PFISR's field of view at 100, 200, 300 and 400 km altitude.

The first experiments were run in August of 2011 for a period of three hours around local midnight from 9-12 UT. In order to achieve high-time resolution measurements of electron density and ion velocity, the Poker Flat Incoherent Scatter Radar (PFISR) was set to run a mode consisting of four antenna beams (one vertical, one along the local magnetic field line i.e. towards north, and the other two beams were spread towards northeast and northwest) transmitting long pulses (480  $\mu$ s corresponding to range resolution of 72 km) on two frequencies (449.6 MHz and 449.3 MHz) with a total output power of 1.72 MW. The return samples were collected every 30  $\mu$ s (corresponding to a range resolution of 4.5 km) from an altitude of 100 to 743 km. Samples of noise were taken at a far range when there are no return signals from the ionosphere, and samples from the injected calibrated pulse of known temperature were also measured. For the mode used here, the four antenna azimuth positions were 14.04°, -154.3°, 15°, 103.29° with elevation angles of 90°, 77.5°, 74°, 74.99° respectively. Figure 3.4 shows the geometry plot of the azimuthal and elevation angle of the beams. This mode transmits ~36 long pulses per second in the vertical direction and 12 pulses per second in each of 3 other look directions. The vertical beam has higher time resolution than the other beams since every other pulse is transmitted in the vertical direction and is used to observe the electron density irregularities whereas the other beams were used to obtain the ion velocity information. The raw electron density data from the vertical beam has an average time resolution of 25 ms. In signal processing, multiple samples are integrated over a few seconds to get an integrated sample with a higher SNR than the individual samples. For this purpose the samples were integrated over ~ 3 seconds (about 120 pulses in the case of a vertical beam), through which the raw electron density is calculated by using the equation

$$Ne'(r) = \frac{2C_s}{P_T \tau_p} r^2 \frac{K_B T_{cal} B}{\overline{S_c} - \overline{S_n}} (\overline{S_r}(r) - \overline{S_n})$$

where  $\overline{S_r}$  = Time averaged measured power at a range  $r$

$K_B$  = Boltzmann constant =  $1.38 * 10^{-23}$  J/K

$T_{cal}$  = Noise pulse temperature injected by the calibrated pulse = 364 K

$B$  = Receiver bandwidth

$\overline{S_c}$  = Time averaged calibrated power

$\overline{S_n}$  = Time averaged Noise Power

$P_T$  = Peak Transmitted Power = 1.72 MW

$\tau_p$  = Pulse width = 480  $\mu$ s

$c_s$  = Calibration constant =  $1.668011e^{-19}$ .

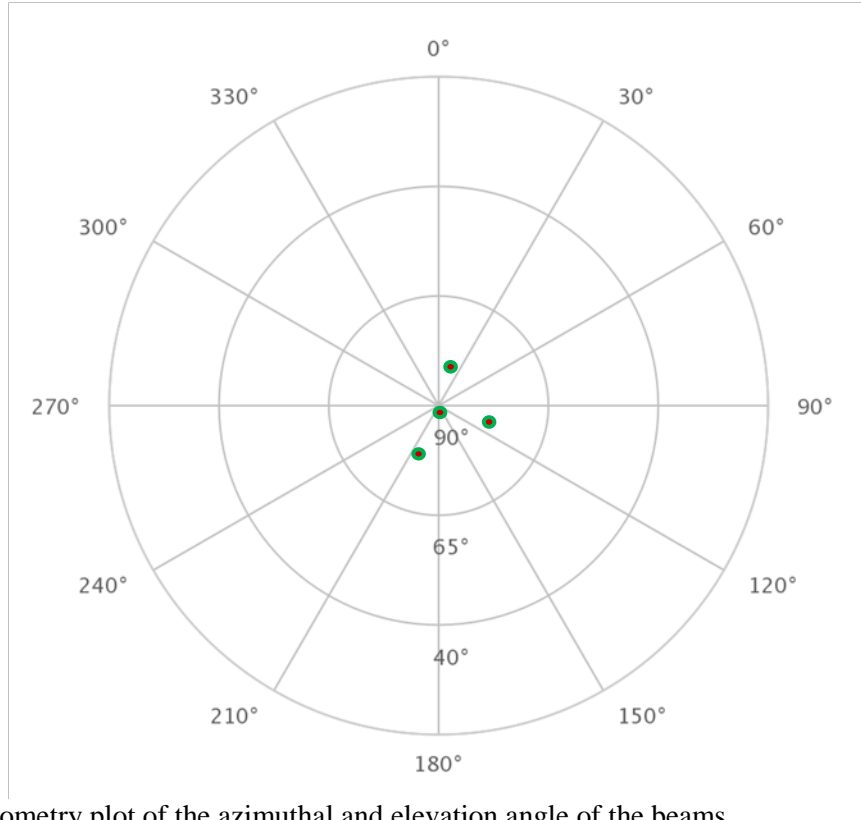


**Figure 3.4:** Geometry plot of the azimuthal and elevation angle of the beams.

Figure 3.5 shows the electron density plot as a function of time and altitude with no Te/Ti correction with an integration of 120 pulses (about 2 to 3 seconds). From the plot, it is clearly visible that there are density structures embedded in a noisy background. The little noise-like blips in the raw electron density plots are not significant enough to be treated as electron density structures as they are not spatially correlated. ISR signals themselves are noise-like as the phase information of the data is discarded by taking the magnitude of the data during the integration of pulses. Noise can be reduced by increasing the integration time from 2-3 seconds to 120-180 seconds, but this is not desired here as it filters out the electron density structures associated with 10-75 km scale sizes.

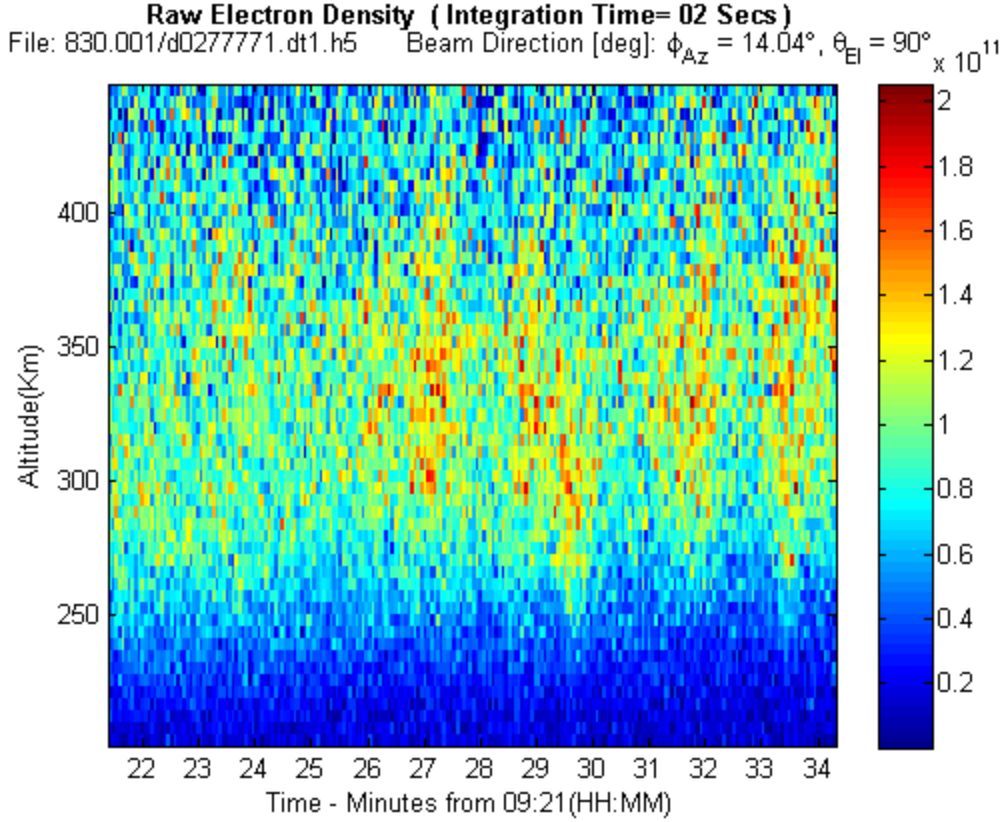


**Figure 3.5:** Electron density plot (Integration time of 2 seconds) from an altitude of 200-450 km with no Te/Ti correction as a function of altitude and time from the vertical beam [AZ:  $14.04^\circ$ , El:  $90^\circ$ ] of PFISR.

Without losing the important information in the data, noise or random fluctuations can be reduced by smoothing the data either by means of parametric regression or non-parametric regression. A prior knowledge of the regression equation that can fit the data well is required for the parametric regression analysis. Since the electron density observations cannot be parameterized in terms of a predetermined model, non-parametric regression is used to smooth the data. The most commonly used approaches for smoothing the data are running mean or moving average filter, stretched grid method, kernel smoother, Savitzky-Golay smoothing filter, local regression also known as ‘loess’ and ‘lowess’, Kolmogorov–Zurbenko filter, Natural Splines, Restricted Splines and B-Spline. Another classical approach to the problem introduced by Whittaker [1923] that has been used in this thesis is penalized least squares regression which estimates its parameters by minimizing the residual sum of squares (RSS) plus roughness penalty term (P) which is given by

$$F(\hat{y}) = RSS + s P(\hat{y}) = \|\hat{y} - y\|^2 + s \|D\hat{y}\|^2$$



where  $y$  = signal  $y$  with Gaussian noise ( $\varepsilon$ ) with zero mean and unknown variance.

$$= \hat{y} + \varepsilon$$

$\hat{y}$  = smoothed signal

$s$  = smoothing parameter

$RSS$  = residual sum of squares

$P$  = penalty term that reflects the roughness of the smooth data

$\| \cdot \|$  = Euclidean norm

$D$  = dividend difference matrix.

For one-dimensional data array  $D$  is defined by

$$D_{i,i-1} = \frac{2}{h_{i-1}(h_{i-1}+h_i)} \quad D_{i,i} = \frac{-2}{h_{i-1}h_i} \quad D_{i-1,i} = \frac{2}{h_i(h_{i-1}+h_i)} \quad \text{for } 2 < i < n - 1$$

where  $n$  = number of elements in  $\hat{y}$

$h_i$  = step between  $\hat{y}_i$  and  $\hat{y}_{i+1}$ .

Assuming the repeating border elements ( $y_0 = y_1$  and  $y_{n+1} = y_n$ ) gives

$$-D_{1,1} = D_{1,2} = \frac{1}{h_1^2} \quad \text{and} \quad D_{n,n-1} = -D_{n,n} = \frac{1}{h_{n-1}^2}.$$

Minimizing  $F(\hat{y})$  provides the smoothed data which is in the form of a linear system influenced by smoothing parameter  $s$  as given by

$$\hat{y} = \frac{1}{(I_n + sD^T D)} y = H(s)y \tag{3.1}$$

where  $H$  = hot matrix =  $(I_n + sD^T D)^{-1}$

$I_n$  =  $n \times n$  identity matrix.

A smoothing parameter should be chosen carefully in order to determine the best possible fit of the data without over- or under-smoothing the data. In the case of smoothing splines, Craven and Wahba [1978] introduced a method of generalized cross-validation (GCV) to

estimate the value of smoothing parameter  $s$ . Parameter  $s$  is chosen in such a way that it minimizes the GCV score,

$$s = \operatorname{argmin}(GCV) \text{ with } GCV(s) \equiv \frac{\frac{RSS}{n}}{\left(1 - \frac{\operatorname{Tr}(H)}{n}\right)^2}$$

where  $\operatorname{Tr}$  = trace matrix and  $\operatorname{Tr}(H)$  can be calculated by using the equation below

$$\operatorname{Tr}(H) = \sum_{i=1}^n \frac{1}{1+s\lambda_i^2},$$

when  $\lambda_i^2$  = eigenvalues of  $D^T D$ .

Substituting  $\operatorname{Tr}(H)$  in the above equations we get

$$GCV(s) = n \sum_{i=1}^n (\hat{y}_i - y_i)^2 / (n - \sum_{i=1}^n (1 + s\lambda_i^2)^{-1})^2.$$

During the minimization process of GCV score  $\hat{y}$  is calculated at each step since the GCV score is a function of  $\hat{y}$  increasing the computational complexity. As the amount of data increases solving eq 3.1, which is a linear system, is time consuming. Buckley [1994] introduced an algorithm based on discrete cosine transform that can reduce the computational complexity and time when the data is equally spaced or evenly gridded. For equally spaced data, matrix  $D$  can be written as simple difference matrix and Eigen decomposition of  $D$  yields

$$D = U\Lambda U^{-1}$$

where  $U$  = unitary matrix

$$\begin{aligned} \Lambda &= \text{diagonal matrix containing the Eigenvalues of } D \\ &= \operatorname{diag}(\lambda_1 \cdots \cdots \lambda_n) \text{ with } \lambda_i = -2 + 2\cos\left(\frac{(i-1)\pi}{n}\right). \end{aligned}$$

Substituting  $D$  in eq (3.1) leads to

$$\hat{y} = U(I_n + s\Lambda^2)^{-1}U^T y \equiv U\Gamma U^T y = \operatorname{IDCT}(\Gamma \operatorname{DCT}(y)) \quad (3.2)$$

where  $U^T, U = n$ -by- $n$  type-2 DCT and inverse DCT matrices

$$\Gamma_{i,i} = [1 + s(2 - 2\cos \left(\frac{(i-1)\pi}{n}\right)^2)]^{-1} \text{ for } i = j$$

$$= 0 \text{ for } i \neq j.$$

Substituting and solving the above equations provides a simplified GCV score which is given by

$$GCV(s) = \frac{n \sum_{i=1}^n \left(\frac{1}{1+s\lambda_i^2} - 1\right)^2 DCT_i^2(y)}{\left(n - \sum_{i=1}^n \frac{1}{1+s\lambda_i^2}\right)^2}.$$

The penalized least square approach based on the DCT does not require any matrix manipulations to determine a GCV score which reduces the computational complexity and time taken to smooth the data. DCT-based smoothing technique adapted to weighted data, missing values and two dimensional data was explained in detail by Garcia [2009]. Garcia also provided fully automated simplified Matlab code for smoothing of one-three dimensional data.

This smoothing technique that carries out the amount of smoothing by minimizing the GCV score is applied to the two dimensional electron density data. The filtered density is as shown in figure 3.6. From this plot, we can clearly observe some large-scale electron density irregularity structures without any uncertainties due to noise measurements. The fractional change in TEC associated with these plasma structures varies from 0.01 TECU to a few TECU depending on the ionospheric conditions. Variations of about 0.23 TECU or more is a problem for interferometer applications and are difficult to correct in SAR imaging [Meyer, 2011].

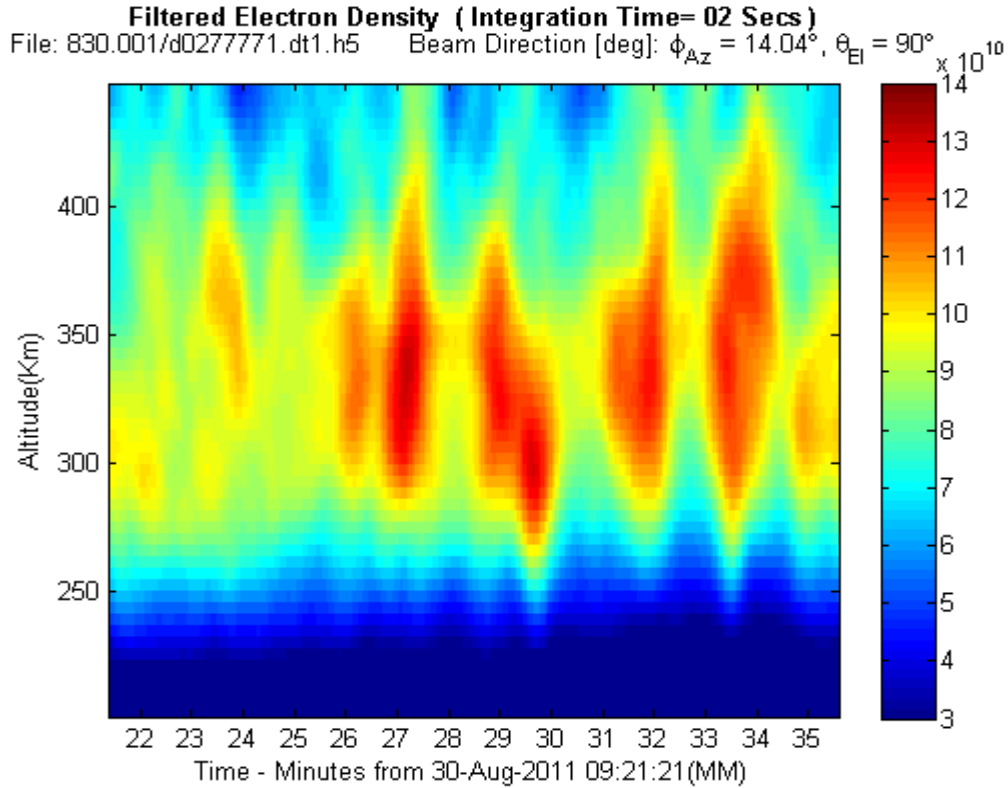


**Figure 3.6:** Filtered Electron density plot (integration time of 2 seconds) from an altitude of 200-450 km with no Te/Ti correction as a function of altitude and time from the vertical beam [ $Az: 14.04^\circ$ ,  $El: 90^\circ$ ] of PFISR.

### 3.4. Determination of Ionization Blob Scale Sizes

As the objective of the thesis is to measure the scale sizes of F-region ionosphere plasma structures, the filtered electron density data from 200-450 km is integrated across the range bins to obtain a line plot every  $\sim 12$  minutes as shown in figure 3.7. The horizontal extent of the electron density irregularity structures is equal to the wavelengths of integrated electron density time series data. In order to measure various local wavelengths on a crest-to-crest or trough-to-trough basis, velocity information with which these structures are moving and the frequency content of the time series signal is required. These structures are thought to be moving with  $E \times B$  drift velocity. Neutral winds might also play a role in the convection of blobs but as the incoherent-scatter radar measures the resultant ion velocity, this ion velocity information itself is sufficient to calculate the blob sizes.

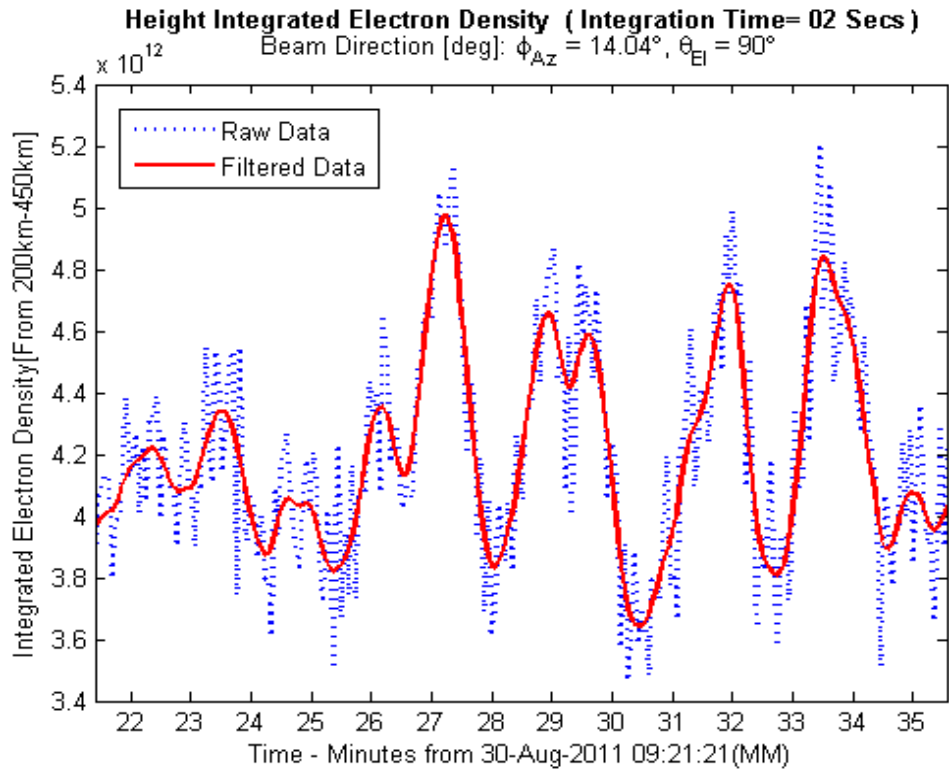


**Figure 3.7:** Height Integrated Electron density  $N_e$  (Integrated over F region i.e., from 200-250 km) with no Te/Ti correction as a function of time from the vertical beam [ $Az$ : 140.040,  $El$ : 90o] of PFISR.

Spectral density or power spectral density estimate of the time series signal characterizes the frequency content of the signal. Spectrum estimation can be done either by using parametric methods (covariance, modified covariance, Burg, and Music) or non-parametric methods (Periodogram, Correlogram, Modified periodogram, Welch's method, Blackman-Tukey, and Lomb scargle periodogram). Parametric methods are based on parametric models (auto regressive (AR) models, moving average (MA) models and auto regressive – moving average (ARMA) models). In order to estimate power spectral density (PSD) by using parametric methods in a reliable way, an appropriate model that reflects the behavior of the system that generates the time series should be estimated first. Parametric methods cannot be used here as there is no prior information of the model that can reflect the F-region ionosphere electron density data. Non-parametric methods of spectrum estimation are based on the discrete Fourier transform. The periodogram of the sequence  $y(t)$ ,  $t=1\dots N$  is modulus-squared of the Fourier transform and is given by

$$\hat{\Phi}_p(\omega) = \frac{1}{N} \left| \sum_{t=1}^N y(t) e^{-j\omega t} \right|^2 = \frac{1}{N} |y(\omega)|^2.$$

The periodogram can be rewritten as

$$\hat{\Phi}_c(\omega) = \sum_{k=-N+1}^{N-1} \hat{r}_k e^{-j\omega k}$$

where

$$\hat{r}(k) = \sum_{t=k+1}^N y(t) y^*(t-k) \quad 0 \leq k \leq N-1$$

$\hat{r}(k)$  = estimate of the covariance  $r(k)$  and  $r(k) = r(-k)$  for real valued signals.

This above form is referred to as a Correlogram. A spectral estimate is calculated by applying the Fourier transform to the autocorrelation sequence of the time series signal. Modified periodogram, Welch, and Bartlett methods are designed to reduce the variance of the basic periodogram. Statistical variability of spectrum estimation can be reduced by using a Blackman-Tukey spectral estimate and is given by

$$\hat{\Phi}_{BT}(\omega) = \sum_{k=-(M-1)}^{M-1} w(k) \hat{r}(k) e^{-j\omega k}$$

where  $M < N$  and  $w(k)$  is real sequence satisfying the following conditions

$$0 \leq w(k) \leq w(0) = 1$$

$$w(-k) = w(k)$$

$$w(k) = 0, |k| > M.$$

All windows have a dominant relative narrow peak (main lobe around  $w=0$ ). Blackman Tukey is a locally weighted average of the periodogram.

The integrated electron density data is detrended and the single sided amplitude spectral estimate (i.e. square root of power spectral estimate) of this time series data is estimated using Blackman-Tukey spectral estimate with a Kaiser Window and is as shown in figure 3.8. The

peaks of the spectrum correspond to the periodicities in the data through which the scale sizes can be determined. In order to investigate the sizes we have assumed that these peaks are associated with ionization blobs if their amplitude is double the level of background ionization. However, we have included a couple of case studies to demonstrate the difference in results for different density threshold values at the end of this chapter. In the figure below there are ~8 peaks, but only 4 of them have sufficient amplitude to be labeled as ionization blobs.

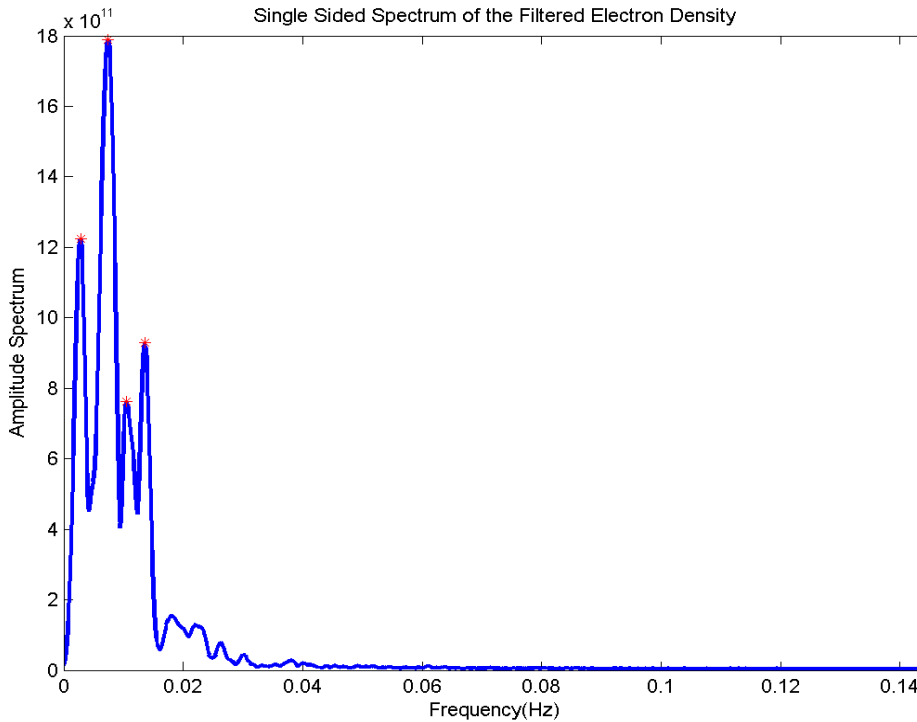


**Figure 3.8:** Single sided amplitude spectrum of integrated and detrended electron density data for about 12 minutes estimated using Blackman-Tukey spectral estimate (using Kaiser Window) a function of frequency.

As explained in chapter 2, LOS velocities are measured from multiple look directions and are resolved into ion drift velocities as a function of time and magnetic latitude (from  $66^{\circ}$ - $68^{\circ}$  with  $0.25^{\circ}$  steps). As the beams used in our experiment design are less and have higher elevation angles, their latitudinal coverage is less, which results in noisy velocity measurements in higher latitudes (above  $66.75^{\circ}$ ). The radar measured eastward ion velocity and northward ion velocity components as a function of time and magnetic latitude during the period of observation (for about 3 hours) are shown in Figure 3.9. From the figure it can be clearly seen that eastward ion velocities are noisy for latitude greater than magnetic latitude  $66.75^{\circ}$ . In the auroral zone during

night time, east-west ion velocity component is substantially greater than the north-south ion velocity component.

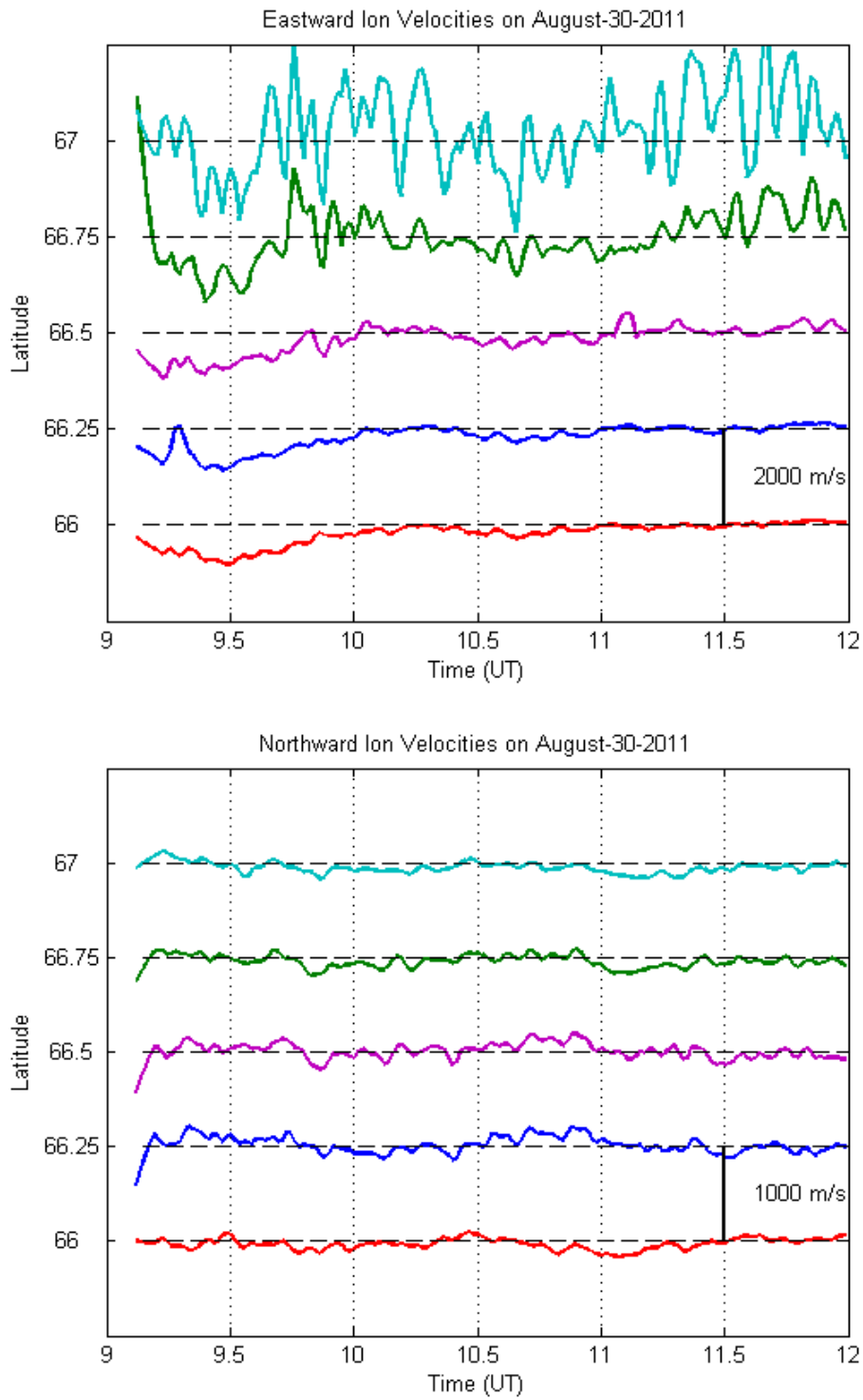


**Figure 3.9:** (a) Eastward ion velocities and (b) Northward ion velocities from 9-12 UT on 30 August 2011 as a function of time and magnetic latitude.



In order to determine the spatial size of ionization blobs, the electron density structures are assumed to be moving with a constant velocity for 12 minute periods. The average eastward ion velocity and northward ion velocity is calculated by taking an average of magnitude of ion velocities across the magnetic latitude bins  $66^{\circ}$  -  $66.75^{\circ}$  and across the time bins. The total ion velocity or the velocity with which the blobs are moving is the square root of sum of the squares of averaged eastward ion velocity and northward ion velocity. Using the peaks of the spectrum and the ion velocity information the horizontal structure of the blobs can be determined by using the formula

$$\begin{aligned} & \textit{Horizontal structure or wavelength of blob} \\ & = \textit{Total ion velocity} / \textit{peaks of the spectrum.} \end{aligned}$$

This process is repeated for the whole observation period and scales sizes are measured and plotted using a bar graph as shown in Figure 3.10. As significant amount of smoothing of electron density data is done, ionization blobs with scale sizes less than 10 km are not apparent and irregularity structures with more than 300 km scale are not considered blobs. For this reason we studied the ionization blobs with scale sizes ranging from 10-300 km which forms our experimental limit.

The observations of blob scale sizes were made from 2011 to 2013 under varying conditions of geomagnetic activity. The  $K_p$  index quantifies the level of geomagnetic activity and is derived by calculating a weighted average of local K-indices from a global network of geomagnetic observatories. The  $K_p$  index scale has a range from 0 to 9 and is directly related to the maximum amount of fluctuation (relative to a quiet day) in the geomagnetic field.

It is common to forecast the level of auroral activity (active, medium and quiet) based on the planetary magnetic index  $K_p$ . Quiet conditions, indicated by a  $K_p \leq 1$ , have minimal auroral activity overhead of Poker Flat, Alaska as shown in Figure 3.11. During quiet conditions, when the magnetic activity is low, the radar is located in a region of low plasma velocities (100-500 m/s) well south of the auroral oval (essentially a mid-latitude type ionosphere). During moderate conditions ( $K_p = 2$  or  $3$ ), auroral activity will be minimal overhead of Poker Flat, Alaska as shown in Figure 3.12. During moderate conditions, when the magnetic activity is moderate, the radar is located in a region of medium plasma velocities (300-600 m/s) in the vicinity of the

auroral oval. During disturbed or active conditions ( $K_p \geq 4$ ), auroral activity will be high overhead of Poker Flat, Alaska as shown in Figure 3.13.

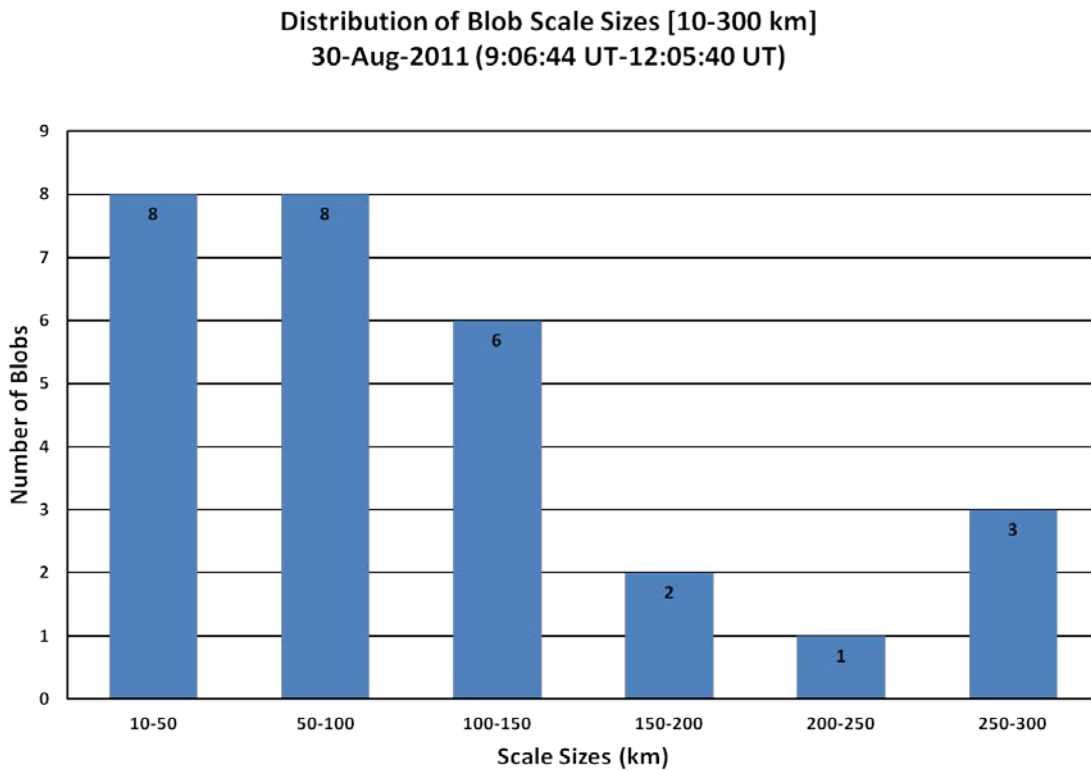


**Figure 3.10:** Bar graph of blob occurrence as a function of scale sizes on 30 August 2011.

During disturbed conditions, when the magnetic activity is high, the radar is located in the region of strong auroral east-west plasma velocities. Though the  $K_p$  scale is a reasonable way to summarize the global level of geomagnetic activity, the disturbance of the local geomagnetic field may also be used as an indicator of local conditions. This thesis uses both  $K_p$  and Alaskan magnetometer data values to determine the level of geomagnetic activity.

As mentioned earlier, in order to determine the sizes of blobs we have limited our study to the electron density enhancements that are at least double the background density. The variation in the distribution of ionization blob scale sizes for different density threshold values is discussed here. Figure 3.14 and 3.15 shows the distribution of ionization blob scale sizes determined using different threshold values (i.e., 25% above the background, 50% above the background and double the background) during slightly active conditions and disturbed conditions respectively. In both cases the number of blobs with scale sizes ranging from 10-100

km tends to increase with the decrease in the level of threshold value as expected. Blobs with scale sizes ranging from 100-300 km are constant irrespective of the threshold value.

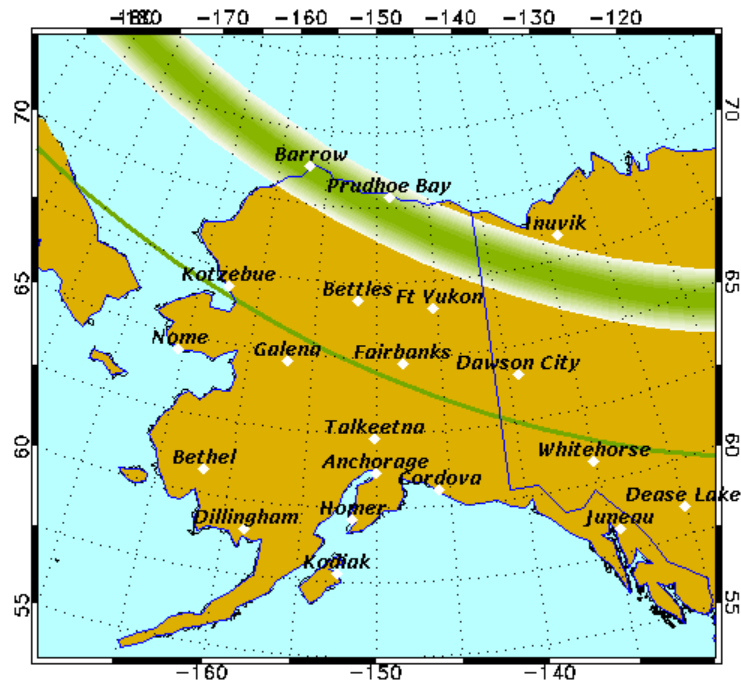


**Figure 3.11:** Auroral activity during quiet conditions ( $K_p \leq 1$ ) over Alaska.

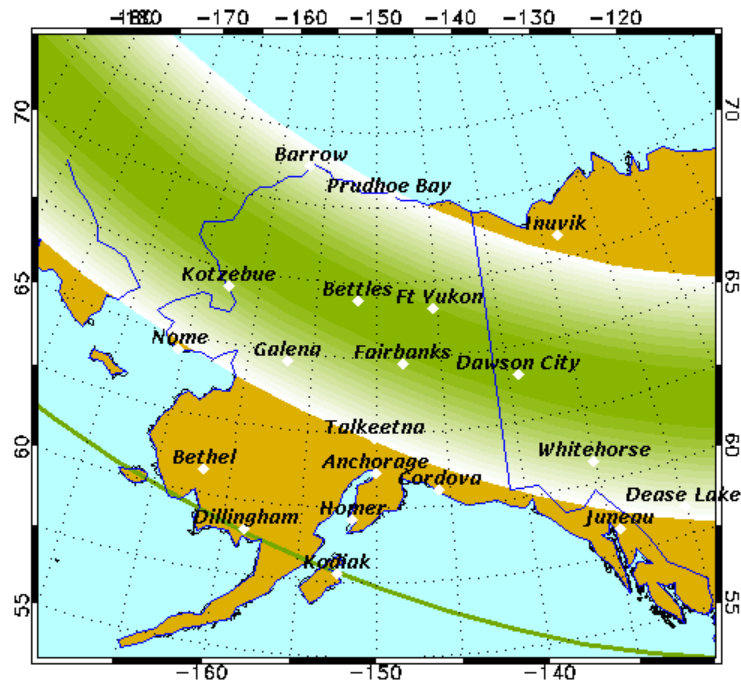


**Figure 3.12:** Auroral activity during moderate conditions ( $2 \leq K_p \leq 3$ ) over Alaska.

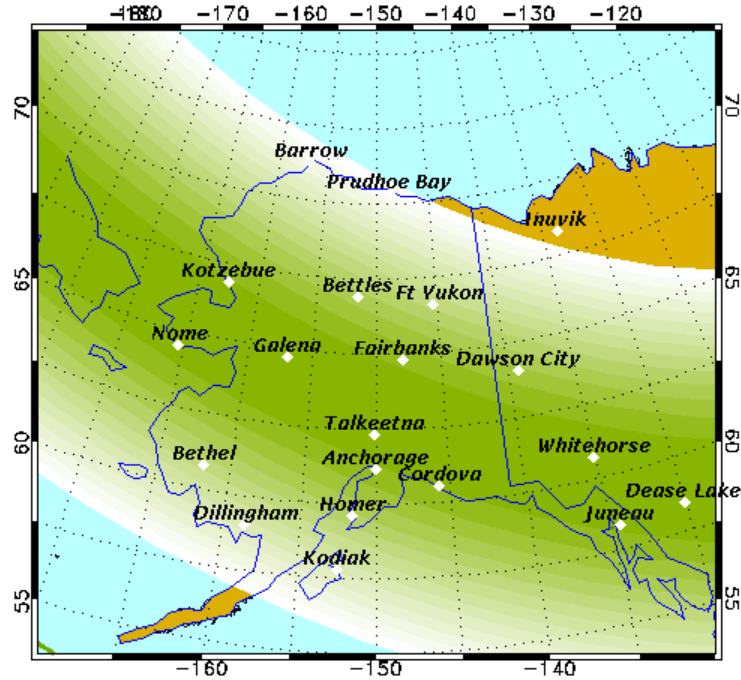


**Figure 3.13:** Auroral activity during disturbed conditions ( $K_p \geq 3$ ) over Alaska.

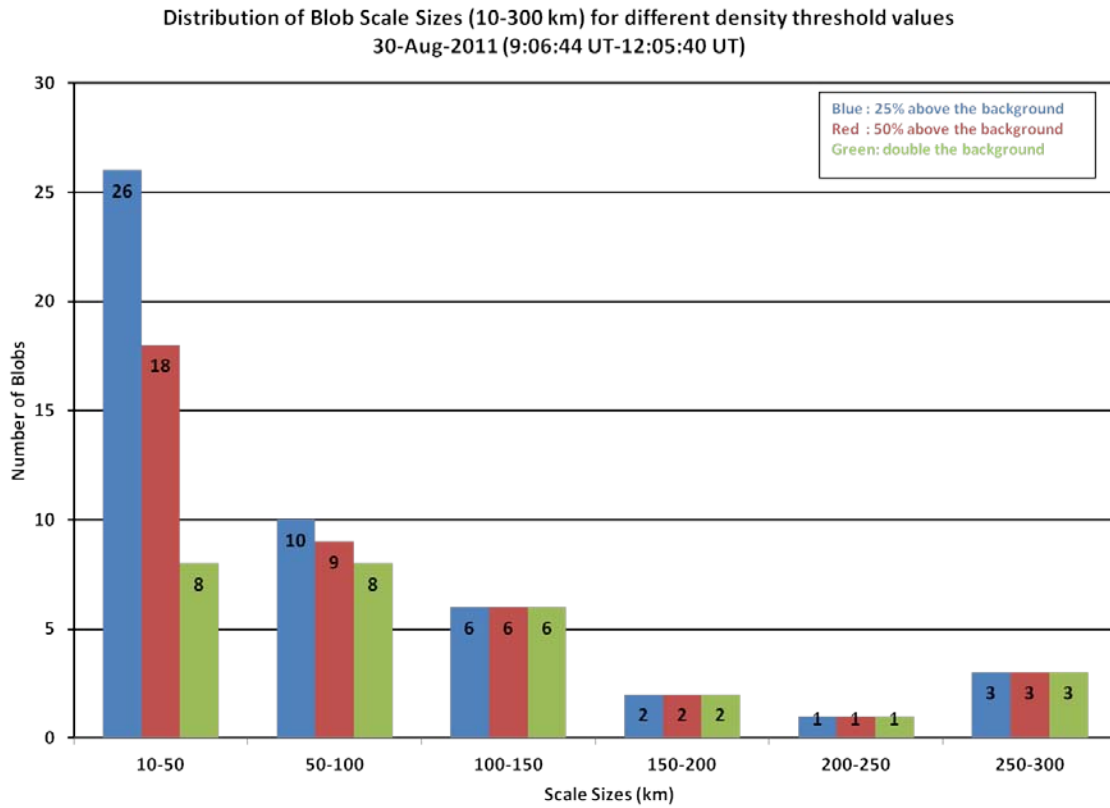


**Figure 3.14:** Distribution of ionization blob scale sizes for different density threshold values during slightly active conditions ( $K_p = 2$ ).

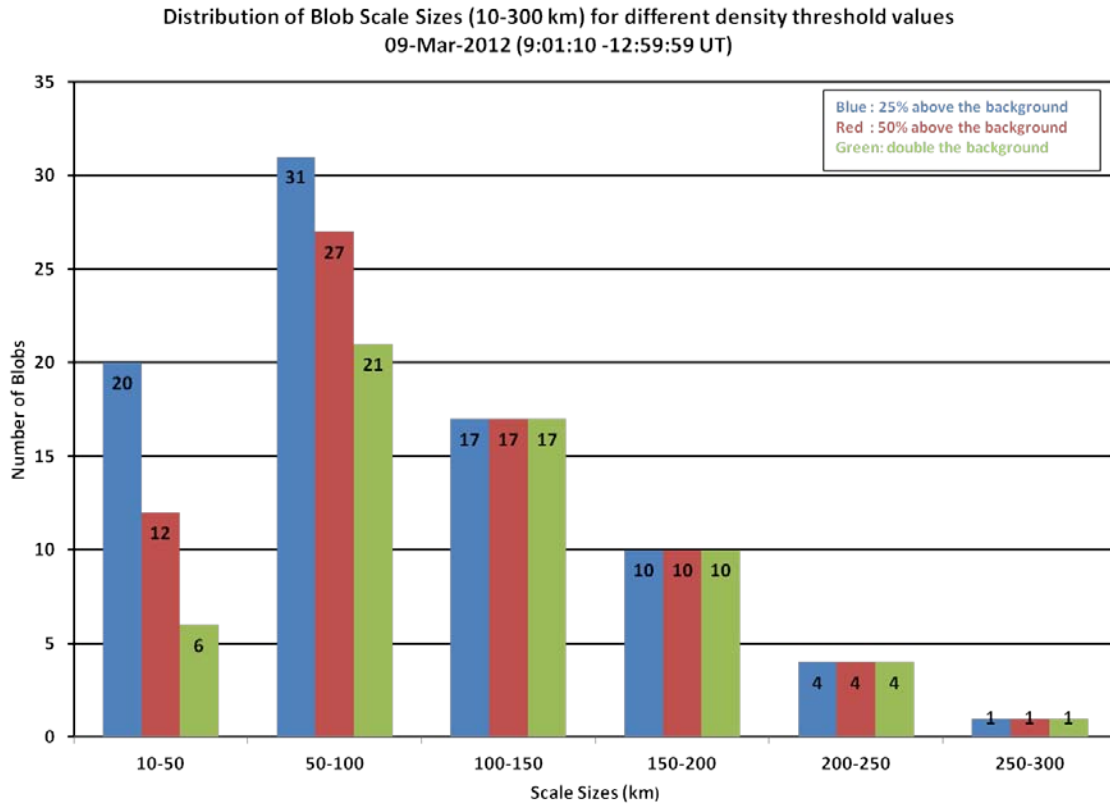


**Figure 3.15:** Distribution of ionization blob scale sizes for different density threshold values during disturbed conditions ( $K_p = 5$ ).

## CHAPTER 4. OBSERVATIONS OF ELECTRON DENSITY IRREGULARITIES USING THE POKER FLAT INCOHERENT SCATTER RADAR

### 4.1. Introduction

Electron density irregularity observations using the high-resolution mode were carried out on fourteen different nights for three to four hour periods near magnetic midnight using the incoherent-scatter radar located at the Poker Flat Research Range, Alaska as shown in Table 4.1. Electron density irregularity structures with varying horizontal scale sizes are observed on all the nights. Several distinctive results, as indicated with shading in Table 4.1, are discussed in this chapter. The summary of the findings is discussed at the end of this chapter.

**Table 4.1:** Operations carried out using Poker Flat Incoherent-scatter radar from Aug, 2011-Jan, 2013.

<b>Date</b>	<b>Start Time (UT)</b>	<b>End Time (UT)</b>	<b>Description</b>	<b>Estimated Planetary kp index</b>
27 August 2011	09:05:58	12:05:23	Very quiet magnetic conditions at both Poker Flat and Ft Yukon.	0
28 August 2011	09:06:09	12:05:30	Slightly active conditions at the radar site with moderately active conditions at Ft Yukon.	2
29 August 2011	09:06:17	12:05:25	Active conditions at both Poker Flat and Ft Yukon	4
30 August 2011	09:06:44	12:05:40	Slightly active conditions at the radar site with moderately active conditions at Ft Yukon.	2
31 August 2011	09:06:34	12:05:37	Very quiet magnetic conditions at both Poker Flat and Ft Yukon.	1
09 March 2012	09:01:10	12:59:59	Very disturbed conditions at both Poker Flat and Ft Yukon.	7
25 March 2012	09:01:13	13:00:02	Slightly active conditions at both Poker Flat and Ft Yukon	2
26 March 2012	09:01:03	12:59:52	Slightly active conditions at the radar site with moderately active conditions at Ft Yukon.	2

**Table 4.1 continued:**

09 October 2012	07:01:14	09:59:54	Very disturbed conditions at both Poker Flat and Ft Yukon.	5
12 October 2012	07:01:00	10:00:10	Moderately active conditions at both the stations.	3
19 October 2012	07:00:58	09:59:53	Very quiet magnetic conditions at both Poker Flat and Ft Yukon.	0
03 November 2012	07:00:54	10:00:04	Bad data.	0
04 November 2012	07:01:19	09:59:59	Very quiet magnetic conditions at both Poker Flat and Ft Yukon with slightly active conditions at Kaktovik [North of Poker Flat]	1
15 January 2013	07:01:03	09:59:58	Slightly active conditions at the radar site with moderately active conditions at Ft Yukon.	2

## 4.2. Results

### 4.2.1. August 28th, 2011

The first set of experiments was run in August 2011 from 09-12 UT to observe the scale sizes of electron density blobs during the midnight time sector. Figure 4.1 shows the magnetometer data from Poker Flat and Ft Yukon for 28 August 2011. Slight magnetic perturbations can be seen at Poker Flat with strong perturbations at Ft Yukon, which is present at a higher latitude north of Poker Flat. Magnetometer data from these stations suggest that there is an onset of westward current north of Ft Yukon at ~8:40 UT and ~10:00 UT. Observations from PFISR and Alaskan magnetometers from 09-12 UT on 28 August 2011 are incorporated and shown in Figure 4.2. Figure 4.2 shows H, D and Z components of the ground magnetic variations recorded by the magnetometers at Poker Flat and Ft Yukon (Figure 4.2a), electron density (Figure 4.2b), electron temperature (Figure 4.2c), eastward ion velocities (Figure 4.2d) and northward ion velocities (Figure 4.2e). Electron density and electron temperature from the vertical beam are shown with ~1 min time resolution while the ion velocity data here was processed at ~30 sec time resolution. Details for the figure 4.2 format are described in the caption.

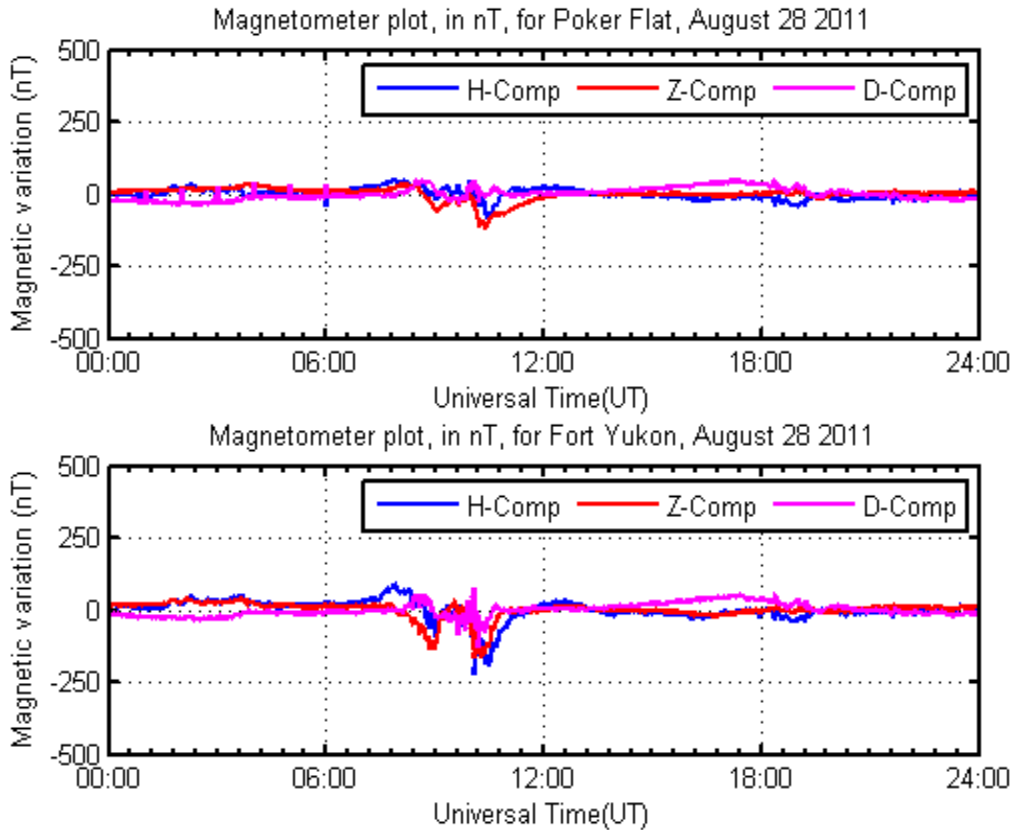
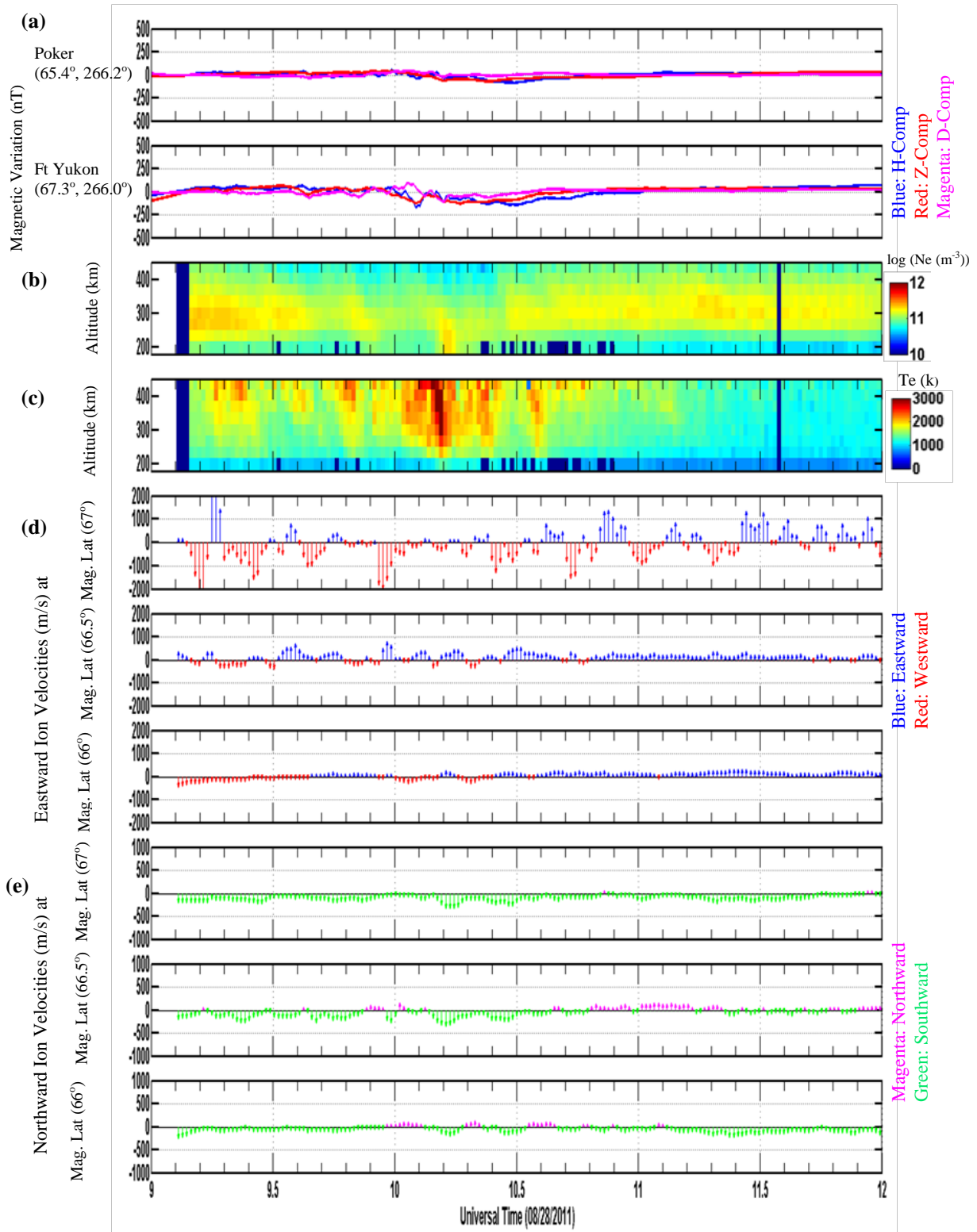


**Figure 4.1:** Magnetometer data from Poker Flat and Ft Yukon on 28 August 2011. [Onset of westward current is noted from onset of the negative excursion of the magnetic H component and Z component indicates the location of the substorm current].

---

\*Figure 4.2: (a) Magnetic perturbations of H (blue), Z (red) and D (magenta) components recorded by two Alaska magnetometers that are roughly at the same local time are shown as a function of universal time. The name and geomagnetic location of each magnetometer are shown to the left. (b-c) Electron density (corrected for  $T_e/T_i$  or Debye length effects) and electron temperature measured by the vertical beam using the long pulse measurements of PFISR are shown as a function of altitude (from 180 km to 450 km) and universal time. (d) Eastward velocity flows measured at mag. lat  $66^\circ$ ,  $66.5^\circ$  and  $67^\circ$  by PFISR are shown as a function of magnitude and universal time. In Figure 4.2d, flows with eastward components are blue, and those with westward components are red. (e) Northward velocity flows measured at magnetic latitude  $66^\circ$ ,  $66.5^\circ$  and  $67^\circ$  by PFISR are shown as a function of magnitude and universal time. In Figure 4.2e, flows with northward components are magenta, and those with southward components are green. Eastward and Northward plasma flows are plotted without removing any measurement uncertainties.

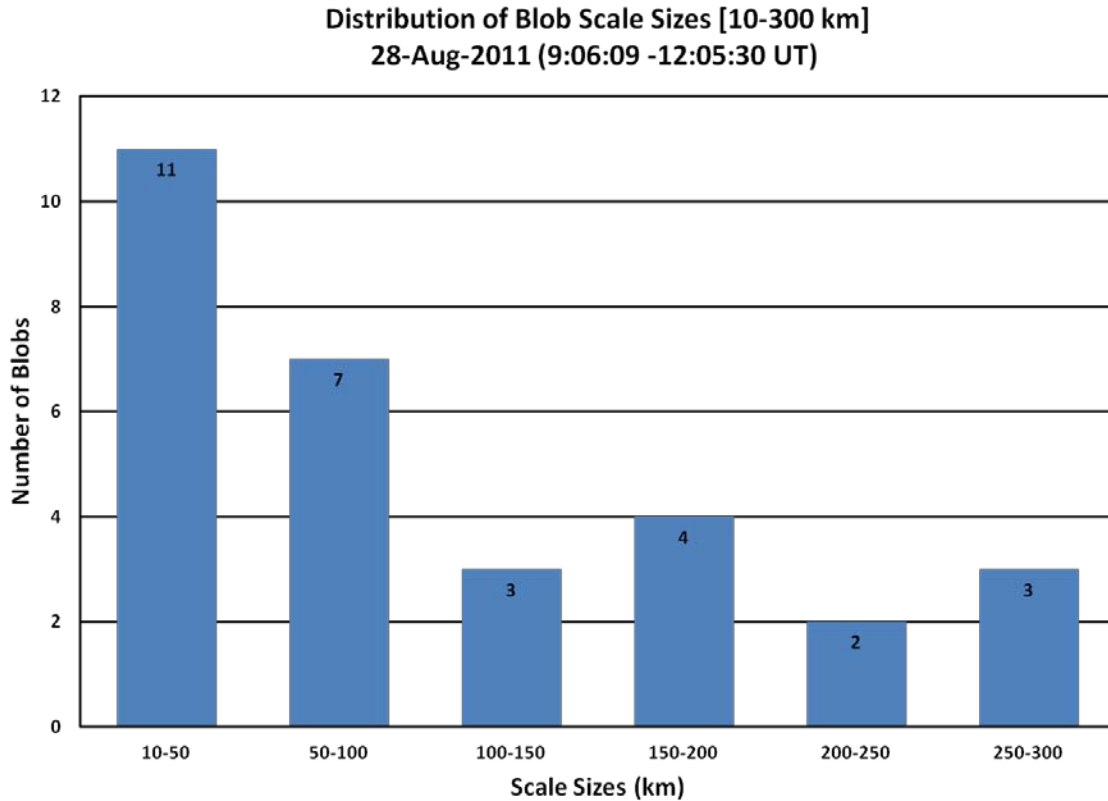




**Figure 4.2:** Magnetometer data and PFISR results for the night of 28 August 2011 from 09-12 UT.

As shown in Figure 4.2, the ionization profile from the vertical beam show electron density irregularity structures in the F-region throughout the observation period. Strong auroral ionization seen at around 180 km at ~10:00 UT is clearly related to the onset of westward currents that is evident by the negative excursion of the magnetic H component. Electron density and electron temperature observations from 9:00-11:00 UT show the presence of electron density structures roughly associated with an increase in electron temperature and suggest that these structures are formed locally due to soft particle precipitation [e.g. Kelley et al., 1982]. Structures observed during the remaining period of observation are not produced locally as there is no indication that electron temperature increases. This suggests that these structures are transported from the polar cap or high-latitude region [e.g. Robinson et al., 1985]. Due to the onset of westward current north of Ft Yukon at ~10 UT, the radar-measured eastward ion velocity component from magnetic latitude  $66^{\circ}$ - $66.75^{\circ}$  is directed eastward with an average velocity of ~343.3 m/s. Northward ion velocity data from magnetic latitude  $66^{\circ}$ - $66.75^{\circ}$  is directed southward with an average velocity of ~ 81 m/s indicating that the blobs are moving with an average total velocity of ~ 340 m/s. Ion velocity data from magnetic latitude  $67^{\circ}$ - $68^{\circ}$  has very high measurement uncertainty due to poor signal-to-noise ratio, therefore velocity information from these latitudes is not used in determining the scale sizes of blobs.

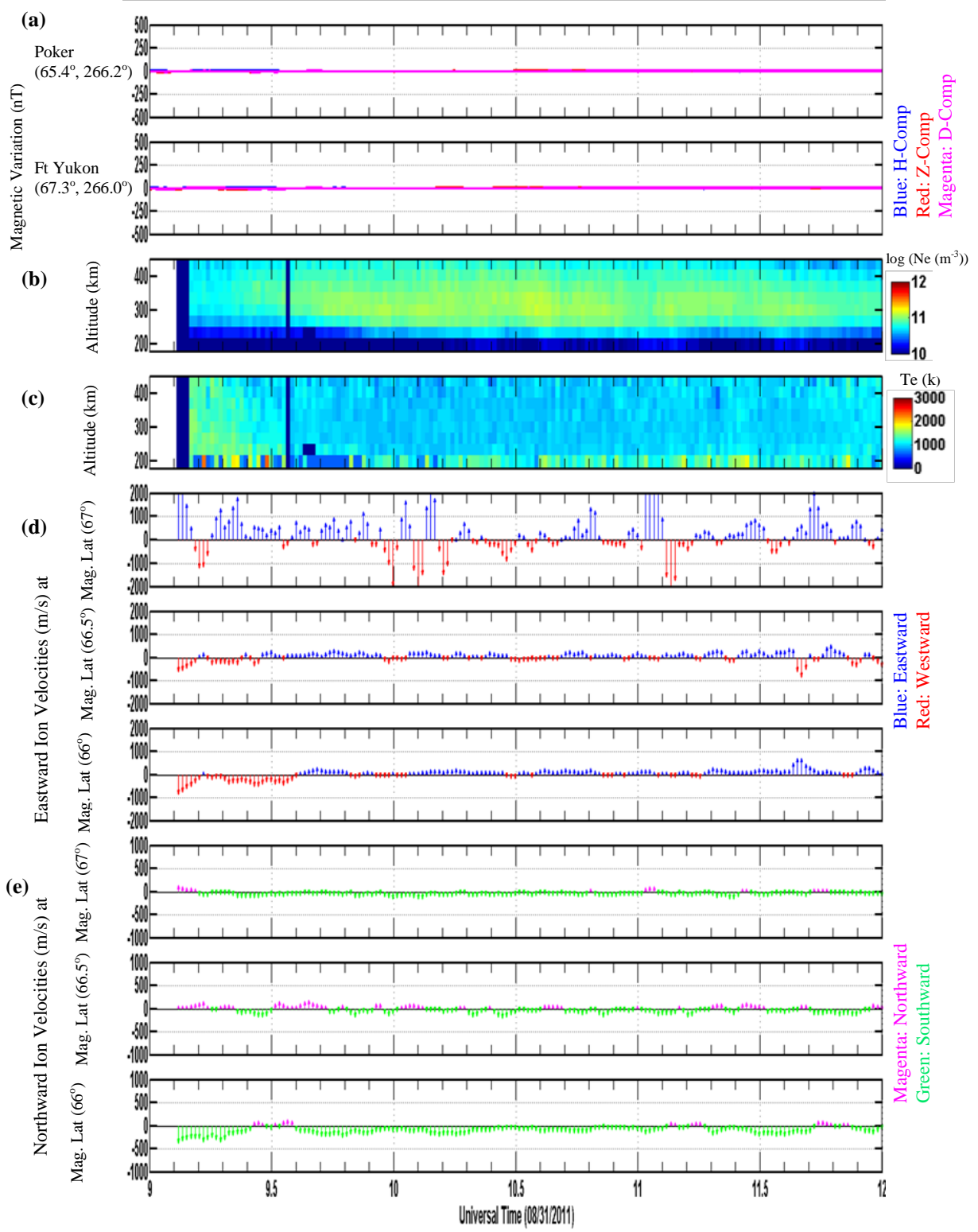
Figure 4.3 shows the occurrence of ionization blobs as a function of scale size. These blob scale sizes are calculated using the approach explained in chapter 3. Electron density structures with scale sizes less than 10 km and more than 300 km are not taken into account as they are outside the experimental limits of our technique. From Figure 4.2 it can be clearly seen that the size distribution maximizes in the range of 10-50 km and 50-100 km scale sizes.



**Figure 4.3:** Bar graph of blob occurrence as a function of scale sizes on 28 August 2011.

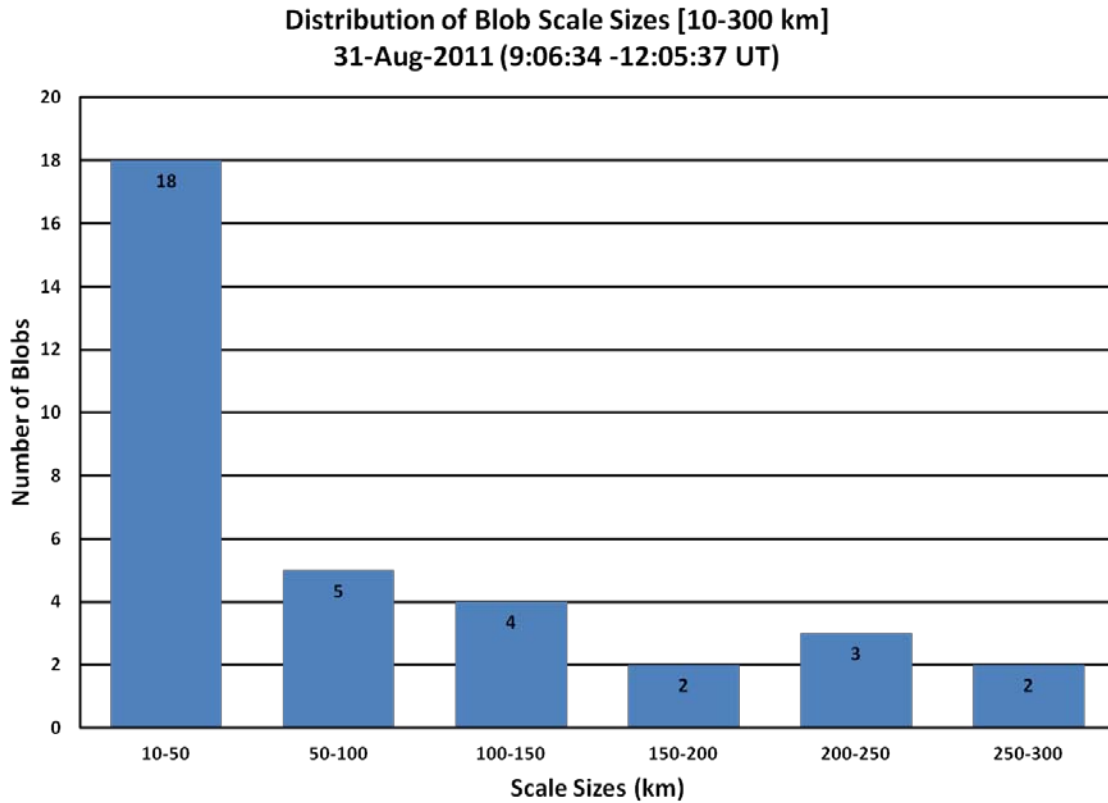
#### **4.2.2. August 31<sup>st</sup>, 2011**

Figure 4.4 shows the observations from PFISR and Alaskan magnetometers from 09-12 UT on 31 Aug 2011. As shown in Figure 4.4a, quiet magnetic conditions were observed at both the stations. Ionization profile data show the presence of density structures from 9:40-11:40 UT with no evidence of an increase in electron temperature that suggests these elongated enhancements are not formed locally and are likely convected horizontally into the radar field of view as the F-region ionosphere plasma has a long recombination lifetime. As the perturbations in the H component of the magnetic field show no sign of substorm activity, it is suggested that the auroral oval is located well poleward of the radar and that convection flows are very low. The radar measured eastward ion velocity component from magnetic latitude  $66^{\circ}$ - $66.75^{\circ}$  shows near zero east-west plasma flows with an average velocity of  $\sim 214$  m/s. The northward ion velocity component from magnetic latitude  $66^{\circ}$ - $66.75^{\circ}$  is directed southward with an average velocity of  $\sim 42$  m/s, indicating that the ionization blobs are moving with an average total velocity of  $\sim 220$  m/s.



**Figure 4.4:** Magnetometer data and PFISR results for the night of 31 August 2011 from 09-12 UT.

Figure 4.5 shows the occurrence of ionization blobs as a function of scale size. From this figure, it can be clearly seen that the size distribution of blobs maximizes in the range of 10-50 km scale size. The lower level of occurrence of blobs with 50-300 km scale sizes is associated with short-term variations in eastward velocity component.



**Figure 4.5:** graph of blob occurrence as a function of scale sizes on 31 August 2011.

#### 4.2.3. March 9<sup>th</sup>, 2012

The second set of experiments was run in March 2012 from 9-13 UT to observe the scale sizes of blobs for about four hours around midnight. As shown in figure 4.6, very strong perturbations of H component are observed at both the stations, indicating the presence of intense substorm activity, which indicates a storm event. On this day the conditions are very disturbed before and during the period of study.

Figure 4.7 shows the observations from PFISR and Alaskan magnetometers from 09-13 UT on 09 March 2012. Elongated electron density enhancements associated with an increase in electron temperature are observed throughout the period of observation suggest that these structures are formed locally near the observation region. As the magnetic conditions are

disturbed, the plasma velocities are much higher and the eastward ion velocity component from magnetic latitude  $66^{\circ}$ - $66.75^{\circ}$  is directed eastward with an average velocity of  $\sim 773$  m/s and northward ion velocity from magnetic latitude  $66^{\circ}$ - $66.75^{\circ}$  is directed southward with an average velocity of  $\sim 412$  m/s, indicating that the blobs are moving southeast with an average total velocity of  $\sim 876$  m/s.

The distribution of blob occurrence as a function of scale size, as shown in Figure 4.8, indicates that the size distribution of ionization blobs maximizes in the range of 50-200 km scale sizes.

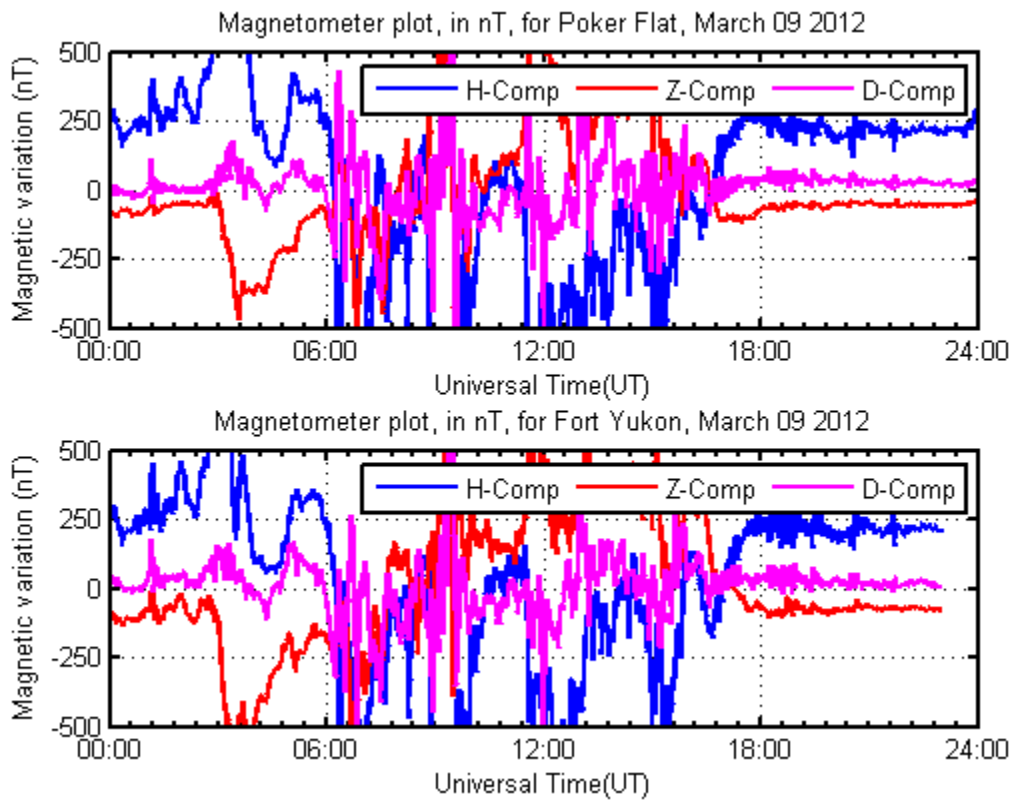


**Figure 4.6:** Magnetometer data from Poker Flat and Ft Yukon on 09 March 2012.

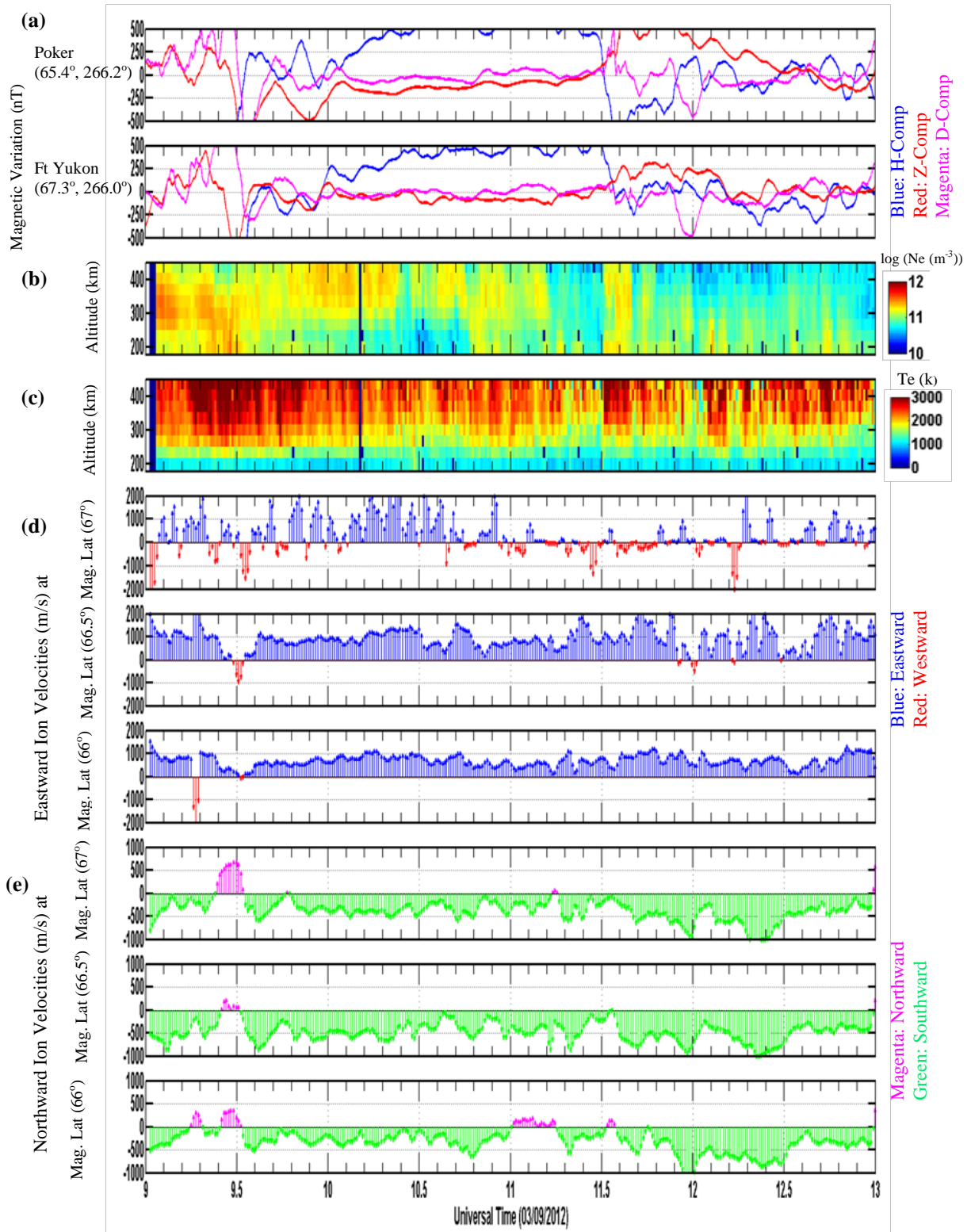


**Figure 4.7:** Magnetometer data and PFISR results for the night of 09 March 2012 from 09-13 UT

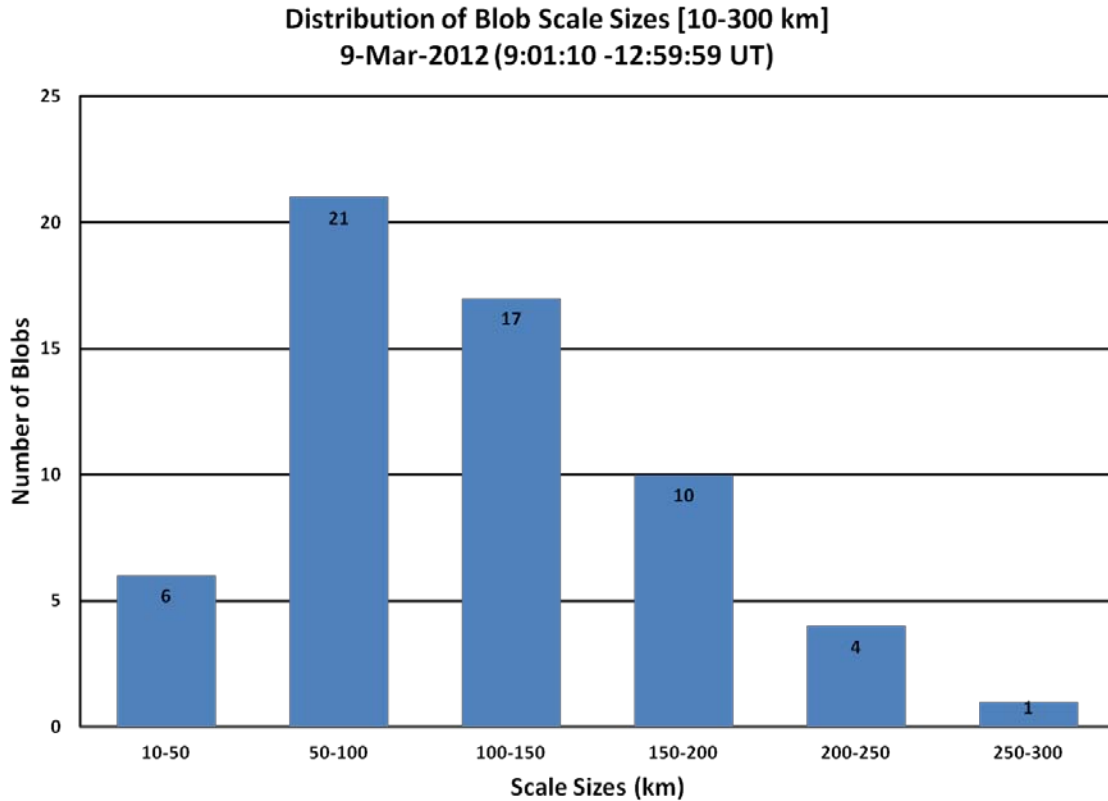


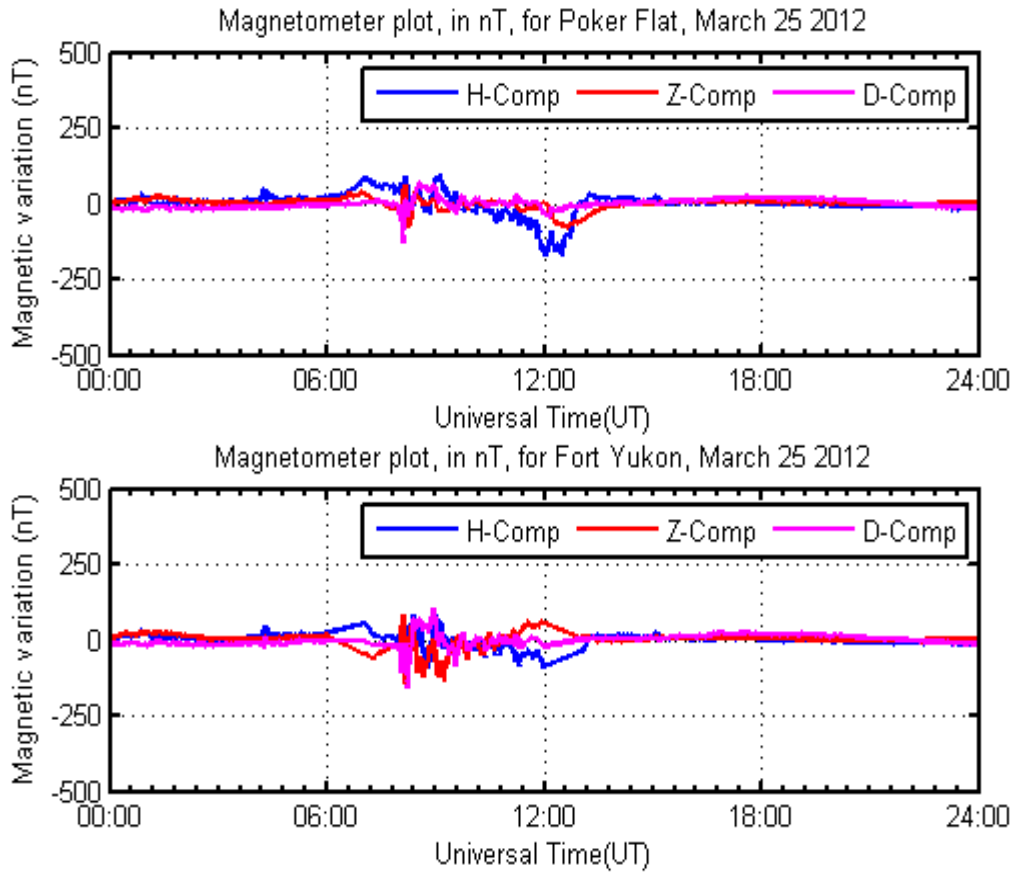
**Figure 4.8:** Bar graph of blob occurrence as a function of scale sizes on 09 March 2012.

#### **4.2.4. March 25<sup>th</sup>, 2012**

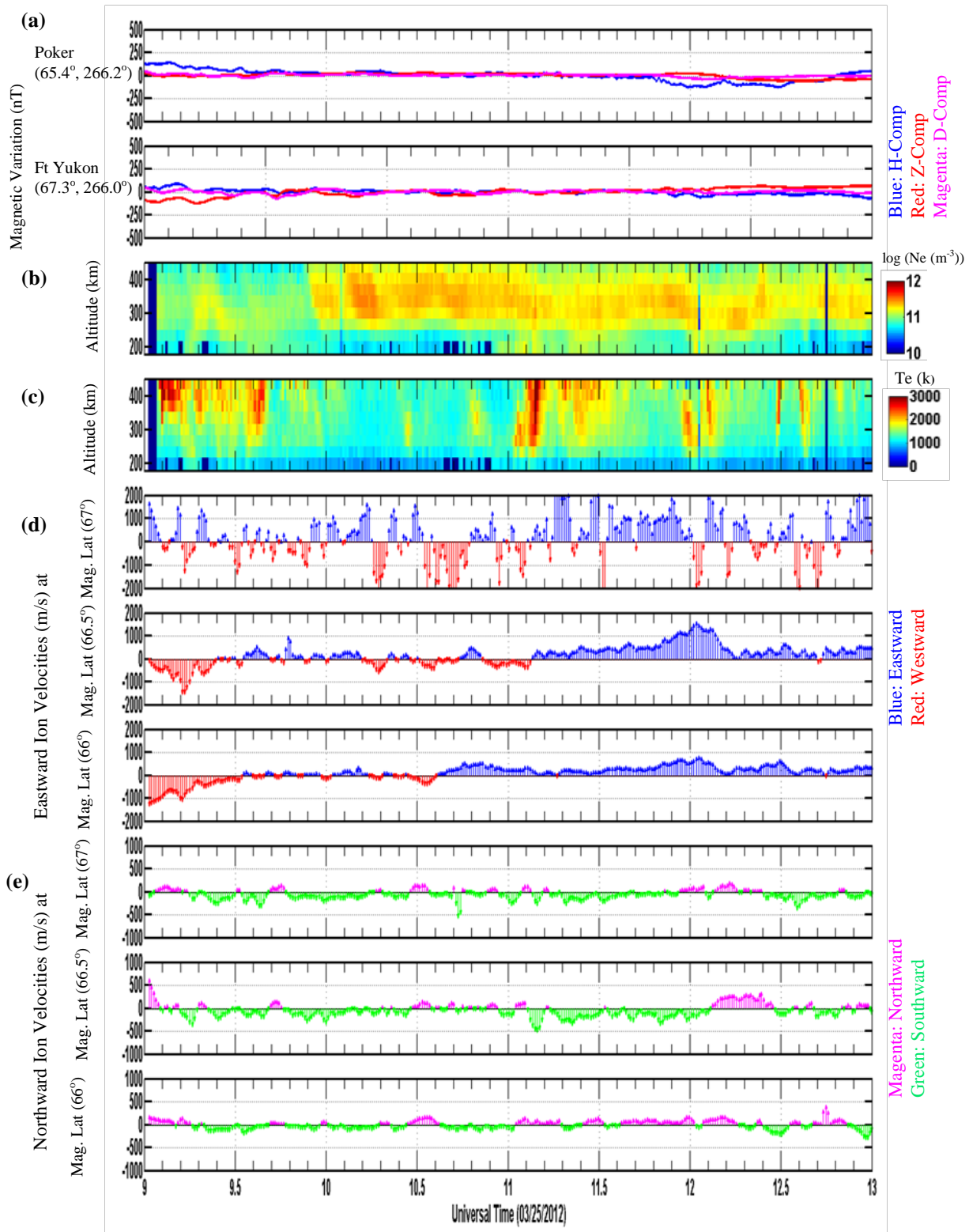
As shown in Figure 4.9, slight magnetic variations of the H component are observed at both stations. During this night, there is an onset of westward current overhead of the radar site at ~10:40 UT. Figure 4.10 shows the observations from PFISR and Alaskan magnetometers from 09-13 UT on 25 March 2012. Ionization profile and electron temperature clearly show the presence of locally-formed and horizontally- convected enhanced structures throughout the period of observation. From 9:00-9:30 UT, eastward ion velocity at magnetic latitude  $66^{\circ}$ -  $66.75^{\circ}$  is directed westward. There is an increase in magnitude of westward flow leading to near zero east-west plasma velocities for about 60-90 minutes during the growth phase prior to the onset of the substorm (i.e. ~10:40 UT). Just before substorm onset, the westward plasma flow changes to eastward flow (i.e. westward current). The average eastward plasma velocity during this period is ~476 m/s where as the northward ion velocity from magnetic latitude  $66^{\circ}$ -  $66.75^{\circ}$  is directed southward with an average velocity of ~47 m/s, indicating that the blobs are moving with an average total velocity of ~479 m/s in the southwest direction.



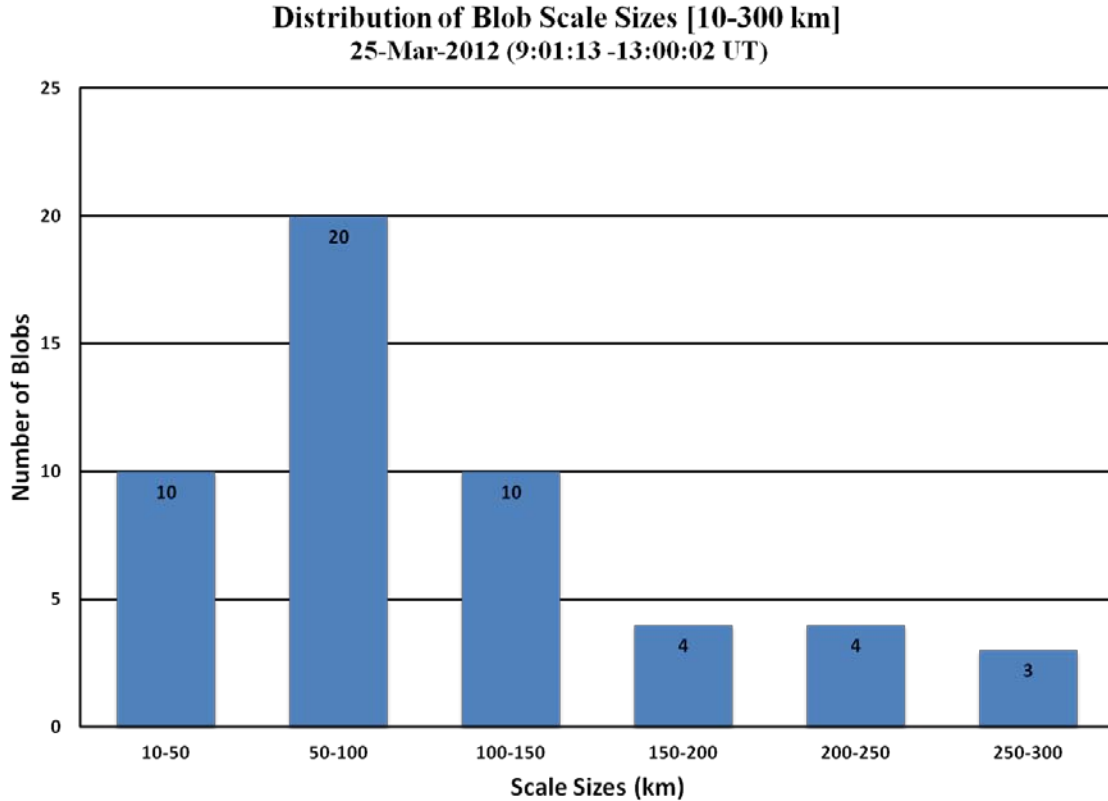
Figure 4.11 shows the occurrence of blobs as a function of scale sizes. Electron density blobs with 50-150 km scale sizes are dominant during this night, as shown in this figure.



**Figure 4.9:** Magnetometer data from Poker Flat and Ft Yukon on 25 March 2012.



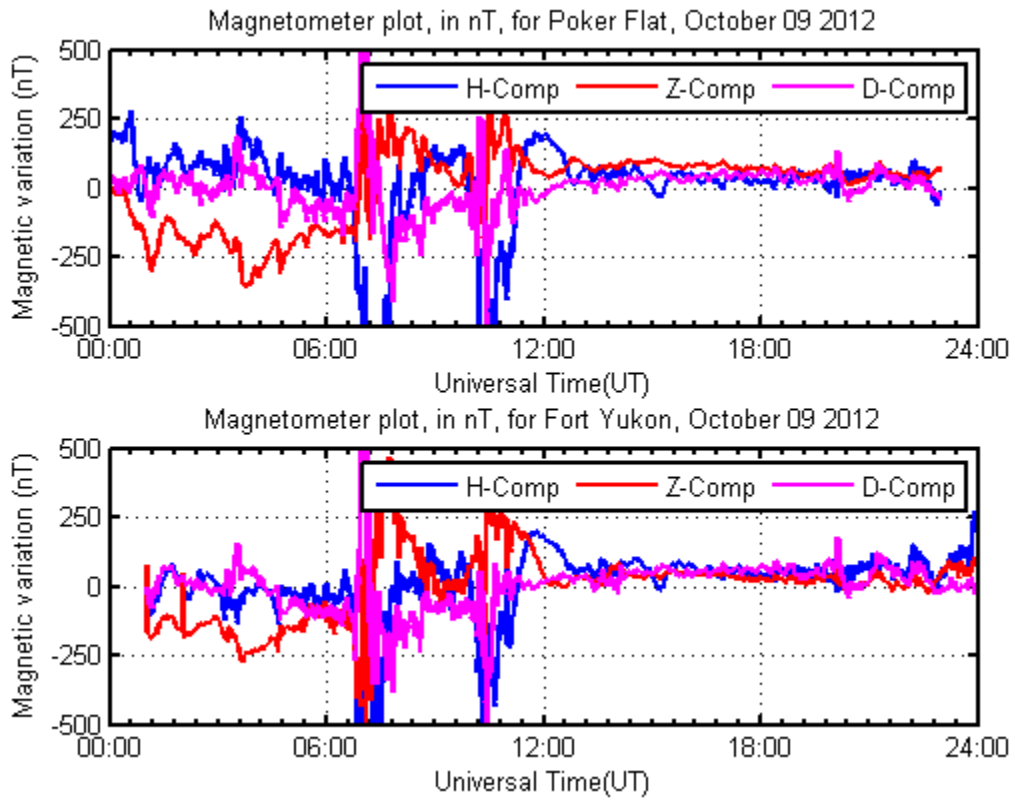
**Figure 4.10:** Magnetometer data and PFISR results for the night of 25 March 2012 from 09-13 UT.



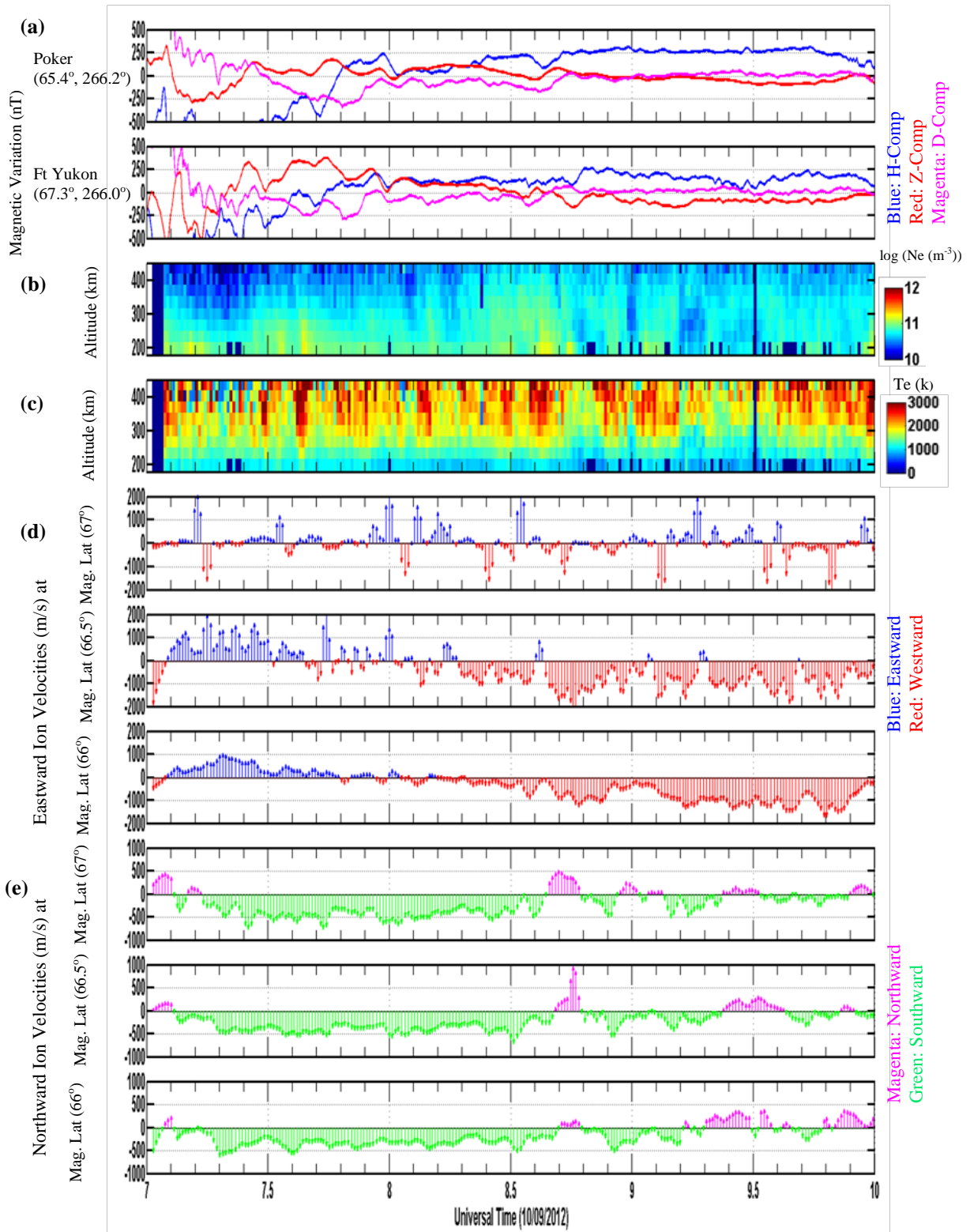
**Figure 4.11:** Bar graph of blob occurrence as a function of scale sizes on 25 March 2012.

#### 4.2.5. October 9<sup>th</sup>, 2012

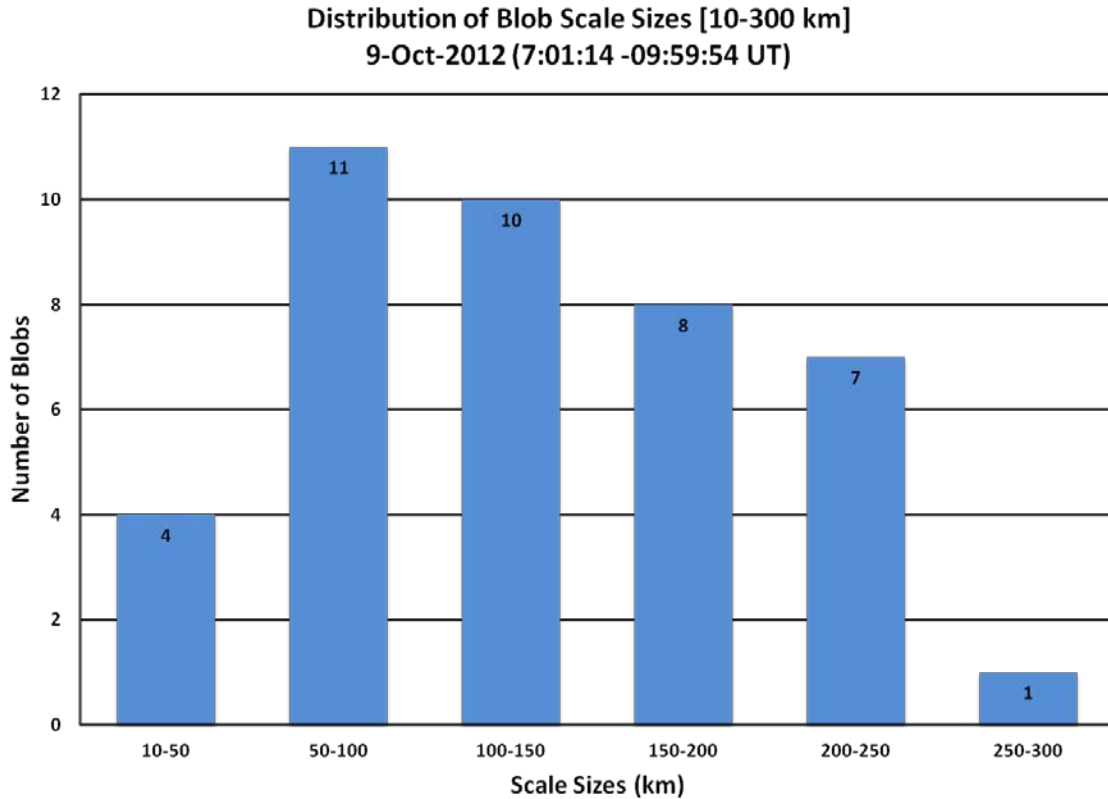
The third set of experiments was run from Oct 2012 to Jan 2013 from 7-10 UT to observe the enhanced electron density structures during the evening time sector. As shown in Figure 4.12, intense variations of the H component are observed at both stations. On this night, there is an onset of two substorm events with a gap of two hours. The first hour of observation is associated with the recovery phase of the first substorm and there is another onset of a substorm just after the period of observation. Figure 4.13 shows the observations from PFISR and Alaskan magnetometers from 07-10 UT on 09 March 2012. Ionization profile and electron temperature plots show the structures with enhanced temperatures. Plasma flow is directed eastward during the first hour due to the onset of westward currents just before the period of observation, and during the remaining period the plasma flow is directed westward. The average magnitude of eastward plasma flow is  $\sim 640$  m/s. Northward plasma flow is directed southward with an average velocity of  $\sim 275$  m/s. Figure 4.14 clearly shows that ionization blobs with scale sizes ranging from 50-250 km are dominant during this night.



**Figure 4.12:** Magnetometer data from Poker Flat and Ft Yukon on 09 October 2012.



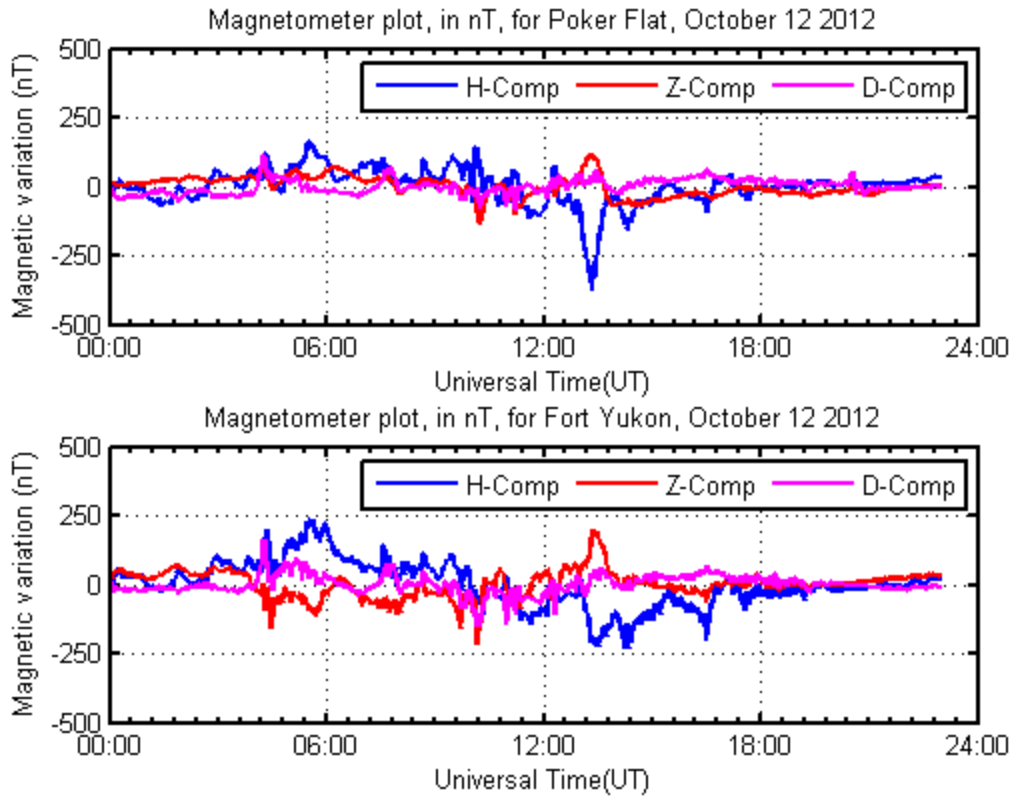
**Figure 4.13:** Magnetometer data and PFISR results for the night of 09 October 2012 from 07-10 UT.



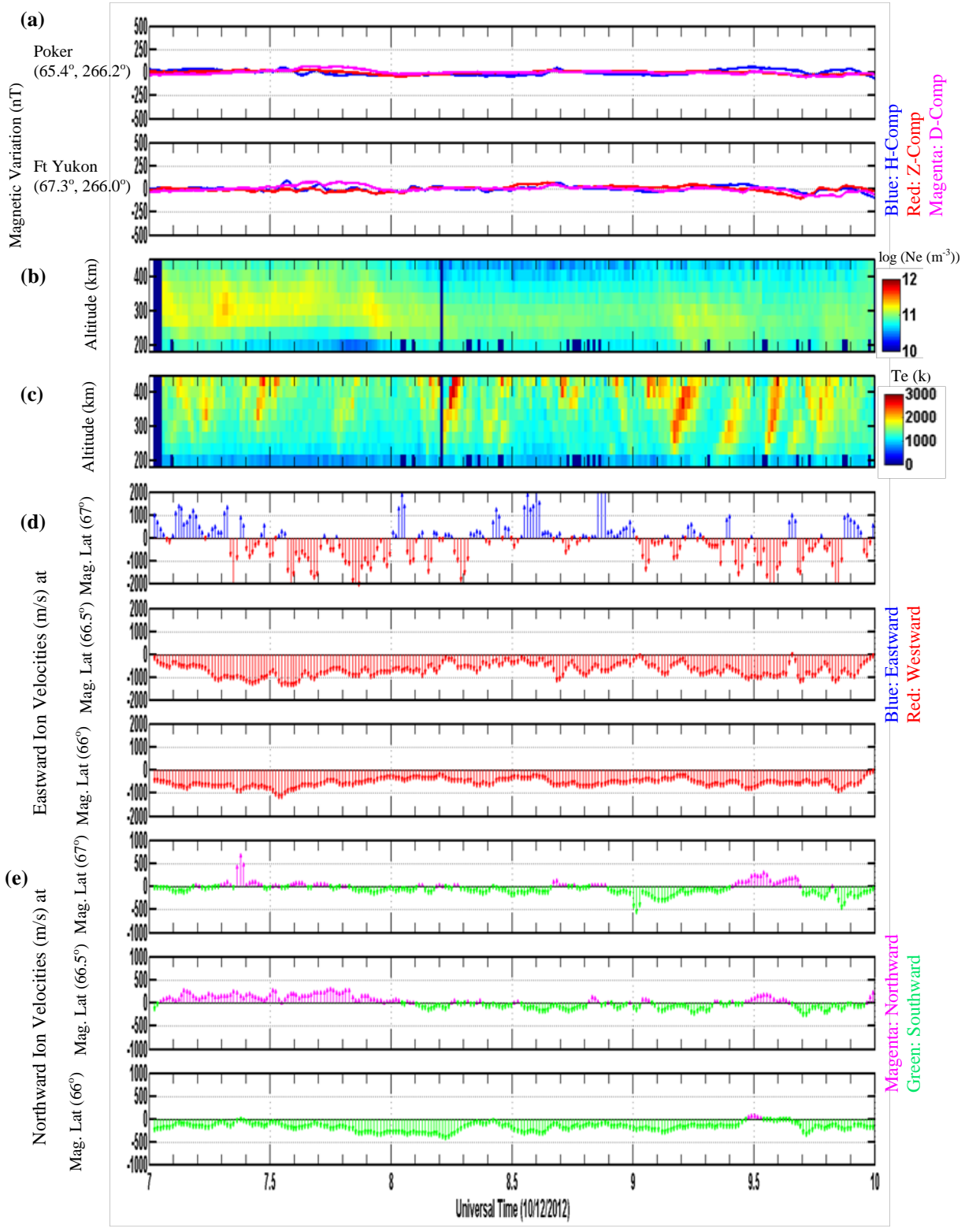
**Figure 4.14:** graph of blob occurrence as a function of scale sizes on 09 October 2012.

#### 4.2.6. October 12<sup>th</sup>, 2012

As shown in Figure 4.15, Slight perturbations of the H component can be observed at both stations. There is an onset of substorm activity at around 11 UT on this day, suggesting active conditions. Figure 4.16 shows the observations from PFISR and Alaskan magnetometers from 07-10 UT on 12 October 2012. Ionization profile and electron temperature data clearly show the presence of locally-formed and horizontally- convected enhanced structures throughout the period of observation. The eastward plasma flow is directed westward with an average velocity of  $\sim 800$  m/s and northward plasma flow is directed mostly southward with an average velocity of  $\sim 80$  m/s, indicating that the blobs are moving with an average velocity of  $\sim 805$  m/s. Figure 4.17 clearly shows that the occurrence of ionization blobs with scale sizes ranging from 50-200 km is high during this night.

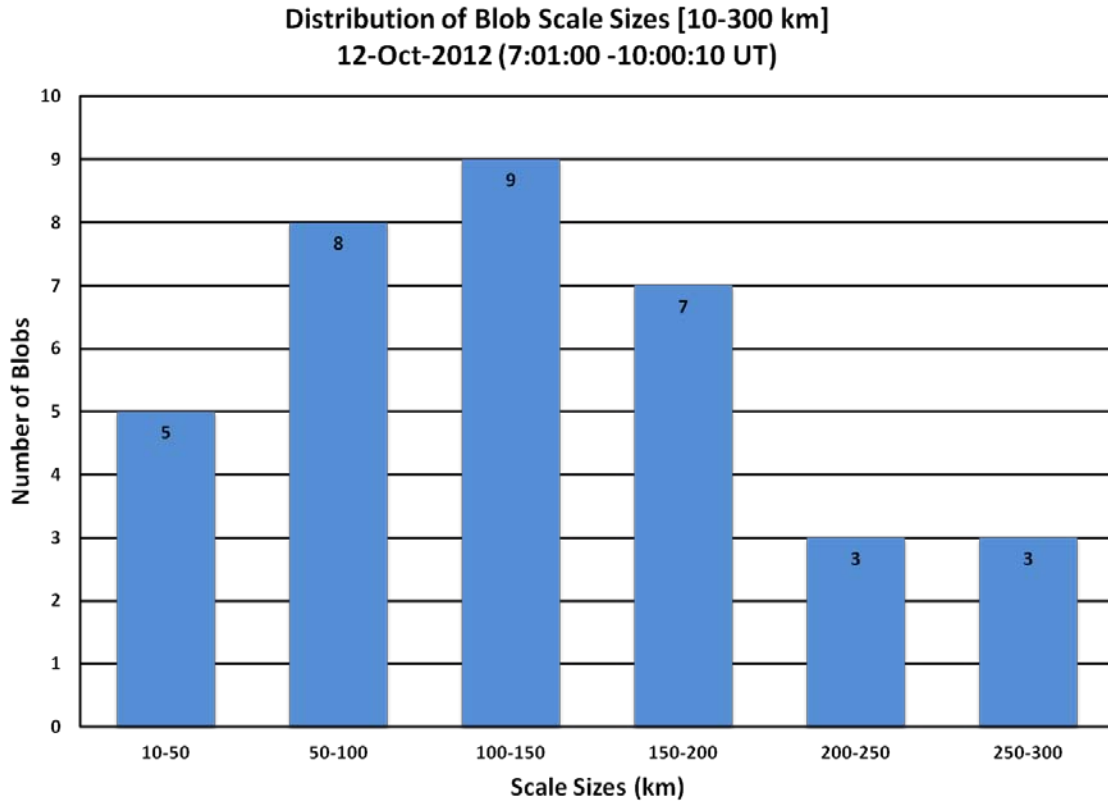


**Figure 4.15:** Magnetometer data from Poker Flat and Ft Yukon on 12 October 2012.



**Figure 4.16:** Magnetometer data and PFISR results for the night of 12 October 2012 from 07-10 UT.

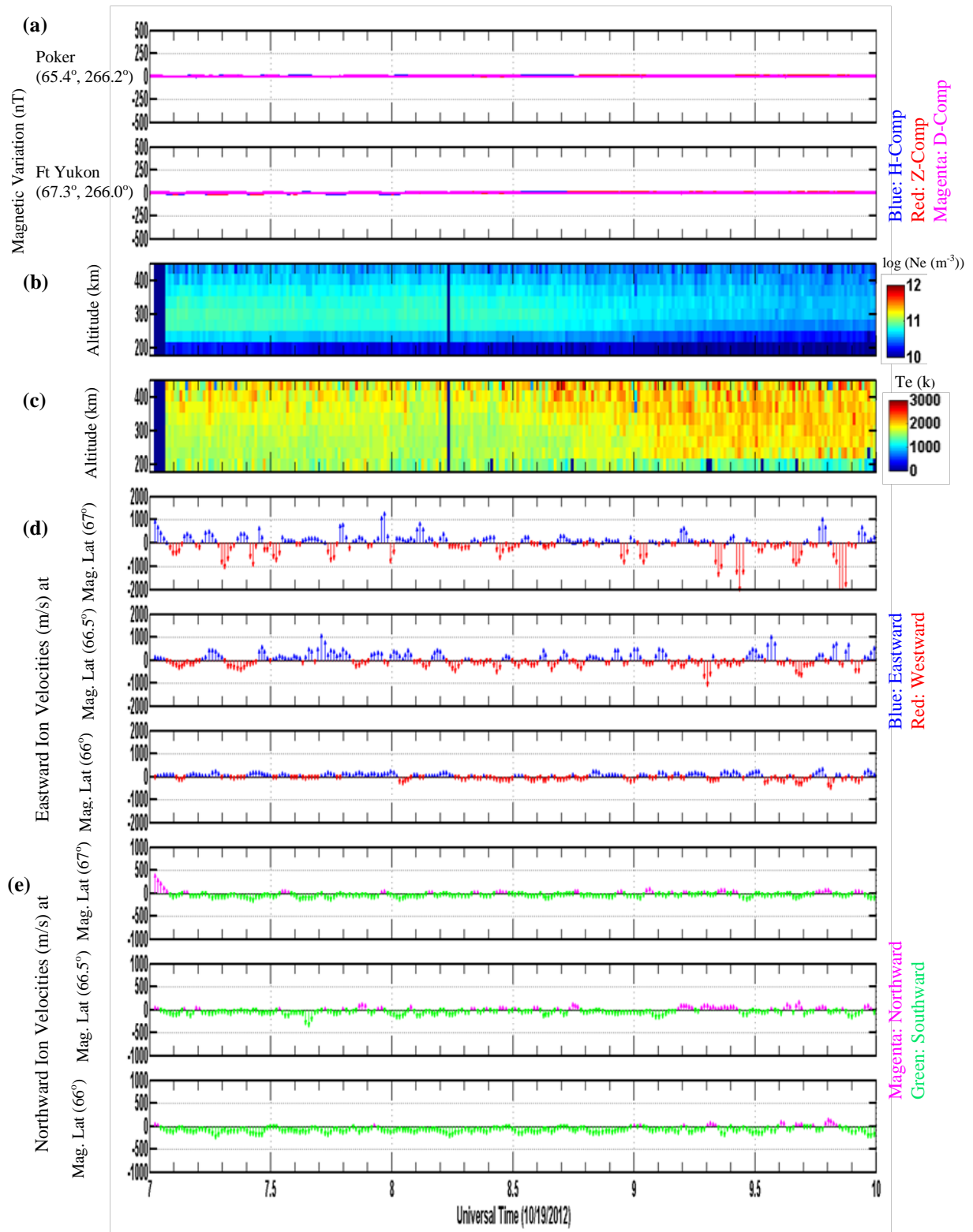




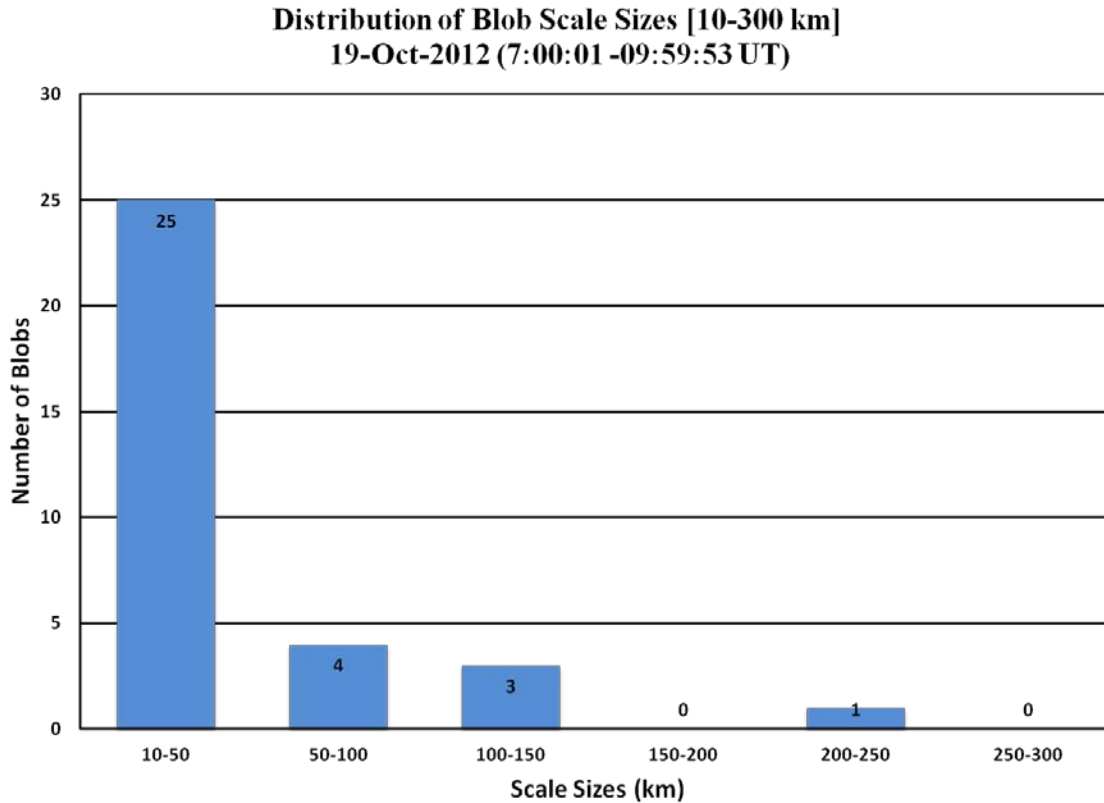
**Figure 4.17:** Bar graph of blob occurrence as a function of scale sizes on 12 October 2012.

#### **4.2.7. October 19<sup>th</sup>, 2012**

Figure 4.18 shows the observations from PFISR and Alaskan magnetometers from 07-10 UT on 19 October 2012. As shown in Figure 4.18a, there is no indication of magnetic perturbations at either of the stations. From the ionization profile, it can be clearly seen that the electron density during this night is very low with some less intense structures during the first hour of observation. Since the electron density is very low, electron temperature measurements have measurement uncertainties; otherwise there is no variation in electron temperature. Near zero east-west plasma flow with an average velocity of  $\sim 383$  m/s and southward plasma flow with an average velocity of  $\sim 51$  m/s can be observed from magnetic latitude  $66^{\circ}$ - $66.75^{\circ}$ . Figure 4.19 clearly shows that the occurrence of ionization blobs with scale sizes ranging from 10-50 km is high during this night.



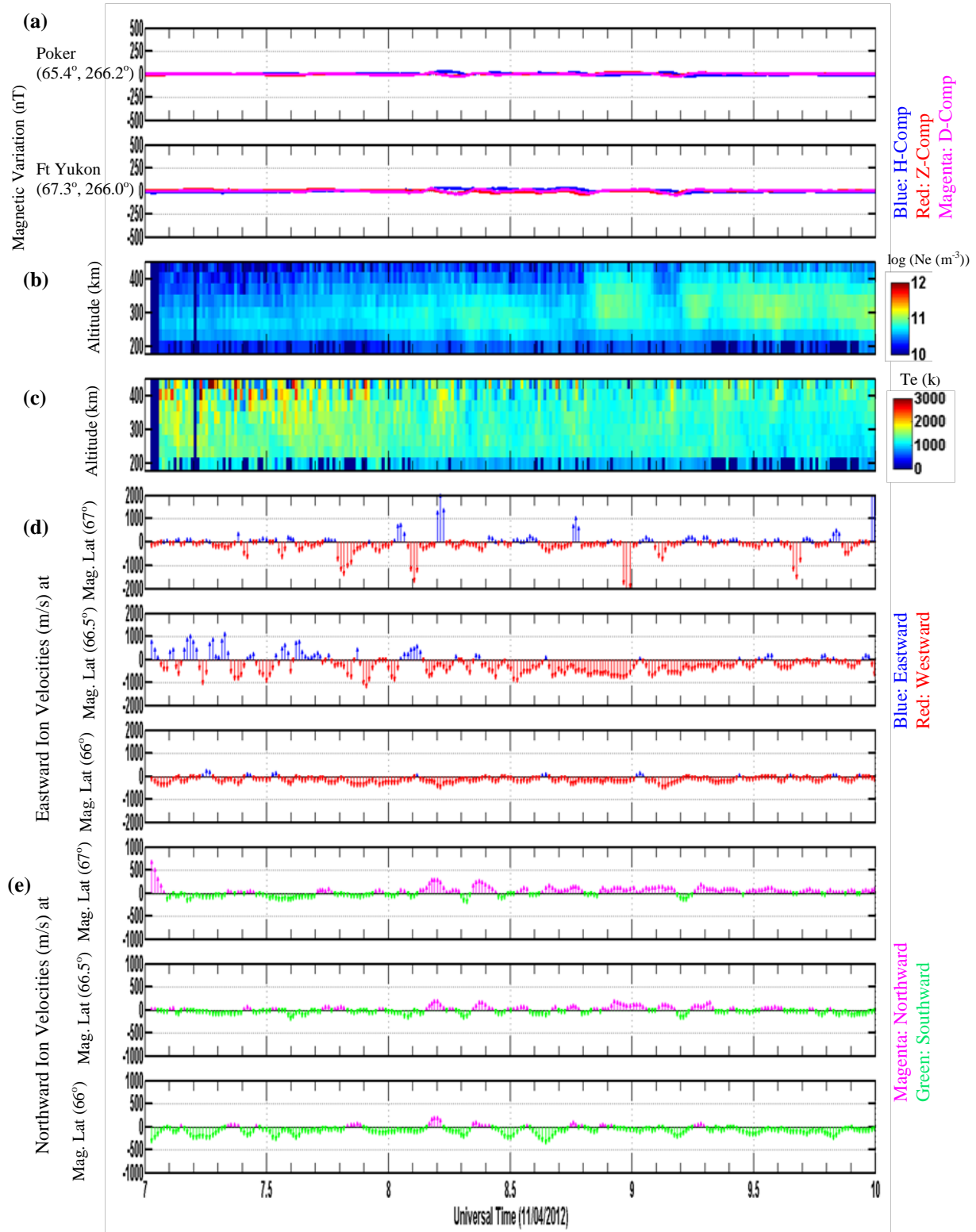
**Figure 4.18:** Magnetometer data and PFISR results for the night of 19 October 2012 from 07-10 UT.



**Figure 4.19:** Bar graph of blob occurrence as a function of scale sizes on 19 October 2012.

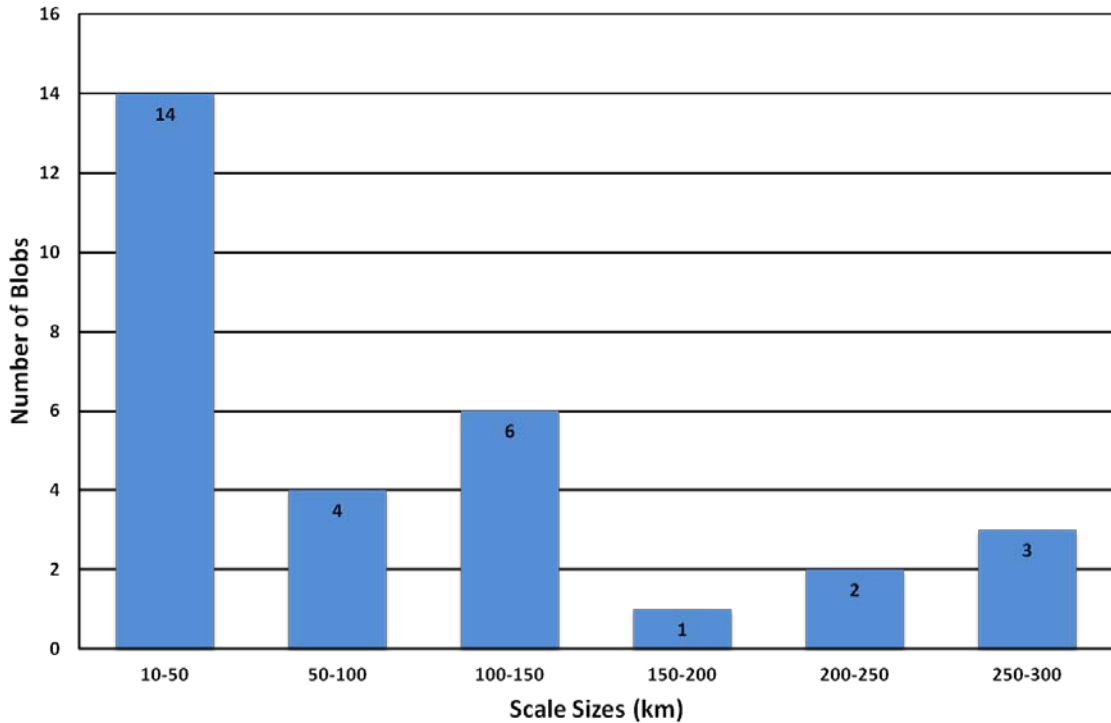
#### 4.2.8. November 4<sup>th</sup>, 2012

Figure 4.20 shows the observations from PFISR and Alaskan magnetometers from 07-10 UT on 4 November 2012. As shown in Figure 4.20a, there is no indication of magnetic perturbations at these stations during the period of observation. Ionization profile data show the presence of density structures from 8:30-10:00 UT with no corresponding increase in electron temperature; this suggests that the enhanced elongated structures are not formed locally and have convected horizontally into the radar field of view. Westward plasma flows with an average velocity of  $\sim 468$  m/s and near zero north-south plasma flows with an average velocity of  $\sim 80$  m/s can be observed from magnetic latitude  $66^\circ$ - $66.75^\circ$ . Figure 4.21 clearly shows that the occurrence of blobs with scale sizes ranging from 10-50 km is high along with the occurrence of blobs with sizes from 50-150 km during this night.



**Figure 4.20:** Magnetometer and PFISR data for the night of 04 November 2012 from 07-10 UT.

**Distribution of Blob Scale Sizes [10-300 km]**  
**04-Nov-2012 (7:01:19 -09:59:59 UT)**



**Figure 4.21:** Bar graph of blob occurrence as a function of scale sizes on 04 November 2012.

The following is a summary of the data from the remaining nights for which the data is not shown.

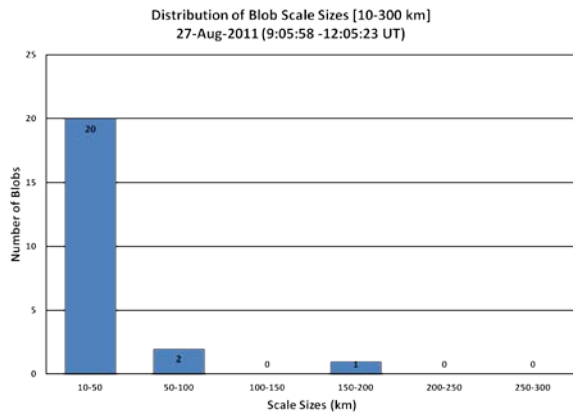
**Aug. 27, 2011:** Very quiet magnetic conditions are observed at both the stations. The ionization profile showed some small-scale structures during the period of observation. Near-zero east-west plasma flow with an average velocity of  $\sim 330$  m/s and southward plasma flow with an average velocity of 59 m/s were observed from magnetic latitude  $66^\circ$ - $66.75^\circ$ . Ionization blobs with scale sizes 10-50 km are present during the period of observation as shown in figure 4.22a.

**Aug. 29, 2011:** Active magnetic conditions are observed at both the stations. Electron density profile and electron temperature plots showed continuous structures of enhanced temperatures. The radar-measured eastward ion velocity component is directed eastward with an average velocity of 450 m/s and the northward ion velocity component is directed southward with an average velocity of 50 m/s. Ionization blobs with horizontal scale sizes of 50-200 km are dominant during this night as shown in figure 4.22(b).

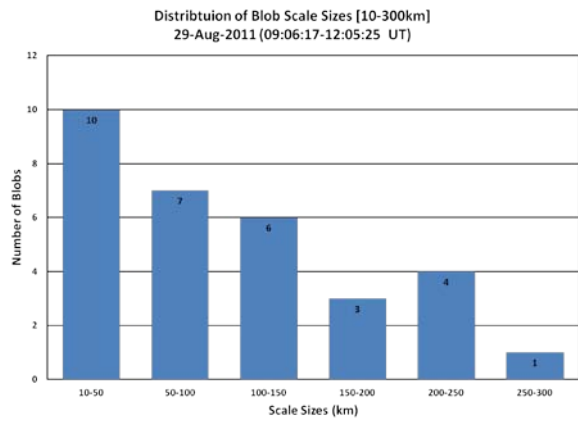
**Aug. 30, 2011:** Slightly active conditions with an onset of westward current near overhead of Ft Yukon at ~11:30 UT were observed from the magnetometer data. Electron density and electron temperature profiles indicate the presence of non-locally formed continuous enhanced structures (i.e., convected structures). Westward plasma with an average velocity of 336 m/s and northward plasma flow with an average velocity of 54 m/s were observed. Ionization blobs with scale sizes 10-150 km were observed during this night as shown in figure 4.22(c).

**Mar. 26, 2012:** Slightly active conditions are observed at both the stations. There is an onset of westward current to the north of Ft Yukon at ~10 UT. Electron density data showed the presence of locally-formed electron density structures along with convected structures. After the substorm onset, the east-west plasma flow is directed eastward with an average velocity of 800 m/s. Ionization blobs with scale sizes 10-100 km are dominant during this night as shown in figure 4.22(d). From the figure, it can be observed that there are some structures with scale size ranging from 150-250 km.

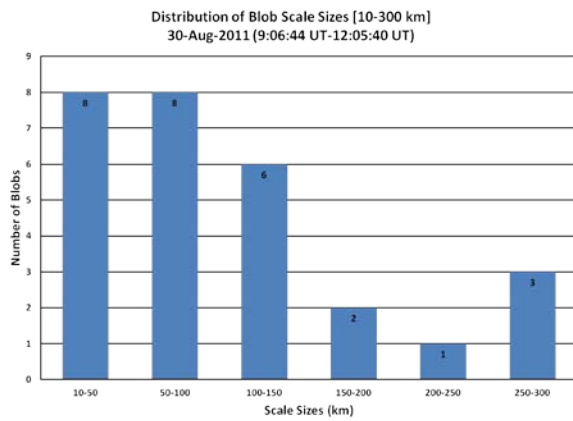
**Jan. 15, 2013:** Very slight active conditions are observed at both the stations. The electron density profile and the electron temperature profile indicate the presence of locally-formed and convected structures. Westward plasma flow with an average velocity of 464 m/s and southward plasma flow with an average velocity of 90 m/s were observed. Ionization blobs with scale sizes 10-150 km were high during this night as shown in figure 4.22(e).



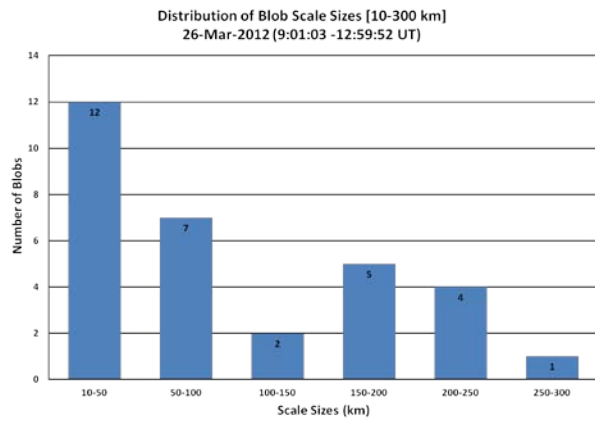
(a)



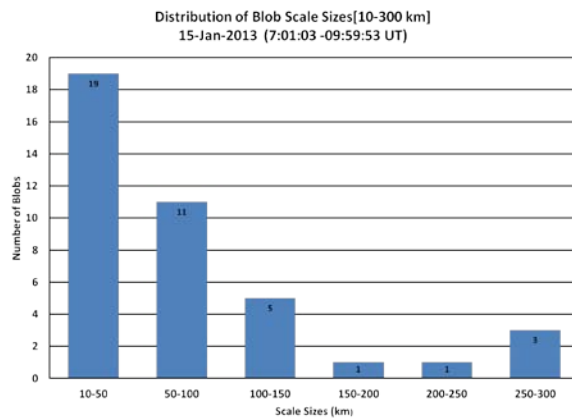
(b)



(c)



(d)



(e)

**Figure 4.22:** Bar graph of blob occurrence as a function of scale sizes on (a) 27 August 2011 (b) 29 August 2011 (c) 30 August 2011 (d) 26 March 2012 (e) 15 January 2013

### 4.3. Discussion

These observations of F-region ionosphere electron density structures using the data from Poker Flat incoherent-scatter radar have provided valuable insights of horizontal structure sizes and convection of auroral zone ionization blobs. Under southward IMF conditions, polar cap patches [high density plasma structures with scale sizes of 100-1000 km] that are formed on the day-side of the earth by solar radiation or energetic particle precipitation in the cusp region move anti-sunward across the polar cap with the ExB drift velocity from noon to midnight as shown in Figure 4.23a. As F-region plasma has a long (30-60 minute) chemical recombination time, polar cap patches then convect into the night-side auroral zone, forming east-west elongated structures known as ionization blobs with varying scale sizes. Particle precipitation in the polar cap or high latitude region may also produce blobs in the evening auroral zone. These convected blobs are often termed cold plasma irregularities as they are not associated with an increase of electron temperature. A density enhancement produced locally by soft-particle precipitation associated with an increase of electron temperature will also result in the formation of a blob in the auroral zone. Both mechanisms together will also contribute to the formation of the density increases as seen in our foregoing analysis. Under northward IMF conditions, i.e. when the magnetic conditions are quiet the plasma flow is restricted to higher latitudes, patches do not occur in the polar cap ionosphere. Instead, sun-aligned arcs or theta auroras with dawn-dusk are observed as shown in Figure 4.23b.

Ionization blobs are large-scale irregularity structures with 10-300 km sizes moving with the background plasma in the auroral zone. The high-latitude plasma flow plays a very important role in the history of the blob regardless of the source mechanism. Detailed space-time variation studies of electric fields using Poker Flat incoherent scatter radar [Watkins et al., 2011; Gudivada and Watkins, 2011, 2012] has shown the behavior of plasma flow during active geomagnetic conditions. All the cases studied using radar-derived plasma drift data during early evening hours (from 6-13 UT) when substorms occur over or near Alaska show a consistent trend as shown in the Figure 4.24.

This trend was observed at all the latitudes (from magnetic latitude  $66^{\circ}$ - $68^{\circ}$  in 0.25 degree steps) with some temporal variations depending on the current location. The east-west component of plasma flow is larger than the north-south component of plasma flow. During early evening hours in the vicinity of the westward substorm current, the east-west component of



plasma flow is negative, indicating westward plasma flow (i.e. northward E-field). Increase in westward plasma flow or near-zero east-west plasma flow was observed during the substorm growth phase (about 45-90 minutes before the substorm onset), depending on the intensity of substorm activity. At the onset of the substorm, westward plasma flow turns eastward and remains eastward. A few cases with two substorm onsets within a gap of 2-3 three hours indicated that the eastward plasma goes westward after the recovery phase of the first substorm. Following this, westward plasma flow goes eastward at the onset of second substorm and remains eastward. This behavior can be clearly observed during the night of 9<sup>th</sup> October 2012. The north-south component of plasma flow has near-zero values in the evening prior to substorm growth, indicating that there is no north-south plasma drift. During the substorm growth phase, there is westward E-field component corresponding to southward plasma motion. After the substorm onset, the westward E-field component remains, indicating continued southward plasma flow.

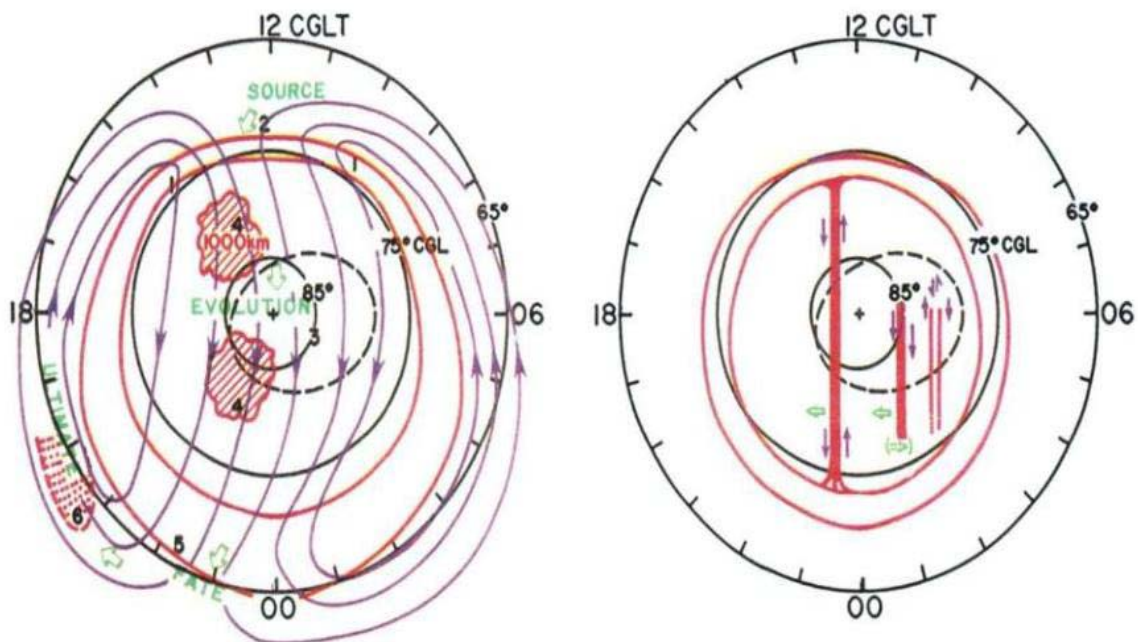


**Figure 4.23:** Irregular structures in the polar cap ionosphere (a) Patches drifting anti-sunward during Southward IMF state (b) Sun-aligned arcs or theta auroras with Dawn-Dusk drift observed during Northward IMF state [After Carlson 1994].

The foregoing analysis of plasma flow on fifteen different nights for 3-4 hour periods during the early evening and midnight time sector using 4-position high resolution mode showed similar behavior. The only difference is that the plasma flows from magnetic latitude  $66^{\circ}$ - $66.75^{\circ}$  are observed as the latitudinal range extent of this mode is limited and the data from higher latitudes has high measurements uncertainty error.

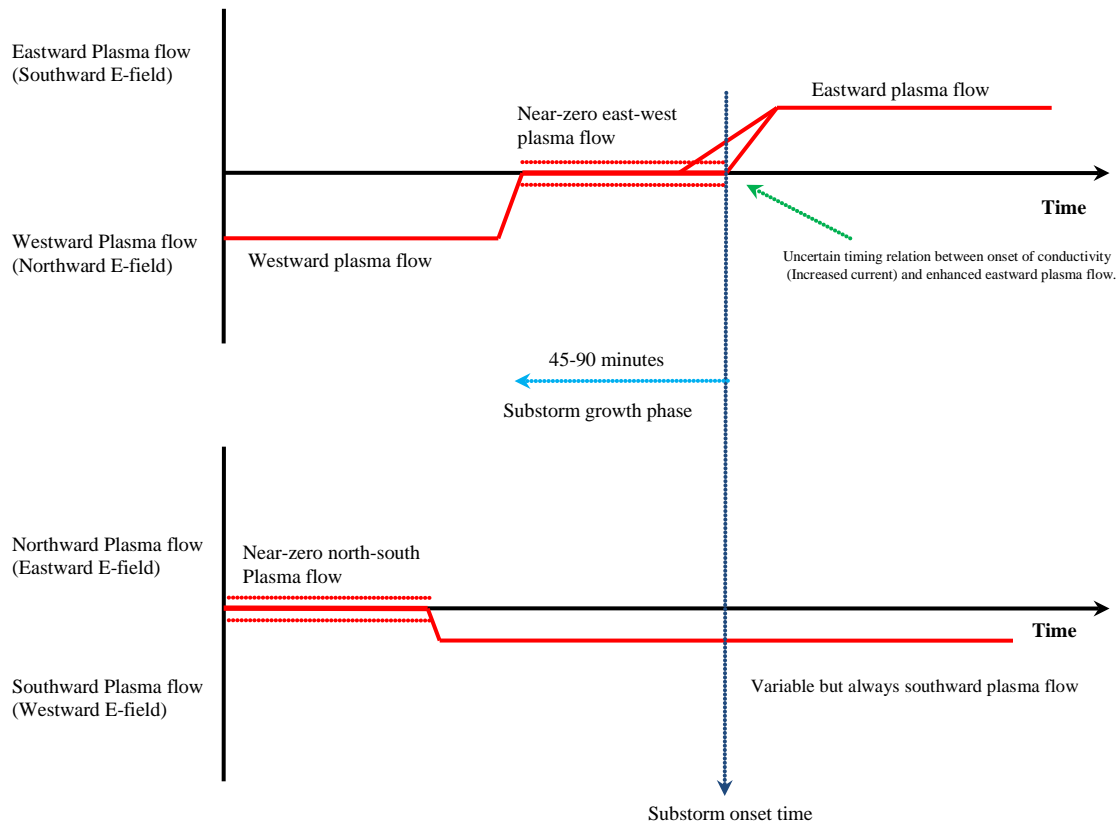


**Figure 4.24:** Consistent trend of plasma flow observed from numerous case studies using Poker Flat incoherent scatter radar.



## CHAPTER 5. CONCLUSIONS AND FUTURE WORK

### 5.1. Conclusions

In this thesis, we utilized the newly available Advanced Modular Incoherent Scatter Radar (AMISR) at Poker Flat, Alaska to measure the scale sizes of F-region electron density structures during night time. This work presents the first analysis of the horizontal structure and convection of ionization blobs in the evening auroral zone. Since incoherent-scatter radar systems are costly to operate and as the demand for the radar operation during specific time periods is high, the amount of data collected using the high-resolution mode was limited. However, there are a number of excellent case studies that have been analyzed and presented here. The observations were made from years 2011 to 2013 under varying conditions of geomagnetic activity and at different times in the evening and around the midnight time sector. From our study, we are able to conclude that:

1. For quiet geomagnetic conditions ( $K_p \leq 1$ ), near-zero east-west plasma flows with an average velocity of 100-500 m/s and southward plasma flow with an average velocity of up to 100 m/s were observed. The size distribution of ionization blobs maximizes in the range of 10-50 km.
2. These structures, during quiet conditions measured well south of the auroral oval, probably represent typical mid-latitude conditions.
3. For active geomagnetic conditions ( $K_p \geq 4$ ), the drift of the ionization blobs depends on the onset of the westward current and the distribution of scale sizes is shifted to 100-300 km. The radar-measured ion velocity component is directed westward with an average velocity of 500-1000 m/s before the substorm onset and it is directed eastward with an average velocity of 500-1000 m/s after the substorm onset. Southward plasma flow with a velocity of up to 400 m/s was observed.
4. This shift of distribution from smaller sizes (10-50 km) to larger scale sizes (100-300 km) during active conditions ( $K_p \geq 4$ ) is related to the relative location of the observations to the strong auroral east-west plasma velocities just equatorward of the auroral oval.
5. For the observations in the region of large east-west plasma velocities, due to long chemical recombination times these structures are convected horizontally into the observation regions from their origin in the polar cap and dayside ionosphere.

## 5.2. Future Work

Much work remains to be done in this area. Observations presented here were limited by a restricted data base, as the radar was operated in a special mode for limited time intervals. In order to make more generalized statements about the distribution of the scale sizes of electron density irregularities more data is required. By carrying out the observations throughout the year, the variations could be ascribed to the changing season or the time of day. The Poker Flat Incoherent Scatter Radar is operated continuously on a low-duty cycle throughout the year with a beam configuration similar to the mode used in this thesis. Figure 5.1a shows the geometry plot of the azimuthal and the elevation of the beams. Figure 5.1b shows the line plot of the range coverage of the beams. This mode, named IPY (long-duration measurements in support of the International Polar Year) transmits both long-pulse and a shorter alternating code. This data has poor-time resolution compared to the data used in this thesis because of the transmission of alternating code pulses that are usually not useful for F-region studies. Similar technique could be used to study the diurnal and seasonal variations of electron density irregularity scale sizes by sacrificing the time resolution.

Other experiments that could be performed include simultaneous optical and radar experiments to examine if there is any difference between the scale sizes of electron density irregularities measured using both techniques.

Work relating polar cap patches and auroral zone blobs hasn't been done. Simultaneous observations in the polar cap and auroral zone would be invaluable in this regard. The northward looking Resolute Bay Incoherent Scatter Radar (RISR-N) is shown in figure 5.2. RISR-N is located at Cornwallis Island, Nunavut, Canada, geographic latitude  $74.72^{\circ}$  N and longitude  $94.90^{\circ}$  W. The face of the radar is tilted in such a way that its bore-sight direction corresponds to an azimuthal angle (east of north) of  $26^{\circ}$  and an elevation angle of  $74^{\circ}$ . The radar operating frequency is  $\sim 442.5$  MHz and operates at an output power of 2 MW. This radar is located in the polar cap, making it suitable for the observation of polar cap ionization patches. Simultaneous observations of polar cap patches using RISR-N and auroral zone ionization blobs using PFISR might provide valuable insights into electron density irregularities relating to their formation and transport from the polar cap to the auroral zone.

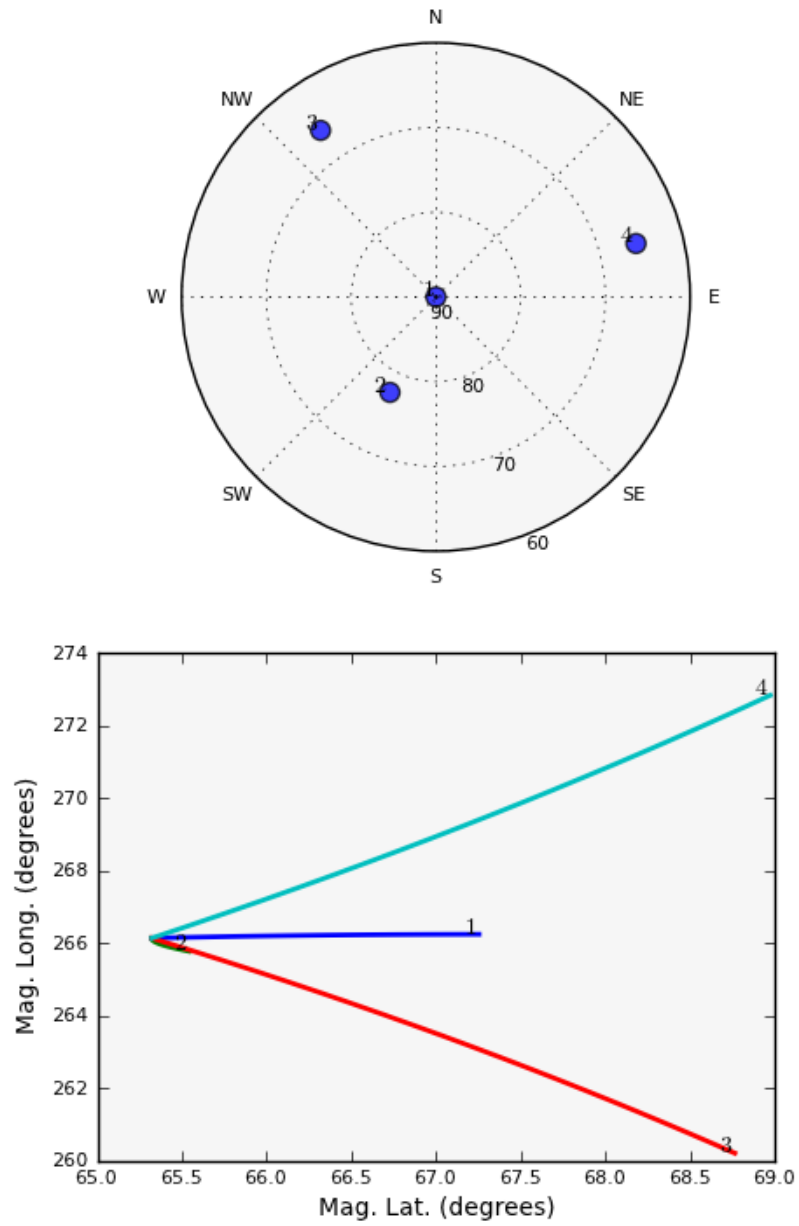


**Figure 5.1:** (a) Geometry plot of the azimuthal and elevation angles of the beams. (b) Range coverage of the beams as a function of magnetic longitude and magnetic latitude.



**Figure 5.2:** Northward looking UHF phased array radar at Resolute Bay, on Cornwallis Island, Canada.

## References

- Aarons, J., (1982), Global morphology of ionospheric scintillations, Proceedings of the IEEE, 70(2), 360-378.
- Aarons, J., H. M. Silverman, and B. A. Ramsey (1966), Latitudinal effects on satellite scintillations, Ann. Geophys., 22, 349-355.
- Aarons, J., H. S. Whitney, and R. S. Allen (1971), Global Morphology of Ionospheric Scintillation, Proc IEEE, 59, 159-172.
- Aarons, J., J. P. Mullen, and H. E. Whitney (1969), The Scintillation Boundary, J. Geophys. Res., 74(3), 884-889.
- Anderson, D. N., J. Buchau, and R. A. Heelis (1988), Origin of density enhancements in the winter polar cap ionosphere, Radio Sci., 23(4), 513-519.
- Appleton, E. V., and M. A. F. Barnett (1925a), On Some Direct Evidence for Downward Atmospheric Reflection of Electric Rays, Proceedings of the Royal Society of London, Series A, Containing Papers of a Mathematical and Physical Character, 109(752), 621-641.
- Appleton, E. V., and M. A. F. Barnett (1925b), Local Reflection of Wireless Waves from the Upper Atmosphere, Nature, 115, 333-334.
- Axford, W. I., and C. O. Hines (1961), A unifying theory of high latitude geophysical phenomena and geomagnetic storms, Can. J. Phys., 39, 1433-1464.
- Bacquerel, H., (1897), Sur une interprétation applicable au phénomène de Faraday et au phénomène de Zeeman, C. R. Acad. Sci., 125, 679-685.
- Bandyopadhyay, P., and J. Aarons (1970), The equatorial F layer irregularity extent as observed from Huancayo, Peru, Radio Sci., 5, 931-938.
- Banks, P. M., C. L. Rino, and V. B. Wickwar (1974), Incoherent scatter radar observations of westward electric fields and plasma densities in the auroral ionosphere, 1, J. Geophys. Res., 79(1), 187-198.



- Basu, S., R. S. Allen, and J. Aarons (1964), A detailed study of a brief period of radio star and satellite scintillations, *Journal of Atmospheric and Terrestrial Physics*, 26(8), 811-823.
- Basu, S., J. P. McClure, S. Basu, W. B. Hanson, and J., Aarons (1980), Coordinated study of equatorial scintillation and in-situ and radar observations of nighttime F- region irregularities, *Journal of Geophys. Res.*, 85, 5119-5130.
- Behnke, R. A., (1971), Vector measurements of the ion transport velocity with applications to F-region dynamics, Ph.D. thesis, Rice University, Houston, Texas.
- Bekefi, G., (1966), *Radiation processes in plasmas*, John Wiley and Sons, Inc.
- Bolton, J. G., and G. J. Stanley (1947), Variable source of Radio Frequency Radiation in the Constellation of Cygnus, *Nature*, 161, 312-313.
- Bolton, J. G., O. B. Slee, and G. J. Stanley (1953), Galactic radiation at Radio Frequencies. VI. Low Altitude Scintillations of the Discrete Sources, *Austr. J. Phys.*, 6, 434-451.
- Booker, H. G., J. A. Ratcliffe, and D. H. Shinn (1950), Diffraction from an Irregular Screen with Application to Ionospheric Problems, *Phil. Tran. Roy. Soc. Lond. A*, 242(856), 579-607.
- Booker, H. G., (1958), The Use of Radio Stars to Study Irregular Refraction of Radio Waves in the Ionosphere, *Proceedings of the IRE* , 46(1), pp.298-314.
- Bowles, K. L., (1958), Observations of vertical-incidence scatter from the ionosphere at 41 Mc/sec, *Phys. Rev. Letters*, 1, 454-455.
- Bowles, K. L., (1959), National Bureau of Standards Report 6070, Boulder Colorado.
- Breit, G., and M. A. Tuve (1926), A Test of the Existence of the Conducting Layer, *Physical Review*, 28 (3), 554-575.
- Brekke, A., (1977), *Radar Probing of the Auroral Plasma: EISCAT Summer School Proceedings*, Scandinavian university books.

- Briggs, B. H., (1958), A study of the ionospheric irregularities which cause spread-F echoes and scintillations of radio stars, *Journal of Atmosphere and Terrestrial Physics*, 12(1), 34-45.
- Browne, I. C., et al. (1956), Radio echoes from the Moon, *Proc. Phys. Soc. London Sect. B*, 69, 901-920.
- Buchau, J., B. W. Reinisch, E. J. Weber, and J. G. Moore (1983), Structure and dynamics of the winter polar cap F region, *Radio Sci.*, 18, 995-1010.
- Buckley, M.J., (1994), Fast computation of a discretized thin-plate smoothing spline for image data, *Biometrika*, 81, 247-258
- Buneman, O., (1962), Scattering of radiation by the fluctuations in a nonequilibrium plasma, *J. Geophys. Res.*, 67, 2050-2053.
- Burns, C. J., and J. K. Hargreaves (1996), The occurrence and properties of large-scale electron-density structures in the auroral F region. *Journal of Atmospheric and Terrestrial Physics*, 58, 217-232.
- Carlson, H. C., (1994), The dark polar ionosphere: Progress and future challenges, *Radio Sci.*, 29(1), 157-165.
- Carlson, H. C., (2012), Sharpening our Thinking about Polar Cap Ionospheric Patch Morphology, *Research and Mitigation Techniques*, *Radio Sci.*, 47.
- Carru, H., M. Petit, and P. Waldteufel (1967a), Mis en évidence de mouvements dans l'ionosphère au moyen de la diffusion incohérente, *C. R. Acad. Sci. Paris*, 264, 560-563.
- Carru, H., M. Petit, G. Vasseur, and P. Waldteufel (1967b), Résultats ionosphériques obtenus par diffusion de Thomson, 1966-1967, *Ann. Geophys.*, 23, 455-465.
- Cotton, A., and H. Mouton (1907), Nouvelle propriété optique de certains liquids organiques non colloïdaux, *C. R. Acad. Sci.*, 145, 229-230.
- Craven, P., and G. Wahba (1978), Estimating the correct degree of smoothing by the method of generalized cross-validation, *Numerische Mathematik*, 31, 377-403.

- Davies, K., (1989), *Ionospheric Radio*, Peter Peregrinus, London, 8.3, 273-277.
- Davies, K., R. B. Fritz, R. N. Grubb, and J. E. Jones (1975), Some early results from the ATS-6 Radio Beacon Experiment, *Radio Sci.*, 10(8, 9), 785-799.
- De la Beaujardière, O., et al. (1985), Universal time dependence of nighttime F-region densities at high latitudes, *J. Geophys. Res.*, 90(A5), 4319-4332.
- De la Beaujardière, O., R. Vondrak and M. Baron (1977), Radar observations of electric fields and currents associated with auroral arcs, *J. Geophys. Res.*, 82(32), 5051-5062.
- Dougherty, J. P., and D. T. Farley (1960), A theory of incoherent scattering of radio waves by a plasma, *Proc. Roy. Soc.*, A259, 79-99.
- Dougherty, J. P., and D. T. Farley (1963), A theory of incoherent scattering of radio waves by a plasma, 3. Scattering in a partly ionized gas, *J. Geophys. Res.*, 68, 5473-5486.
- Douppnik, J. R., P. M. Banks, M. J. Baron, C. L. Rino, and J. Petriceks (1972), Direct measurements of plasma drift velocities at high magnetic latitudes, *J. Geophys. Res.*, 77(22), 4268-4271.
- Dungey, J. W., (1961), Interplanetary Magnetic field and auroral zones, *Phys. Rev. Letts.*, 6, 47-48.
- Evans, J. V., (1972), The upper atmosphere observatory, *Science*, 176, 463-473.
- Evans, J. V., R. A. Brockelman, R. F. Julian, W. A. Reid, and L. A. Carpenter (1970), Determination of F-region Vertical Drifts at Millstone Hill, *Radio Sci.*, 5(1), 27-38.
- Evans, J. V., (1969), Theory and practice of ionosphere study by Thomson scatter radar, *Proceedings of the IEEE*, 57(4), 496-530.
- Faraday, M., (1846), On the magnetization of light and the illumination of magnetic lines of force, *Trans. R. Soc. London*, 136, 1-62.

- Farley, D. T., (1969a), Incoherent-Scatter Power Measurements; a Comparison of Various Techniques, *Radio Sci.*, 4(2), 139-142.
- Farley, D. T., (1969b), Faraday rotation Measurements Using Incoherent Scatter, *Radio Sci.*, 4, 143-152.
- Farley, D. T., (1969c), Incoherent-Scatter Correlation Function Measurements, *Radio Sci.*, 4(10), 935-953.
- Farley, D. T., (1971), Radio wave scattering from the ionosphere, ch.14 in *Methods of Experimental Physics*, R. H. Lovberg, and H. R. Griem, eds., 9B, 139-186.
- Farley, D. T., (1972), Multiple-pulse incoherent-scatter correlation function measurements, *Radio Science*, 7(6), 661- 666.
- Farley, D. T., (1966), A theory of incoherent scattering of radio waves by a plasma, 4, The effect of unequal ion and electron temperatures, *J. Geophys. Res.*, 63, 79-99.
- Farley, D. T., J. P. Dougherty, and D. W. Barron, (1961), A theory of incoherent scattering of radio waves by a plasma, 2, Scattering in a magnetic field, *Proc. Roy. Soc.*, A263, 238-258.
- Fejer, J. A., (1960a), Scattering of radio waves by an ionized gas in thermal equilibrium, *Can. J. Phys.*, 38, 1114-1133.
- Fejer, J. A., (1960b), Radio-wave scattering by an ionized gas in thermal equilibrium, *J. Geophys. Res.*, 65, 2635–2636.
- Foster, J. C., (1984), Ionospheric signatures of magnetospheric convection, *J. Geophys. Res.*, 89, 855–865.
- Foster, J. C., (1989), Plasma transport through the dayside cleft: A source of ionization patches in the polar cap, in *Electromagnetic Coupling in the Polar Clefts and Caps*, Kluwer Acad., Norwell, Mass, 343-354.
- Foster, J. C., and J. R. Doupnik (1984), Plasma convection in the vicinity of the dayside cleft, *J. Geophys. Res.*, 89, 9107-9113.

- Foster, J. C., et al. (2005), Multiradar observations of the polar tongue of ionization, *J. Geophys. Res.*, 110, A09S31.
- Foster, J. C., J. M. Holt, J. D. Kelley, and V. B. Wickwar (1985), High resolution observations of electric fields and F-region plasma parameters in the cleft ionosphere, *The Polar Cusp*, 349-364.
- Frihagen, J., and L. Liszka (1965), A study of auroral zone ionospheric irregularities made simultaneously at Tromso, Norway, and Kiruna, Sweden, *J. Atmospheric Terrestrial Phys.*, 27, 513.
- Garcia, D., (2009), Robust smoothing of gridded data in one and higher dimensions with missing values, *Computational Statistics & Data Analysis*, 54, 1167-1178.
- Gordon, W. E., (1958), Incoherent scattering of radio waves by free electrons with applications to space exploration by radar, *Proc. IRE*, 46, 1824-1829.
- Gray, R. W., and D. T. Farley (1973), Theory of incoherent-scatter measurements using compressed pulses, *Radio Sci.*, 8(2), 123-131.
- Gudivada, K. P., and B. J. Watkins (2011), Variations of Substorm Electric-field Components Measured with the Poker-Flat Incoherent-Scatter Radar, AGU 2011 Fall Meeting, abstract # SA41B-1852, San Francisco, California, USA, 2011.
- Gudivada, K. P., and B. J. Watkins, Electric Field and Conductivity Variations Near Substorm Onset Times , UNSC-URSI National Radio Science Meeting 2012, Boulder, Colorado, USA 2012.
- Hagen, J. B., and D. T. Farley (1973), Digital-correlation techniques in radio science, *Radio sci.*, 8(8), 775-784.
- Hagfors, T., (1961), Density fluctuations in a plasma in a magnetic field, with application to the ionosphere, *J. Geophys. Res.*, 66(6), 1699-1712.
- Hagfors, T., and R. A. Behnke (1974), Measurement of three-dimensional plasma velocities at the Arecibo Observatory, *Radio Sci.*, 9(2), 89-93.

- Hargreaves, J. K., (1970), ATS-F: Observational opportunities, in Proceedings of the Symposium on the Future Application of Satellite Beacon Experiments, 16, 1-9.
- Hargreaves, J. K., and B. K. Holman (1972), Computed effects of the ionosphere/proton sphere distribution on VHF signals from ATS-F/G in Proceedings of the Symposium on the Future Application of Satellite Beacon Measurements, 129-138.
- Hargreaves, J. K., and C. J. Burns (1988), Electron density and electron content fluctuations in the auroral zone, *Radio Sci.*, 23(4), 493-502.
- Hargreaves, J. K., C. J. Burns, and S. C. Kirkwood (1985), EISCAT studies of F-region irregularities using beam scanning, *Radio Sci.*, 20(4), 745-754.
- Harper, R. M., (1971), Dynamics of the neutral atmosphere in the 200-500 km height region at low latitudes, Ph.D. thesis, Rice University, Houston, Texas.
- Heelis, R. A., (1984), The effects of interplanetary magnetic field orientation on dayside high-latitude ionospheric convection, *J. Geophys. Res.*, 89, 2873-2880.
- Heelis, R. A., J. K. Lowell, and R. W. Spiro (1982), A model of the high-latitude ionospheric convection pattern, *J. Geophys. Res.*, 87, 6339-6345.
- Heinselman, C. J., (1999), Auroral effects on meteoric metals in the upper atmosphere, Ph.D. thesis, Dept. of Electrical Engineering, Stanford University, Stanford, California.
- Heinselman, C. J., and M. J. Nicolls (2008), A Bayesian approach to electric field and E-region neutral wind estimation with the Poker Flat Advanced Modular Incoherent Scatter Radar, *Radio Science*, 43, RS5013.
- Heppner, J. P., (1972), Polar-cap electric field distributions related to the interplanetary magnetic field direction, *J. Geophys. Res.*, 77(25), 4877-4887.
- Heppner, J. P., and N. C. Maynard (1987), Empirical high-latitude electric field models, *J. Geophys. Res.*, 92, 4467-4489.
- Heppner, J. P., (1973), High-latitude electric fields and the modulations related to interplanetary magnetic field parameters, *Radio Sci.*, 8, 933-948.

- Heppner, J. P., (1977), Empirical models of high-latitude electric fields, *J. Geophys. Res.*, 82, 1115-1125.
- Hewish, A., (1952), The Diffraction of Galactic Radio Waves as a Method of Investigating the Irregular Structure of the Ionosphere, *Proceedings of the Royal Society*, 214, 494-514.
- Hey, J. S., S. J. Parsons and J. W. Phillips (1946), Fluctuations in Cosmic Radiation at Radio frequencies, *Nature*, 158, 234.
- Holt, J. M., D. A. Rhoda, D. Tetenbaum, and A.P. Van Eyken (1992), Optimal analysis of incoherent scatter radar data, *Radio Sci.*, 27(3), 435-447.
- Hunsucker, R. D., and J. K. Hargreaves (2003), *The high-latitude ionosphere and its effects on radio propagation*, Cambridge University Press.
- Huuskonen, A., and T. Turunen (1990), Observations of D- and E-region stratifications with incoherent scatter radar, *Advances in Space Research*, 10, 93-100.
- Huuskonen, A., et al. (1988), Range ambiguity effects in Barker-coded multipulse experiments with incoherent scatter radars, *Journal of Atmospheric and Terrestrial Physics*, 50, 265-276.
- Ioannidis, G., and D. T. Farley (1972), Incoherent Scatter Observations at Arecibo Using Compressed Pulses, *Radio Sci.*, 7(7), 763-766.
- Ireland, W., and G. F. Preddey (1967), Regular fading of satellite transmissions, *J. Atmospheric Terrest. Phys.*, 29, 137-138.
- Kelley, M. C., et al. (1982), On the origin and spatial extent of high-latitude F-region irregularities, *J. Geophys. Res.*, 87, 4469-4475.
- Kelley, J. D., and J. F. Vickrey (1984), F-region ionospheric structure associated with antisunward flow near the dayside polar cusp, *Geophys. Res. Lett.*, 11(9), 907-910.
- Kent, G. S., (1959), High frequency fading observed on the 40 Mc/s wave radiated from artificial satellite 1957 $\alpha$ , *Journal of Atmospheric and Terrestrial Physics*, 16, 10-20.

- Kent, G. S., (1961), High frequency fading of the 108 Mc/s wave radiated from an artificial earth satellite as observed at an equatorial station, *Journal of Atmospheric and Terrestrial Physics*, 22, 255-260.
- Knudsen, W. C., P. M. Banks, J. D. Winningham, and D. M. Klumpar (1977), Numerical model of the convecting F2 ionosphere at high latitudes, *J. Geophys. Res.*, 82, 4784-4792.
- Lehtinen, M. S., (1986), Statistical theory of incoherent scatter radar measurements, Tech. Rep. 86/45, European Incoherent Scatter Science Association, Kiruna, Sweden.
- Lehtinen, M. S., and I. Häggström (1987), A new modulation principle for incoherent scatter measurements, *Radio Sci.*, 22, 625-634.
- Lehtinen, M. S., and A. Huuskonen (1996), General incoherent scatter analysis and GUIDAP, *Journal of Atmospheric Terrestrial Physics*, 58, 435-452.
- Liszka, L., (1962a), Diffraction of satellite signals by irregularities in sporadic E layers. Scientific Report No. 6, Contract No. AF 61(514)-1314.
- Liszka, L., (1962b), Auroral zone satellite scintillation studies. *Radio Astronomical and Satellite Studies of the Upper Atmosphere*. North-Holland Publ. Comp, 344.
- Liszka, L., (1963), Satellite scintillation observed in the auroral zone. *Archive for Geophysics*, 4, 211-225.
- Little, C. G., and A. C. B. Lovell (1950), Origin of the fluctuations in the intensity of radio waves from galactic sources, *Nature*, 165, 423-424.
- Maynard, N. C., J. P. Heppner, and A. Egeland (1982), Intense, variable electric fields at ionospheric altitudes in the high latitude regions as observed by DE-2, *Geophys. Res. Lett.*, 9(9), 981-984.
- McClure, J. P., (1964), The Height of Scintillation-Producing Ionospheric Irregularities in Temperate Latitudes, *J. Geophys. Res.*, 69(13), 2775-2780.



- McClure, J. P., and W. B. Hanson (1973), A catalog of ionospheric F-region irregularity behavior based on OGO-6 retarding potential analyzer data, *J. Geophys. Res.*, 78, 7431-7440.
- McEwen, D. J., and D. P. Harris (1996), Occurrence patterns of F-layer patches over the north magnetic pole, *Radio Sci.*, 31, 619-628.
- Meyer, F. J., et al. (2006), The potential of low-frequency SAR systems for mapping ionospheric TEC distributions, *Geoscience and Remote Sensing, IEEE Transactions on*, 3, 560-564.
- Meyer, F. J., (2011), Performance requirements for ionospheric correction of low-frequency SAR data, *Geoscience and Remote Sensing, IEEE Transactions on*, 49, 3694-3702.
- Milan, S. E., M. Lester, and T. K. Yeoman (2002), HF radar polar patch formation revisited: summer and winter variations in dayside plasma structuring, *Ann. Geophys.*, 20, 487-499.
- Moen, J., et al. (2006), EISCAT observations of plasma patches at sub-auroral cusp latitudes, *Ann. Geophys.*, 24, 2363-2374.
- Muldrew, D. B., and J. F. Vickrey (1982), High-latitude F-region irregularities observed simultaneously with ISIS 1 and the Chatanika radar, *J. Geophys. Res.*, 87, 8263-8272.
- Nicolls, M. J., and C. J. Heinselman, (2007), Three-dimensional measurements of traveling ionospheric disturbances with the Poker Flat Incoherent Scatter Radar, *Geophys. Res. Lett.*, 34, L21104.
- Nygren, T., (1996), Introduction to Incoherent-scatter radar measurements, INVERS Oy, Finland.
- Nygren, T., and M. Markkanen (1997), Long alternating codes, 1. Search by playing dominoes, *Radio Science*, 32, 1-8.
- Pedersen, P. O., (1927), *The Propagation of Radio Waves*, Dan. Naturvidensk. Samfund, Copenhagen, 109-111.

- Pedersen, T. R., B. G. Fejer, R. A. Doe, and E. J. Weber (1998), Incoherent scatter radar observations of horizontal F-region plasma structure over Sondrestrom, Greenland, during polar cap patch events, *Radio Sci.*, 33, 1847-1866.
- Pineo, V. C., L. G. Kraft, and H. W. Briscoe (1960), Some characteristics of ionospheric backscatter observed at 440 Mc/s, *J. Geophys. Res.*, 65, 2629-2634.
- Pryse, S. E., L. Kersley, and I. K. Walker (1996), Blobs and irregularities in the auroral ionosphere, *J. Atmos. Terr. Phys.*, 58, 205-215.
- Quegan, S., et al. (1982), A theoretical study of the distribution of Ionization in the high-latitude ionosphere and the plasma sphere: First results on the mid-latitude trough and the light-ion trough, *J. Atmos. Terr. Phys.*, 44, 619-640.
- Ratcliffe, J. A. (1951), Some regularities in the F2 region of the ionosphere, *J. Geophys. Res.*, 56(4), 487-507.
- Ratcliffe, J. A., (1954), The analysis of fading records from spaced receivers, *J. Atmos. Terr. Phys.*, 5, 173-181.
- Rino, C. L., M. J. Baron, G. H. Burch, and O. de la Beaujardiere, (1974), A multipulse correlator design for incoherent scatter radar, *Radio Sci.*, 9(12), 1117-1127
- Rino, C. L., et al. (1983), Recent studies of the structure and morphology of auroral zone F-region irregularities, *Radio Sci.*, 18(6), 1167-1180.
- Robinson, R. M., R. T. Tsunoda, J. F. Vickrey, and L. Guerin (1985), Sources of F-region ionization enhancements in the nighttime auroral zone, *J. Geophys. Res.*, 90, 7533-7546.
- Rodger, A. S., et al. (1994), A new mechanism for polar patch formation, *J. Geophys. Res.*, 99, 6425-6436.
- Rosenbluth, M., and N. Rostoker (1960), Test Particles in a Completely Ionized Plasma, *Phys. Fluids*, 3, 1.

- Rosenbluth, M., and N. Rostoker (1962), Scattering of electromagnetic waves by a nonequilibrium plasma, *Phys. Fluids*, 5, 776.
- Ryle, M., and A. Hewish (1950), The Effects of the Terrestrial Ionosphere on the Radio Waves from Discrete Sources in the Galaxy, *Monthly Notices of the Royal Astronomical Society*, 110, 384-394.
- Salpeter, E. E. (1960a), Scattering of radio waves by electrons above the ionosphere, *J. Geophys. Res.*, 65(6), 1851-1852.
- Salpeter, E. E., (1960b), Electron density fluctuations in plasma, *Phys. Rev.*, 120(5), 1528 -1535.
- Salpeter, E. E. (1961), Effect of the magnetic field in ionospheric backscatter, *J. Geophys. Res.*, 66(3), 982-984.
- Schlegel, K., and D. R. Moorcroft (1989), EISCAT as a tristatic auroral radar, *J. Geophys. Res.*, 94(A2), 1430-1438.
- Schunk, R. W., J. J. Sojka, and M. D. Bowline (1986), Theoretical study of the Electron temperature in the high-latitude ionosphere for solar maximum and winter conditions, *J. Geophys. Res.*, 91, 12,041-12,054.
- Shimazaki, T., (1959), A statistical study of world-wide occurrence probability of spread-F, *Journal of Radio Research Labs*, 6, 669-687.
- Singleton, D. G., and G. J. Lynch (1962), The Scintillations of the Radio Transmissions from Explorer 7, *JATP*, 24, 353-374.
- Smerd, S. F., and O. B. Slee (1966), Regular Variations in the scintillations of Radio sources with Season, Time of day and Solar Distance, *Australian Journal of Physics*, 19, 427-439.
- Smith, F. G., (1950), Origin of the Fluctuations in the Intensity of Radio Waves from Galactic Sources, *Nature*, 165, 422-423.
- Sojka, J. J., and R. W. Schunk (1987), Theoretical study of the high-latitude ionosphere's response to multi-cell convection patterns, *J. Geophys. Res.*, 92(A8), 8733-8744.

- Sojka, J. J., et al. (1993), Modeling polar cap F-region patches using time varying convection, *Geophys. Res. Lett.*, 20(17), 1783-1786.
- Sojka, J. J., and R. W. Schunk (1985), A theoretical study of the global F-region for June solstices, solar maximum, and low magnetic activity, *J. Geophys. Res.*, 90, 5285-5298.
- Sojka, J. J., M. D. Bowline, and R. W. Schunk (1994), Patches in the polar ionosphere: UT and seasonal dependence, *J. Geophys. Res.*, 99(A8), 14,959–14,970.
- Spiro, R. W., R. A. Heelis, and W. B. Hanson (1978), Ion convection and the formation of the mid-latitude F-region ionization trough, *J. Geophys. Res.*, 83, 4255-4264.
- Sulzer, M. P., (1986), A radar technique for high range resolution incoherent scatter autocorrelation function measurements utilizing the full average power of klystron radars, *Radio Sci.*, 21, 1033-1040.
- Sulzer, M. P., (1989), Recent incoherent scatter techniques, *Advances in Space Research*, 9, 153-162.
- Sulzer, M. P., (1993), A new type of alternating code for incoherent scatter measurement, *Radio Sci.*, 28, 995-1001.
- Sulzer, M. P., N. Aponte, and S. A. González (2005), Application of linear regularization methods to Arecibo vector velocities, *Journal of Geophysics Research*, 110, A10305.
- Swartz, W. E., and D. T. Farley (1979), A theory of incoherent scattering of radio waves by a plasma, 5. The use of the Nyquist theorem in general quasi-equilibrium situations, *J. Geophys. Res.*, 84(A5), 1930-1932.
- Taylor, G. N., (1974), Meridional F2-region plasma drifts at Malvern, *J. Atmos. Terr. Phys.*, 36(2), 267-286.
- Thomson, J. J., (1906), *Conduction of Electricity through Gases*. London: Cambridge University Press, 321-326.
- Tsunoda, R. T., et al. (1985), Direct evidence of plasma density structuring in the auroral F-region ionosphere, *Radio Sci.*, 20(4), 762-784.

- Tsunoda, R. T., (1988), High latitude F-region irregularities-A review and synthesis, *Rev. Geophys.*, 26, 719-760.
- van de Kamp, M., P. S. Cannon, and M. Terkildsen (2009), Effect of the ionosphere on defocusing of space-based radars, *Radio Sci.*, 44, RS1003.
- Vasseur, G., (1969), Dynamics of the F region observed with Thomson scatter, 1, Atmospheric circulation and neutral winds, *J. Atmos. Terr. Phys.*, 31, 397-420.
- Verdet, M., (1856), Note sur les propriétés optiques des corps transparents soumis á l'action du magnétisme, *C. R. Acad. Sci.*, 43, 529-532.
- Vickrey, J. F., (1981), Radar Observations of Structured Plasma in the High-Latitude F- Region, SRI Final Report, SRI International, Menlo Park, Calif.
- Vickrey, J. F., C. L. Rino, and T. A. Potemra (1980), Chatanika/Triad observations of unstable ionization enhancements in the auroral F-region, *Geophysics Research Letters*, 7(10), 789-792.
- Wand, R. H., and J. V. Evans (1981), Seasonal and magnetic activity variations of ionospheric electric fields over Millstone Hill, *J. Geophys. Res.* 86(A1), 103-118.
- Wang, W. B., P. Chen, and K. Schlegel (1990), Sources of plasma enhancements in the nighttime auroral F-region results of EISCAT observations, *Ann. Geophys.*, 8, 589-598.
- Watkins, B. J., (1978), A numerical computer investigation of the polar F-region ionosphere, *Planet. Space Sci.*, 26, 559-569.
- Watkins, B. J., K. P. Gudivada and C. T. Fallen (2011), Incoherent-Scatter Radar Observations of Electric-Fields Associated with Substorms, 2011 International Conference on Storms, Substorms and Space Weather (ICSSSW 2011), Hangzhou, China.
- Weber, E. J., et al. (1986), Polar cap F-layer patches: Structure and dynamics, *J. Geophys. Res.*, 91(A11), 12,121-12,129.

- Weber, E. J., and J. Buchau (1981), Polar cap F-layer auroras, *Geophys. Res. Lett.*, 8(1), 125-128.
- Weber, E. J., R. T. Tsunoda, J. Buchau, R. E. Sheehan, D. J. Strickland, W. Whiting, and J. G. Moore (1985), coordinated measurements of auroral zone plasma enhancements, *J. Geophys. Res.*, 90(A7), 6497-6513.
- Weber, E. J., et al. (1984), F-layer ionization patches in the polar cap, *J. Geophys. Res.*, 89, 1683-1694.
- Whittaker, E. T., (1923), On a new method of graduation, *Proceedings of the Edinburgh Mathematical Society*, 41, 62-75.
- Wild, J. P., and J. A. Roberts (1956), The Spectrum of Radio-Star Scintillations and Nature of irregularities in the Ionosphere, *Journal of Atmospheric and Terrestrial Physics*, 8, 55-58.
- Williams, P. J. S., G. O. L. Jones, and A. R. Jain (1984) , Methods of measuring plasma velocity with EISCAT, *Journal of Atmospheric and Terrestrial Physics*, 46, 521-530.
- Woodman, R. F., and T. Hagfors (1969), Methods for the measurement of vertical ionospheric motions near the magnetic equator by incoherent scattering, *J. Geophys. Res.*, 74(5), 1205-1212.
- Yariv, A., and P. Yeh (1984), *Optical Waves in Crystals*, sect. 4.10, Faraday rotation, John-Wiley, New York, 103-104.
- Yeh, K. C., and C. H. Liu (1982), Radio Wave Scintillations in the Ionosphere, *Proc IEEE*, 70, 324-360.
- Yeh, K. C., and G. W. Swenson Jr. (1959), The Scintillation of Radio Signals from Satellites, *J. Geophys. Res.*, 64(12), 2281-2286.
- Yeh, K. C., H. Y. Chao, and K. H. Lin (1999), A study of the generalized Faraday effect in several media, *Radio Sci.*, 34(1), 139-153.

Zamlutti, C. J., (1980), Design of Barker coded multiple pulse experiments, *Journal of Atmospheric and Terrestrial Physics*, 42, 975-982.